

Evaluating Self-Supervised Learning in Medical Imaging: A Benchmark for Robustness, Generalizability, and Multi-Domain Impact

Valay Bundele* Oğuz Ata Çal* Bora Kargi* Karahan Sarıtaş*
 Kıvanç Tezören* Zohreh Ghaderi Hendrik Lensch
 University of Tübingen

*Equal contribution.

Abstract

Self-supervised learning (SSL) has emerged as a promising paradigm in medical imaging, addressing the chronic challenge of limited labeled data in healthcare settings. While SSL has shown impressive results, existing studies in the medical domain are often limited in scope, focusing on specific datasets or modalities, or evaluating only isolated aspects of model performance. This fragmented evaluation approach poses a significant challenge, as models deployed in critical medical settings must not only achieve high accuracy but also demonstrate robust performance and generalizability across diverse datasets and varying conditions. To address this gap, we present a comprehensive evaluation of SSL methods within the medical domain, with a particular focus on robustness and generalizability. Using the MedMNIST dataset collection as a standardized benchmark, we evaluate 8 major SSL methods across 11 different medical datasets. Our study provides an in-depth analysis of model performance in both in-domain scenarios and the detection of out-of-distribution (OOD) samples, while exploring the effect of various initialization strategies, model architectures, and multi-domain pre-training. We further assess the generalizability of SSL methods through cross-dataset evaluations and the in-domain performance with varying label proportions (1%, 10%, and 100%) to simulate real-world scenarios with limited supervision. We hope this comprehensive benchmark helps practitioners and researchers make more informed decisions when applying SSL methods to medical applications.

1. Introduction

Medical image annotation is a resource-intensive task that requires specialized domain knowledge, making it significantly more costly and laborious than annotating natural images [39, 45, 63, 79]. The scarcity of labeled medical data, combined with the complexity of the annotation

process, presents a significant challenge for building effective machine learning models in healthcare. Self-supervised learning has emerged as a powerful solution to these limitations, enabling models to learn rich representations from unlabeled data prior to task-specific fine-tuning with minimal labeled samples [2, 6, 21, 24, 38, 40, 71].

While self-supervised learning (SSL) has proven effective in improving classification performance with limited labels [13–15, 29, 80], there has been limited work in evaluating the *robustness* and *generalizability* of learned models. For safe deployment in healthcare, models must perform reliably across diverse settings and recognize when to withhold predictions on out-of-distribution (OOD) samples. Although SSL methods have been evaluated for OOD detection in natural image contexts [31, 36, 43, 48, 57], their effectiveness in medical imaging remains largely under-researched. Berger et al. [9] explore OOD detection using supervised approaches in a clinical context, but focus solely on chest X-rays, limiting insights across other domains. Bozorgtabar et al. [11] evaluate SSL methods for OOD detection under domain shift but they only investigate two SSL approaches in a single medical domain. Although Cai et al. [12] provide a comprehensive study of SSL for anomaly detection, they focus specifically on anomaly detection SSL methods rather than general-purpose SSL approaches.

Beyond OOD detection, an effective model should generalize across different tasks and modalities—a key requirement in medical imaging where datasets and conditions vary widely. A model that performs well across different datasets or modalities ensures continued diagnostic support even when some imaging modalities are inaccessible, reduces the need for extensive retraining, and ensures robust performance in diverse clinical settings. Azizi et al. [7] propose an SSL-based representation learning method and assess its robustness across various medical imaging tasks and domains. However, they do not compare different SSL methods, leaving a gap in research on the cross-domain generalizability of common SSL approaches.

To address these gaps, our study introduces a compre-

hensive benchmark for evaluating the robustness and generalizability of SSL methods in medical imaging. We assess various SSL methods for OOD detection, comparing the effectiveness of convolutional networks (ResNet-50) with transformer-based architectures (ViT-Small). We further assess the generalizability of learned representations by training linear classifiers on frozen encoders across different datasets, enabling cross-dataset transfer evaluation.

A widely adopted strategy in practice is to initialize model training with weights pre-trained on large-scale natural image datasets, such as IMAGENET1K [20], and subsequently fine-tune the model on a medical dataset [56, 58, 68] — a paradigm known as transfer learning. Supervised IMAGENET1K weights can be used either to initiate subsequent self-supervised training [55, 56], or can be directly used without further training [21]. We adopt the former approach as it better adapts the model to the fine-grained medical domain. Building upon previous research, we investigate how IMAGENET1K initialization affects model generalizability across diverse datasets, while also analyzing its impact on OOD detection performance.

Recent studies also suggest that training across multiple domains can further improve a model’s robustness and generalizability, especially in data-limited, OOD-prone scenarios, such as those often encountered in healthcare [60, 75, 76]. Multi-domain models leverage diverse data sources, allowing them to utilize complementary information across domains and enhance overall performance [16, 70]. However, existing studies do not fully evaluate how common SSL methods perform in the context of multi-domain pre-training. To address this, we conduct experiments to examine influence of multi-domain data on the performance of SSL methods, providing a more comprehensive understanding of their generalizability and robustness.

To summarize, we explore the following key questions:

Q1. How is the in-domain classification performance, generalizability, and robustness to OODs affected by: (1) the choice of SSL method, (2) the initialization strategy, and (3) the model architecture?

Q2. Which SSL method and initialization strategy yield the best performance when labeled data is limited?

Q3. Does multi-domain training improve the robustness and generalizability of SSL encoders, enhancing both in-domain and OOD performance?

By addressing these questions, we provide a deeper understanding of the potential of SSL in medical imaging, offering practical insights for developing more robust and generalizable models in real-world healthcare settings.

2. Related Work

Prior self-supervised benchmarks Several studies have focused on benchmarking self-supervised strategies on nat-

ural image datasets [19, 27, 54]. However, a gap remains in the literature when it comes to benchmarking SSL methods in the medical domain using standardized datasets. Recently, Doerrich et al. [21] proposed a systematic benchmark covering convolutional and transformer-based architectures for both supervised and self-supervised strategies. Nevertheless, their approach relies heavily on IMAGENET1K pre-trained encoders, without incorporating self-supervised pre-training on medical datasets. This may limit model’s ability to capture domain-specific features. Kang et al. [40] demonstrated that self-supervised pre-training outperforms supervised IMAGENET1K baselines for pathology but did not explore other modalities. Huang et al. [38] analyzed SSL and semi-supervised methods with hyperparameter tuning but limited their study to four medical datasets, without assessing robustness or generalizability across diverse tasks. Our work advances SSL benchmarks in the medical domain by evaluating methods across several medical datasets, emphasizing multi-domain performance, encoder robustness, generalizability across different datasets, and adaptability to limited labeled data.

Out-of-Distribution Detection Robust pre-trained encoders can be employed as OOD detectors to prevent dangerous misclassifications in the medical domain. To this end, several studies have investigated the use of visual recognition systems as OOD detectors [9, 26, 48, 59, 81]. Hendrycks et al. [36] show that SSL methods outperform fully supervised ones on natural image datasets for OOD detection. Narayanaswamy et al. [59] address modality shift and novel class detection in the medical domain, but their focus is limited to supervised training of OOD detectors. The SSD framework by Schwag et al. [64] demonstrates that SSL can significantly improve OOD detection, achieving performance comparable to supervised methods. Additionally, both Li et al. [48] and Mohseni et al. [57] introduce self-supervised approaches that improve OOD detection, though their analyses are limited to natural images.

Despite these advancements, there remains a notable gap: no prior work has comprehensively evaluated SSL methods for OOD detection in the medical domain, across diverse architectures and pre-training strategies. Our study aims to fill this gap by providing a benchmark that includes OOD detection experiments tailored to medical imaging.

Generalizability The ability of an encoder to perform effectively on datasets and domains beyond its training distribution is crucial for assessing representation quality. Li et al. [47] enhance generalizability through variational encoding with a linear-dependency regularization, while Yan et al. [73] propose a domain-generalization framework for medical image classification without domain labels in the supervised setting. Although Fedorov et al. [25] investigate the generalization of SSL methods in medical imaging, their analysis is confined to MRI data. Azizi et al. [7] propose an

SSL-based representation learning method, evaluating the robustness of their approach across multiple medical imaging tasks and modalities, yet they do not compare different SSL methods. In contrast, we conduct systematic cross-dataset experiments to evaluate the true generalization capabilities of various SSL approaches.

Transfer Learning In medical domain, network initialization with pre-trained weights from large-scale datasets like IMAGENET1K is a common and effective practice [7, 55, 55, 67, 68]. Tajbakhsh et al. [68] showed that CNNs pre-trained on IMAGENET1K outperform those trained from scratch on medical datasets in a supervised fashion. Matsoukas et al. [55] demonstrated that SSL in the medical domain, initialized with supervised IMAGENET1K weights, is effective for both ViTs and CNNs in medical imaging. To the best of our knowledge, the most comprehensive study on transfer learning in the medical domain is conducted by Taher et al. [67]. Although they emphasize domain-adapted continual pre-training, they implement it exclusively with supervised models, leaving the impact of continual pre-training on SSL largely unexplored. In our work, we investigate continual self-supervised pre-training, as well as the potential of self-supervised IMAGENET1K initialization to yield more generalizable representations, an approach not previously explored in medical context.

3. Methodology

Representation Learning Methods We consider the following eight discriminative SSL methods: SimCLR [14], DINO [13], BYOL [28], ReSSL [80], MoCo v3 [15], NNCLR [23], VICREG [8], and Barlow Twins [77] which are explained briefly in Appendix B. A comprehensive survey by Huang et al. [37] highlights SimCLR, MoCo, and BYOL as the most frequently adopted SSL frameworks in medical imaging research. We include the other methods to make the benchmark more comprehensive.

Tasks and Datasets The datasets utilized in this study are derived from MedMNIST [74], which was introduced to standardize research on medical imaging tasks. To maintain our focus on multiclass medical classification and ordinal regression, we exclude ChestMNIST from our analysis, as it only offers multi-label disease classification. As a result, our experiments span 11 MedMNIST datasets. Additional information about MedMNIST is provided in Appendix A.

Architectures For our study, we use ResNet-50 [33] with approximately 25 million parameters and ViT-Small [22] with approximately 22 million parameters to ensure a fair comparison. We exclude other models like ViT-Tiny and ViT-Base due to their significantly different parameter counts of 5.7 million and 86 million, respectively.

Pre-training We employed the `solo-learn` library [19] with minor modifications for pre-training and linear evaluation. Our implementation details are provided in Appendix C.1, and the code will be released after acceptance. In total, we focus on five different pre-training schemes: supervised training with (1) random initialization and (2) supervised IMAGENET1K initialization; self-supervised pre-training with (3) random initialization, (4) supervised IMAGENET1K initialization, and (5) self-supervised IMAGENET1K initialization.

Linear Evaluation To evaluate the quality of self-supervised pre-trained encoders, we use linear probing, training linear classifiers on frozen features to assess downstream performance [28, 34, 44]. Additionally, to simulate realistic scenarios in the medical domain, we evaluate the low-shot performance by training a multi-class logistic regression on the frozen features with only 1% and 10% labeled data, following the evaluation protocol established by Caron et al. [13]. We report accuracy and Area Under the Curve (AUC) scores. Further details on the linear evaluation setup and evaluation metrics can be found in C.3 and C.4, respectively.

Generalizability To assess generalizability, we conduct cross-dataset experiments using our dataset collection, $\mathcal{D} = \{D_1, \dots, D_{11}\}$. For each SSL method, we pre-train the model on a dataset D_i and evaluate its transferability by training a linear classifier on frozen features on each of the remaining datasets, $\mathcal{D} \setminus D_i$. This process is repeated for each dataset D_i in \mathcal{D} to cover all cross-dataset pairs.

OOD Detection We evaluate various SSL methods for distinguishing between in-distribution and OOD samples, focusing on the impact of backbone architectures, pre-training strategies, and multi-domain learning on OOD detection. We use Mahalanobis Distance [46] to assign pseudo-labels by calculating the distance between input features and the nearest class-conditional Gaussian. Further details on the OOD detection metric and evaluation criteria can be found in Appendix C.5.

Multi-Domain Learning We examine the impact of multi-domain learning by comparing models trained on single-domain MedMNIST datasets with those trained on two dataset combinations. The first combination, named $\text{Organ}\{A,C,S\}$, merges the $\text{Organ}\{A,C,S\}$ MNIST datasets to represent a single-modality scenario. The second combination, referred to as $\text{Organ}\{A,S\}$ PnePath, includes $\text{Organ}\{A,S\}$ MNIST (CT), PathMNIST (Colon Pathology), and PneumoniaMNIST (Chest X-Ray), allowing us to assess the effect of combining different modalities. We then train SSL methods from scratch on these combined datasets to assess how dataset combination affects performance.

4. Experiments & Results

In this section, we analyze the in-domain (ID) performance, robustness to OOD samples, and generalizability of the SSL methods. For clarity in certain figures where direct comparisons between the SSL methods are not essential, we display results for a representative subset of five methods, with complete results available in the Appendix for reference.

4.1. In-Domain Performance

We evaluate each SSL method’s in-distribution (ID) performance by pre-training a randomly initialized ResNet-50 on each dataset’s training split, then performing linear evaluation on the test split using the frozen backbone. As shown in Table 2, MoCo v3 exhibits strong performance, achieving the highest accuracy across 5 of the 11 datasets. BYOL and SimCLR also demonstrate competitive results, trailing closely behind MoCo v3. Notably, self-supervised learning outperforms supervised learning in 7 out of 11 datasets when both approaches start from random initialization.

Next, we analyze the effect of supervised IMAGENET1K initialization on self-supervised training performance for in-domain tasks. As shown in Figure 1, IMAGENET1K initialization consistently improves performance on in-domain classification tasks, a trend also observed across other methods in Appendix D.1. Interestingly, DINO and BYOL show the most significant accuracy gains when transitioning from random to IMAGENET1K initialization.

Figure 2 further emphasizes the effect of IMAGENET1K initialization by showing the accuracy differential between ResNet-50 and ViT ($ACC_{RN50} - ACC_{ViT}$) across various methods and datasets, presented for both random and IMAGENET1K-initialized cases. In both scenarios, ResNet-50 generally outperforms ViT. However, the accuracy gap between these architectures generally narrows when transitioning from random initialization to IMAGENET1K-supervised weights. This reduction can be attributed to two factors: firstly, as overall accuracy improves, incremental gains in performance diminish, naturally reducing the architecture gap. Secondly, as prior research suggests [3, 5, 22], the data-intensive nature of transformer-based architectures can be harnessed effectively through large-scale pre-training, such as with IMAGENET1K initialization. Complete numerical results for all methods are provided in Appendix D.1.

Expanding on our in-domain performance evaluation, we also examine how the architectures perform under different levels of label availability. Table 1 presents accuracy drops for various SSL methods when reducing label availability from 100% to 1% in random initialization setting. ResNet-50 not only outperforms other methods in the fully labeled (100%) scenario, as shown in Figure 2, but also exhibits consistently lower average performance drops across nearly all methods. This indicates that ResNet-50 main-

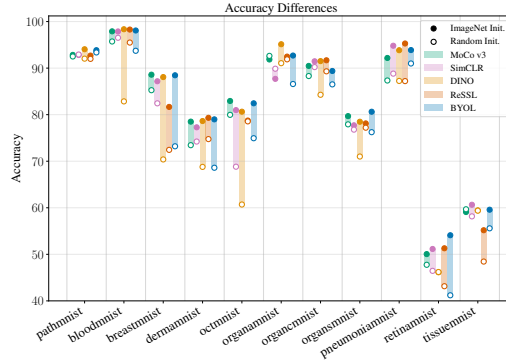


Figure 1. Accuracy differences between self-supervised pre-training with random (unfilled markers) vs. IMAGENET1K (filled markers) initialization using ResNet-50 backbone.

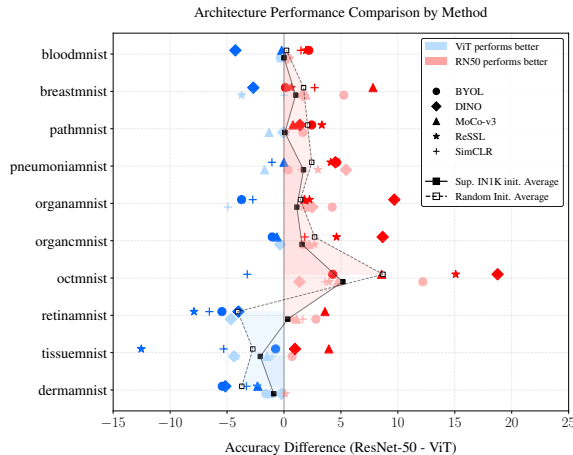


Figure 2. Performance differential between ResNet-50 and ViT across SSL methods, comparing initialization strategies. Dark colors stand for random initialization, whereas light colors stand for IMAGENET1K initialization. For each dataset, geometric markers show individual method performance differentials. The connecting lines represent the mean performance differential across all methods for different initialization strategies.

tains more robust performance compared to ViT-Small even under severe label scarcity. A similar pattern can also be observed across other methods and in IMAGENET1K initialization setting in Appendix D.1, highlighting that transformers generally require more labeled data to reach optimal performance [71, 82].

Moreover, Figure 3 presents a bar chart comparing the mean test accuracies of ResNet-50 across different label availability settings (1%, 10%, and 100%), highlighting the effects of IMAGENET1K versus random initialization. The results show that models initialized with IMAGENET1K weights consistently outperform their randomly initialized counterparts, especially under label-scarce conditions. This finding underscores the value of pre-trained weights in

boosting model performance when labeled data is limited. Notably, with IMAGENET1K initialization, DINO excels in label-scarce scenarios, though it is slightly outperformed by BYOL at the 100% label level. On the other hand, MoCo v3 shows promising results across most of the label percentages in the random initialization setting, slightly losing only to NNCLR at the 1% label level. A similar trend captured in ViT models is shown in Appendix D.1.

Table 1. Accuracy drops from 100% to 1% label availability across datasets for each method and architecture with random initialization. Larger drops are highlighted in red, emphasizing higher sensitivity to limited labeled data.

	SimCLR		DINO		BYOL		ReSSL		MoCo v3	
	RN50	ViT	RN50	ViT	RN50	ViT	RN50	ViT	RN50	ViT
Path	2.91	0.10	0.24	1.22	1.10	1.60	2.38	0.22	-0.12	1.50
Derma	4.54	7.93	1.90	6.56	1.68	4.51	5.54	8.41	3.00	5.47
OCT	9.24	5.62	0.56	6.08	-2.24	7.52	-2.16	10.76	4.20	8.18
Pneumonia	-0.13	9.84	-2.85	0.22	0.06	-2.21	-3.07	3.72	0.45	-0.67
Retina	4.50	9.65	3.30	5.85	-0.85	1.90	0.40	7.00	4.70	0.60
Breast	7.82	3.72	0.51	0.00	0.13	0.00	0.77	1.15	6.54	0.90
Blood	3.34	13.11	12.34	14.57	8.45	17.43	9.92	13.91	6.28	12.04
Tissue	6.66	6.37	7.45	5.04	7.10	8.69	5.76	6.58	7.18	10.20
OrganA	9.40	9.10	8.72	11.73	9.42	6.99	7.36	8.00	6.17	4.63
OrganC	11.45	16.95	23.87	16.93	18.81	15.09	20.32	16.23	14.36	11.20
OrganS	13.83	15.71	21.52	20.16	16.77	15.38	20.13	22.46	21.66	18.33
Average	6.69	8.92	7.05	8.03	5.49	6.99	6.12	8.95	6.76	6.58
Counts	5	6	4	7	5	6	2	10	6	5

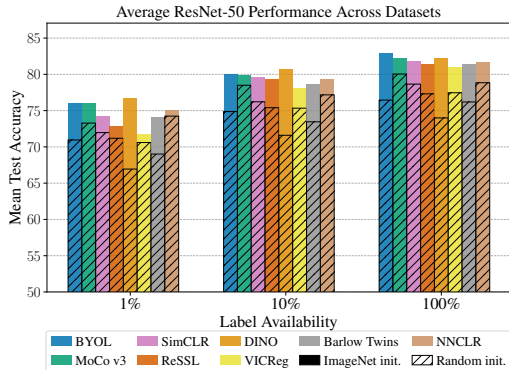


Figure 3. Mean test accuracy across various datasets with 1%, 10%, and 100% label availability, comparing IMAGENET1K against random initialization (hatched) using ResNet-50.

Next, we examine the impact of using self-supervised IMAGENET1K initialization, as opposed to random or supervised IMAGENET1K initialization, on in-domain performance using MoCo v3, SimCLR, BYOL, and DINO. Table 3 presents a comparative analysis of these initialization strategies for self-supervised pre-training using ResNet-50. Although there does not appear to be a clear winner between them, self-supervised IMAGENET1K initialization exhibits competitive performance relative to supervised IMAGENET1K initialization, achieving the best accuracies in 5 of the 11 datasets examined. Currently, deep learning frameworks lack a standardized approach for initialization using self-supervised weights. These results can motivate

developers to also include self-supervised IMAGENET1K weights in deep learning libraries.

Finally, we examine the impact of multi-domain training on in-domain performance. As shown in Figure 4, pre-training on a multi-domain dataset consisting of similar domains (OrganA, OrganC, and OrganS) with random initialization outperforms training on individual single-domain datasets with random initialization. Furthermore, it achieves performance comparable to single-domain training with IMAGENET1K-initialization. In contrast, combining datasets from diverse domains (OrganA, OrganS, Pneumonia, and Path) does not significantly improve accuracy, and may even result in poorer performance. These findings suggest that multi-domain pretraining is beneficial when the domains of combined datasets are similar, whereas combining diverse domains may not provide performance benefits.

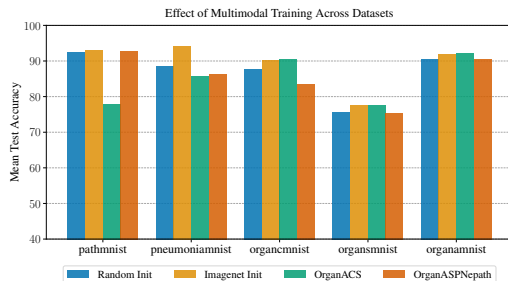


Figure 4. Mean ID performance of SSL methods (ResNet-50), trained on single-domain datasets with different initialization strategies and multi-domain datasets with random initialization.

4.2. Out-of-Distribution Detection

We perform several experiments to assess OOD detection performance of each SSL method. In each experiment, one dataset serves as the ID dataset, while others are treated as OOD for evaluation; resulting in 110 OOD tests (11×10) per method. The pre-trained encoder, trained on the ID dataset, is evaluated for its ability to detect OOD samples.

Figure 5 illustrates the distribution of AUROC scores for OOD detection across various SSL methods using randomly initialized ResNet-50 backbones. Among these, NNCLR and MoCo v3 achieve the highest AUROC scores, suggesting that these methods are particularly effective in learning representations that differentiate ID from OOD samples. When evaluated with a ViT-Small backbone, MoCo v3 demonstrate strong OOD detection performance, which aligns with expectations, as this method were originally developed for the ViT architecture. Detailed analysis of the effect of backbone choice on each method and in-distribution, out-of-distribution pairs ($\mathcal{P}_{ID}, \mathcal{P}_{OOD}$) can be found in Appendix D.2.2.

In our experimental setup, the choice of backbone architecture played a crucial role in OOD detection perfor-

Table 2. In-domain performance of SSL methods on a randomly initialized ResNet-50 backbone, reported as Area Under the Curve (AUC) and Accuracy (ACC). Supervised learning results with random and IMAGENET1K initialization are included for comparison. The highest accuracy scores achieved using SSL methods are highlighted in green while the lowest ones are highlighted in red.

Method	PathMNIST		DermaMNIST		OCTMNIST		PneumoniaMNIST		RetinaMNIST	
	AUC ↑	ACC ↑	AUC ↑	ACC ↑	AUC ↑	ACC ↑	AUC ↑	ACC ↑	AUC ↑	ACC ↑
Supervised (random init.)	98.38±0.53	91.52±1.03	90.79±0.45	74.68±0.89	95.78±0.84	83.14±1.34	93.48±3.32	84.26±2.54	71.78±2.64	52.10±3.03
Supervised (IMAGENET1K init.)	99.46±0.25	94.13±0.43	94.41±1.43	82.79±0.81	96.93±0.57	83.24±1.59	94.84±2.73	89.39±0.88	73.86±1.34	51.55±4.68
SimCLR	99.45±0.01	92.91±0.08	89.20±0.32	74.22±0.18	92.17±0.27	68.82±0.24	94.36±2.54	88.81±4.79	63.38±6.30	46.45±2.20
DINO	99.28±0.01	92.03±0.13	80.67±0.49	68.77±0.22	90.01±0.05	60.70±0.29	90.29±3.01	87.24±3.76	58.72±1.87	46.20±3.55
BYOL	99.44±0.01	93.36±0.13	76.65±0.49	68.59±0.39	95.67±0.29	74.94±0.84	97.45±0.21	90.99±1.07	51.64±0.85	41.20±2.29
ReSSL	99.23±0.02	91.98±0.19	89.87±0.05	74.75±0.27	96.07±0.11	78.56±0.24	94.23±1.18	87.21±2.25	60.35±2.21	43.15±1.53
MoCo v3	99.27±0.02	92.50±0.25	87.60±0.35	73.44±0.16	96.81±0.08	79.96±0.32	98.39±0.19	87.34±3.46	65.37±3.08	47.75±1.86
VICReg	99.25±0.02	92.31±0.17	86.64±0.28	73.05±0.33	96.60±0.05	75.20±0.95	96.50±0.23	91.02±0.66	63.49±5.43	49.15±1.51
Barlow Twins	99.38±0.01	92.43±0.07	86.28±0.07	72.82±0.07	97.05±0.04	77.28±0.58	92.38±1.14	88.07±1.53	67.19±3.35	52.50±1.05
NNCLR	99.26±0.02	92.71±0.17	85.44±0.13	72.67±0.26	97.11±0.08	79.16±0.36	94.27±0.68	88.23±1.38	62.72±0.57	47.40±2.23

Method	BreastMNIST		BloodMNIST		TissueMNIST		OrganAMNIST		OrganCMNIST		OrganSMNIST	
	AUC ↑	ACC ↑	AUC ↑	ACC ↑	AUC ↑	ACC ↑	AUC ↑	ACC ↑	AUC ↑	ACC ↑	AUC ↑	ACC ↑
Supervised (random init.)	88.99±2.46	83.71±2.73	99.88±0.02	97.83±0.21	92.37±0.05	69.95±0.19	99.49±0.11	92.32±0.38	99.14±0.09	90.11±0.66	96.48±0.30	78.14±0.51
Supervised (IMAGENET1K init.)	88.20±4.92	85.64±2.96	99.88±0.04	98.34±0.17	93.35±0.12	71.72±0.16	99.70±0.09	95.19±0.74	99.61±0.07	94.22±0.23	97.12±0.32	82.52±0.85
SimCLR	85.56±1.75	82.43±2.36	99.80±0.00	96.51±0.12	87.38±0.00	58.15±0.07	97.92±0.82	89.87±2.27	99.29±0.03	90.22±0.24	97.35±0.37	76.78±0.24
DINO	62.23±1.55	70.38±1.98	97.53±0.04	82.85±0.36	88.55±0.01	59.38±0.04	99.49±0.02	91.05±0.49	98.35±0.04	84.27±0.28	95.55±0.05	71.00±0.30
BYOL	53.18±8.85	73.20±0.36	99.47±0.03	93.72±0.34	86.11±0.01	55.58±0.08	98.96±0.03	86.58±0.62	98.71±0.07	86.50±0.12	97.41±0.05	76.23±0.69
ReSSL	51.65±6.57	72.43±1.78	99.69±0.01	95.48±0.14	78.65±0.03	48.44±0.11	99.60±0.05	91.88±0.45	99.30±0.02	89.31±0.18	97.57±0.04	77.20±0.48
MoCo v3	80.93±1.57	85.25±0.56	99.71±0.02	95.72±0.37	88.66±0.02	59.67±0.11	99.57±0.16	92.62±1.30	98.51±0.37	88.29±0.83	97.87±0.01	77.92±0.22
VICReg	58.48±11.73	73.46±0.44	99.47±0.01	93.24±0.23	86.34±0.01	56.20±0.14	99.21±0.06	89.66±0.66	98.67±0.16	84.87±1.44	96.47±0.09	73.86±0.42
Barlow Twins	67.44±4.58	79.61±0.87	90.40±0.32	64.43±0.45	84.16±0.05	53.89±0.15	99.47±0.04	91.20±0.40	98.90±0.09	89.28±0.21	97.57±0.02	76.54±0.20
NNCLR	63.59±0.89	73.07±0.80	99.74±0.01	95.94±0.09	88.41±0.02	59.39±0.03	99.67±0.04	92.56±0.53	99.31±0.16	89.45±1.65	97.40±0.14	76.64±1.38

Table 3. Comparison between supervised and self-supervised IMAGENET1K initialization across different methods and datasets. Best accuracies for each method are underlined.

Dataset	MoCo v3		SimCLR		DINO		BYOL	
	Sup.	SSL	Sup.	SSL	Sup.	SSL	Sup.	SSL
Path	92.84	93.52	92.81	92.52	94.05	93.85	93.85	93.43
Derma	78.50	77.29	77.29	76.66	78.63	80.21	78.99	77.12
OCT	82.94	81.48	80.98	75.46	80.64	80.10	82.44	80.56
Pneumonia	92.18	94.36	94.81	93.78	93.85	92.12	93.88	91.47
Retina	50.05	51.40	51.15	52.35	46.15	55.40	54.10	41.75
Breast	88.59	84.62	87.18	90.00	88.08	89.49	88.46	85.77
Blood	97.90	98.12	97.88	97.99	98.35	98.22	98.08	98.29
Tissue	59.09	63.27	60.65	62.90	59.43	47.21	59.58	61.23
OrganA	91.85	91.70	87.69	91.02	95.13	93.43	92.70	91.58
OrganC	90.47	91.26	91.47	89.58	91.51	91.81	89.38	91.01
OrganS	79.69	77.39	77.72	78.91	78.48	79.75	80.63	76.18

mance. Specifically, models using ViT-Small consistently outperformed those using ResNet-50, as shown in Figure 6. This observation aligns with prior research, such as [26, 78], which demonstrated that Transformer-based architectures like ViT generally excel in OOD detection tasks. Furthermore, this trend held across all evaluated SSL methods, suggesting that the improved AUROC scores result from the ViT backbone itself rather than any specific SSL method.

We observe that the impact of initialization on OOD detection varies depending on the choice of backbone, SSL method, and in-domain dataset distribution \mathcal{P}_{ID} . Generally, for smaller datasets such as BreastMNIST, RetinaMNIST, and DermaMNIST, models initialized with IMAGENET1K weights demonstrate improved performance. For the ResNet-50 backbone, SSL methods such as Sim-

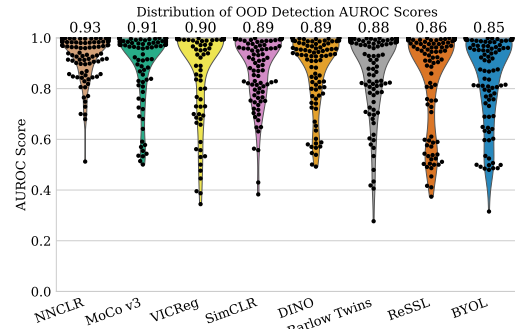


Figure 5. AUROC score distributions for SSL methods with randomly initialized ResNet-50 backbones in OOD detection. Models are ordered by mean AUROC scores (shown above), calculated by averaging over all $(\mathcal{P}_{ID}, \mathcal{P}_{OOD})$ combinations. Black dots indicate individual AUROC scores for each $(\mathcal{P}_{ID}, \mathcal{P}_{OOD})$ dataset pair.

CLR, ReSSL, MoCo v3, and VICReg showed improved performance in OOD detection with random initialization. In the case of ViT-Small backbone models, although differences in OOD detection scores were less pronounced, there was still a noticeable tendency for models to favor random initialization, with VICReg showing the strongest preference for random initialization among them. Detailed information about initialization preferences for each SSL method and backbone can be found in Appendix D.2.3.

Lastly, we compare OOD detection performance between models trained on multi-domain datasets (Organ{A,C,S} and Organ{A,S}PnePath) versus their con-

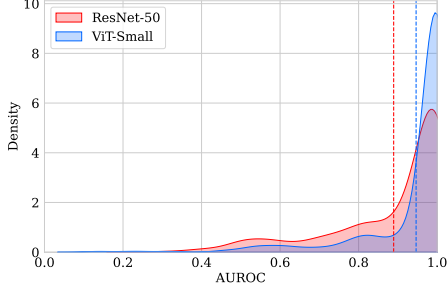


Figure 6. Density distributions of AUROC scores for OOD detection, calculated across all SSL models, comparing ResNet-50 and ViT-Small with random initializations. The dashed line indicates the mean AUROC score, averaged over all $(\mathcal{P}_{ID}, \mathcal{P}_{OOD})$ pairs.

stituent single-domain datasets. Figure 7 shows the mean AUROC differences across SSL methods. Our results show that for all SSL methods, $\text{Organ}\{A,S\}\text{PnePath}$ consistently improves AUROC scores across most ID-OOD pairs, with the exception of a single pair. In contrast, $\text{Organ}\{A,C,S\}$ generally decreases OOD detection performance across most ID-OOD pairs, particularly for models trained with MoCo v3, SimCLR, and ReSSL. These findings demonstrate that a multi-domain dataset with greater domain diversity ($\text{Organ}\{A,S\}\text{PnePath}$) provides a more substantial OOD detection performance boost compared to a more homogeneous multi-domain dataset ($\text{Organ}\{A,C,S\}$).

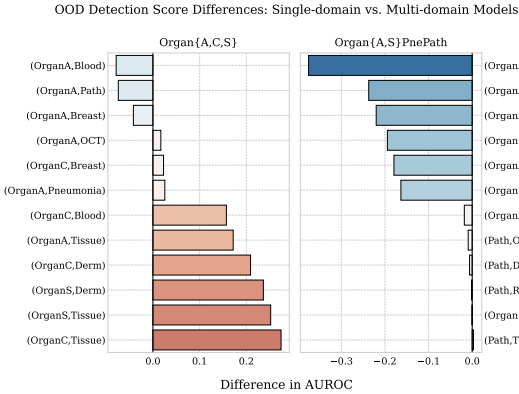


Figure 7. Mean average differences in OOD AUROC scores between models trained on single-domain and multi-domain datasets. The y-axis lists $(\mathcal{P}_{ID}, \mathcal{P}_{OOD})$ pairs where \mathcal{P}_{ID} represents the in-domain dataset used to calculate Gaussian class centers, and \mathcal{P}_{OOD} represents the OOD dataset. For clarity, only the top 6 pairs with the highest AUROC score differences and the bottom 6 pairs with the lowest differences are shown.

4.3. Generalizability

In this section, we evaluate transferability of representations learned from SSL methods by performing cross-dataset evaluations. Specifically, we first pre-train the encoder on

one of the datasets and then train a linear classifier on each of the remaining datasets individually, using a frozen encoder. We evaluate the generalizability of learned representations by calculating the drop in accuracy relative to the in-domain performance as, $\Delta\text{ACC} = \frac{\text{ACC}_{ID} - \text{ACC}_{\text{transfer}}}{\text{ACC}_{ID}} \times 100$, where ACC_{ID} represents the accuracy when training and testing are performed on the same dataset (in-domain), and $\text{ACC}_{\text{transfer}}$ denotes the accuracy when the model is pre-trained on a different dataset. For each source dataset, we calculate the average accuracy drop ($\bar{\Delta\text{ACC}}$) across all target datasets, providing insights into how well a method trained on one dataset performs when transferred to others and which datasets yield the most transferable knowledge.

Table 4 shows that SimCLR and MoCo v3 excel in generalization, with both achieving the lowest accuracy drops in 4 datasets. Notably, models pre-trained on PathMNIST or $\text{Organ}\{C,S\}\text{MNIST}$ show the lowest accuracy drops, suggesting these datasets offer the most transferable representations.

Table 4. **Average Accuracy Drops in Transfer Performance:** The accuracy drop percentages, relative to the mean in-domain performance using ResNet-50 with random initialization are averaged over all possible target datasets. The lowest accuracy drops are highlighted in green, indicating better generalizability. Due to space constraints, only five of the eight evaluated methods are displayed. However, the shown results correspond to the best-performing method out of the full set of eight candidates.

Source	Average Accuracy Drop $\bar{\Delta\text{ACC}}$ (percentage)				
	SimCLR	MoCo v3	Barlow Twins	NNCLR	ReSSL
Path	6.44±5.78	6.38±5.99	3.32±5.82	6.80±6.41	10.10±7.54
Derma	11.16±7.00	16.06±8.55	13.32±8.77	19.81±10.60	14.08±10.36
OCT	14.18±5.06	8.62±4.87	8.05±4.52	11.40±5.68	12.87±6.67
Pneumonia	11.46±7.84	9.77±8.73	17.52±9.23	10.40±7.40	14.96±8.29
Retina	13.73±8.22	13.96±8.25	31.55±14.10	27.84±13.86	16.14±9.26
Breast	12.60±7.84	23.16±11.43	18.46±10.14	39.06±17.18	43.00±18.46
Blood	11.55±9.47	9.37±8.53	33.78±16.95	11.14±7.59	12.04±8.49
Tissue	9.09±5.21	7.70±7.43	8.86±8.36	9.09±7.66	12.57±7.26
OrganA	10.14±8.08	6.24±7.50	7.17±6.53	5.62±8.09	7.97±7.56
OrganC	6.12±5.92	5.54±7.73	7.15±6.25	6.22±6.22	6.81±7.00
OrganS	5.68±7.00	6.60±6.37	7.01±6.38	6.02±6.12	8.73±6.26

We further examine the impact of supervised IMAGENET1K initialization on model generalizability. Figure 8 illustrates the transfer performance difference for models pre-trained on DermaMNIST with random versus IMAGENET1K initialization. In general, the results favor IMAGENET1K initialization across the majority of evaluation scenarios. This trend holds across other datasets and self-supervised methods as well. To evaluate the overall impact of IMAGENET1K initialization compared to random initialization, we conducted paired t -tests for each test dataset across all cross-dataset training combinations including the in-domain setting where test and train splits come from the same dataset. The results demonstrate statistically significant improvements ($p < 0.05$) across all datasets, with PneumoniaMNIST showing the most modest relative gain

($1.88 \pm 3.28\%$) and OCTMNIST exhibiting the largest improvement ($13.22 \pm 25.59\%$). Detailed quantitative results are provided in Appendix D.3. While previous studies have raised concerns about the efficacy of transfer learning from natural to medical images due to significant distributional differences [61], our findings show that continual pre-training [32, 67] improves both in-domain performance and generalization across diverse medical datasets.

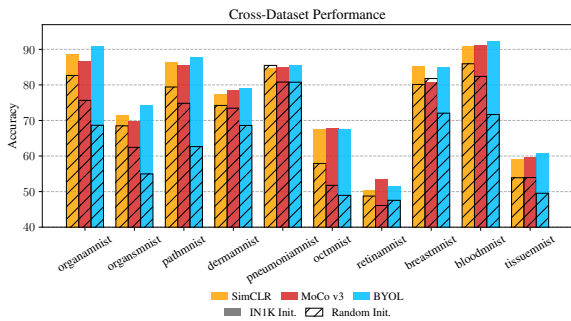


Figure 8. Comparison of transfer performance for SSL methods pre-trained on DermaMNIST with IMAGENET1K and random initializations (hatched). Only SimCLR, MoCo v3, and BYOL are chosen for better visualization.

While ResNet-50 achieved higher in-domain performance than ViT-Small in most datasets (8/11 when trained from scratch and 9/11 when starting from IMAGENET1K weights), ViT-Small demonstrated superior cross-dataset generalization. Specifically, when averaged across different methods, ViT-Small’s performance consistently exceeded that of ResNet-50 by a significant margin in all datasets when trained from scratch. In the pretrained scenario, it outperformed ResNet-50 in 9 out of 11 datasets, with only marginal differences in the remaining two, as shown in Figure 9.

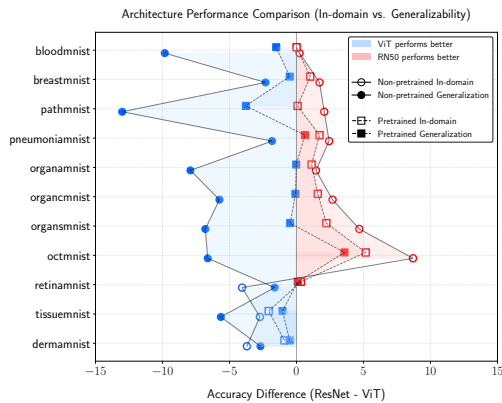


Figure 9. Performance differential between ResNet-50 and ViT (averaged over methods) for both in-domain and cross-dataset evaluations using two different initialization strategies.

Finally, we evaluate the generalizability of representations learned through multi-domain training. Figure 10 compares the cross-dataset performance of models trained on multi-domain datasets with models trained on their individual constituents. Training with similar domain datasets ($\text{Organ}\{A,C,S\}$) enhances cross-dataset transfer performance, suggesting that multi-domain training within a single modality may act as a regularizer. However, this benefit does not hold for mixed-modality combinations ($\text{Organ}\{A,S\}\text{PnePath}$), showing that multi-domain training benefits are modality-dependent (also see Appendix D.3).

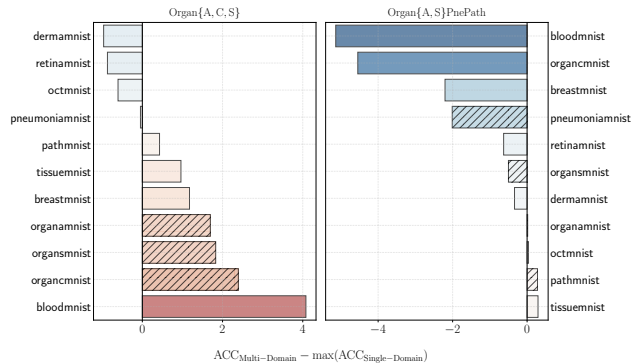


Figure 10. Comparison of performance differences between multi-domain and single-domain models. The bars show the average accuracy difference over five methods between the multi-domain model and the best-performing single-domain model accuracy for that dataset, with in-domain tasks highlighted using dashed lines.

5. Discussion & Conclusion

We have conducted a comprehensive evaluation of popular SSL methods in medical imaging, addressing a crucial gap in understanding how these methods perform across diverse medical tasks. Based on our results and analysis, we offer the following recommendations for practitioners:

Which self-supervised method to choose? MoCo v3 demonstrates remarkable versatility in medical imaging tasks when trained from scratch, achieving superior performance in 5/11 datasets for in-domain tasks and maintaining minimal accuracy drops in 4/11 datasets for cross-domain generalization. It also shows competitive performance in OOD detection tasks. However, the effectiveness of certain SSL methods is significantly influenced by initialization strategy. Notably, DINO and BYOL transform from being among the lowest performers to achieving competitive in-domain results when initialized with IMAGENET1K weights, with DINO particularly excelling with ViT.

Should we start self-supervised pre-training with supervised IMAGENET1K weights? Despite concerns that supervised pre-training might yield less general representations due to label dependency [49, 62], IMAGENET1K ini-

tialization enhances both in-domain and cross-dataset performance. However, this advantage does not consistently extend to OOD detection, as IMAGENET1K initialization degrades performance for certain backbone and model combinations. Overall, supervised and self-supervised IMAGENET1K initialization offer comparable performance, with no clear advantage for either.

Which model architecture is better? Choosing between these architectures involves key trade-offs: While ResNet-50 excels in in-domain classification, ViT-Small demonstrates superior performance in OOD detection and better generalization across datasets, achieving higher mean accuracies in all cross-dataset evaluations. Though these representations are more generalizable, ViT shows greater sensitivity to label scarcity, with performance dropping more steeply when training data is limited. Consistent with Matsoukas et al. [55], IMAGENET1K initialization reduces performance gap, though the trade-offs remain.

Is multi-domain SSL effective? Dataset composition plays a crucial role in model performance. Models trained on heterogeneous datasets ($\text{Organ}\{A,S\}$ PnePath) demonstrated superior OOD detection performance, achieving consistently higher AUROC scores compared to models trained on homogeneous ($\text{Organ}\{A,C,S\}$) or single-domain datasets. In contrast, $\text{Organ}\{A,C,S\}$ often reduces OOD detection performance, underscoring the limitations of less diverse datasets. While $\text{Organ}\{A,C,S\}$ yields better in-domain accuracy and more generalizable representations compared to individual Organ datasets, this pattern does not hold for the more diverse $\text{Organ}\{A,S\}$ PnePath.

6. Acknowledgements

B.K. gratefully acknowledges partial support from the Konrad Zuse School of Excellence in Learning and Intelligent Systems (ELIZA) Master’s Scholarships.

References

[1] Andrea Acevedo, Anna Merino, Santiago Alf3rez, 3ngel Molina, Laura Bold3, and Jos3 Rodellar. A dataset of microscopic peripheral blood cell images for development of automatic recognition systems. *Data in Brief*, 30:105474, 2020. 14

[2] Muhammad Muneeb Afzal, Muhammad Osama Khan, and Yi Fang. A comprehensive benchmark of supervised and self-supervised pre-training on multi-view chest x-ray classification. In *Medical Imaging with Deep Learning*, 2024. 1

[3] Hassan Akbari, Liangzhe Yuan, Rui Qian, Wei-Hong Chuang, Shih-Fu Chang, Yin Cui, and Boqing Gong. Vatt: Transformers for multimodal self-supervised learning from raw video, audio and text, 2021. 4

[4] Walid Al-Dhabyani, Mohammed Gomaa, Hussien Khaled,

and Aly Fahmy. Dataset of breast ultrasound images. *Data in Brief*, 28:104863, 2020. 14

[5] Anurag Arnab, Mostafa Dehghani, Georg Heigold, Chen Sun, Mario Lu3i3, and Cordelia Schmid. Vivit: A video vision transformer, 2021. 4

[6] Shekoofeh Azizi, Basil Mustafa, Fiona Ryan, Zachary Beaver, Jan Freyberg, Jonathan Deaton, Aaron Loh, Alan Karthikesalingam, Simon Kornblith, Ting Chen, Vivek Natarajan, and Mohammad Norouzi. Big self-supervised models advance medical image classification, 2021. 1

[7] Shekoofeh Azizi, Laura Culp, Jan Freyberg, Basil Mustafa, Sebastien Baur, Simon Kornblith, Ting Chen, Patricia MacWilliams, S. Sara Mahdavi, Ellery Wulczyn, Boris Babenko, Megan Wilson, Aaron Loh, Po-Hsuan Cameron Chen, Yuan Liu, Pinal Bavishi, Scott Mayer McKinney, Jim Winkens, Abhijit Guha Roy, Zach Beaver, Fiona Ryan, Justin Krogue, Mozziyar Etemadi, Umesh Telang, Yun Liu, Lily Peng, Greg S. Corrado, Dale R. Webster, David Fleet, Geoffrey Hinton, Neil Houlsby, Alan Karthikesalingam, Mohammad Norouzi, and Vivek Natarajan. Robust and efficient medical imaging with self-supervision, 2022. 1, 2, 3

[8] Adrien Bardes, Jean Ponce, and Yann LeCun. Vi-creg: Variance-invariance-covariance regularization for self-supervised learning, 2022. 3, 15

[9] Christoph Berger, Magdalini Paschali, Ben Glocker, and Konstantinos Kamnitsas. Confidence-based out-of-distribution detection: A comparative study and analysis, 2021. 1, 2

[10] Patrick Bilic, Patrick Christ, Hongwei Bran Li, Eugene Vorontsov, Avi Ben-Cohen, Georgios Kaissis, Adi Szeskin, Colin Jacobs, Gabriel Efrain Humpire Mamani, Gabriel Chartrand, et al. The liver tumor segmentation benchmark (lits). *Medical Image Analysis*, 84:102680, 2023. 14

[11] Behzad Bozorgtabar, Guillaume Vray, Dwarikanath Mahapatra, and Jean-Philippe Thiran. Sood: Self-supervised out-of-distribution detection under domain shift for multi-class colorectal cancer tissue types. In *2021 IEEE/CVF International Conference on Computer Vision Workshops (ICCVW)*, pages 3317–3326, 2021. 1

[12] Yu Cai, Weiwen Zhang, Hao Chen, and Kwang-Ting Cheng. Medianomaly: A comparative study of anomaly detection in medical images, 2024. 1

[13] Mathilde Caron, Hugo Touvron, Ishan Misra, Herv3 J3gou, Julien Mairal, Piotr Bojanowski, and Armand Joulin. Emerging properties in self-supervised vision transformers, 2021. 1, 3, 14, 24

[14] Ting Chen, Simon Kornblith, Mohammad Norouzi, and Geoffrey Hinton. A simple framework for contrastive learning of visual representations, 2020. 3, 14

[15] Xinlei Chen, Saining Xie, and Kaiming He. An empirical study of training self-supervised vision transformers, 2021. 1, 3, 14

[16] Yunfeng Chen, Yalan Lin, Xiaodie Xu, Jinzhen Ding, Chuzhao Li, Yiming Zeng, Weifang Xie, and Jianlong Huang. Multi-domain medical image translation generation for lung image classification based on generative adversarial networks. *Computer Methods and Programs in Biomedicine*, 229:107200, 2023. 2

- [17] Noel Codella, Veronica Rotemberg, Philipp Tschandl, M. Emre Celebi, Stephen Dusza, David Gutman, Brian Helba, Aadi Kaloo, Konstantinos Liopyris, Michael Marchetti, et al. Skin lesion analysis toward melanoma detection 2018: A challenge hosted by the international skin imaging collaboration (isic). In *2019 IEEE 16th International Symposium on Biomedical Imaging (ISBI 2019)*, pages 168–172. IEEE, 2019. 14
- [18] MMSelfSup Contributors. MMSelfSup: Openmmlab self-supervised learning toolbox and benchmark. <https://github.com/open-mmlab/mmselfsup>, 2021. 15
- [19] Victor G. Turrissi da Costa, Enrico Fini, Moin Nabi, Nicu Sebe, and Elisa Ricci. Solo-learn: A library of self-supervised methods for visual representation learning, 2022. 2, 3
- [20] Jia Deng, Wei Dong, Richard Socher, Li-Jia Li, Kai Li, and Li Fei-Fei. Imagenet: A large-scale hierarchical image database. In *2009 IEEE Conference on Computer Vision and Pattern Recognition*, pages 248–255, 2009. 2
- [21] Sebastian Doerrich, Francesco Di Salvo, Julius Brockmann, and Christian Ledig. Rethinking model prototyping through the medmnist+ dataset collection, 2024. 1, 2, 13
- [22] Alexey Dosovitskiy, Lucas Beyer, Alexander Kolesnikov, Dirk Weissenborn, Xiaohua Zhai, Thomas Unterthiner, Mostafa Dehghani, Matthias Minderer, Georg Heigold, Sylvain Gelly, Jakob Uszkoreit, and Neil Houlsby. An image is worth 16x16 words: Transformers for image recognition at scale, 2021. 3, 4
- [23] Debidatta Dwibedi, Yusuf Aytar, Jonathan Tompson, Pierre Sermanet, and Andrew Zisserman. With a little help from my friends: Nearest-neighbor contrastive learning of visual representations, 2021. 3, 15
- [24] Linus Ericsson, Henry Gouk, Chen Change Loy, and Timothy M. Hospedales. Self-supervised representation learning: Introduction, advances, and challenges. *IEEE Signal Processing Magazine*, 39(3):42–62, 2022. 1
- [25] Alex Fedorov, Eloy Geenjaar, Lei Wu, Thomas P. DeRamus, Vince D. Calhoun, and Sergey M. Plis. Tasting the cake: evaluating self-supervised generalization on out-of-distribution multimodal mri data, 2022. 2
- [26] Ido Galil, Mohammed Dabbah, and Ran El-Yaniv. A framework for benchmarking class-out-of-distribution detection and its application to imagenet, 2023. 2, 6, 17
- [27] Priya Goyal, Dhruv Mahajan, Abhinav Gupta, and Ishan Misra. Scaling and benchmarking self-supervised visual representation learning, 2019. 2
- [28] Jean-Bastien Grill, Florian Strub, Florent Altché, Corentin Tallec, Pierre H. Richemond, Elena Buchatskaya, Carl Doversch, Bernardo Avila Pires, Zhaohan Daniel Guo, Mohammad Gheshlaghi Azar, Bilal Piot, Koray Kavukcuoglu, Rémi Munos, and Michal Valko. Bootstrap your own latent: A new approach to self-supervised learning, 2020. 3
- [29] Jean-Bastien Grill, Florian Strub, Florent Altché, Corentin Tallec, Pierre H. Richemond, Elena Buchatskaya, Carl Doversch, Bernardo Avila Pires, Zhaohan Daniel Guo, Mohammad Gheshlaghi Azar, Bilal Piot, Koray Kavukcuoglu, Rémi Munos, and Michal Valko. Bootstrap your own latent: A new approach to self-supervised learning, 2020. 1, 14
- [30] Jie Gui, Tuo Chen, Jing Zhang, Qiong Cao, Zhenan Sun, Hao Luo, and Dacheng Tao. A survey on self-supervised learning: Algorithms, applications, and future trends. *IEEE Transactions on Pattern Analysis and Machine Intelligence*, pages 1–20, 2024. 14
- [31] Charles Guille-Escuret, Pau Rodriguez, David Vazquez, Ioannis Mitliagkas, and Joao Monteiro. Cadet: Fully self-supervised out-of-distribution detection with contrastive learning, 2023. 1
- [32] Suchin Gururangan, Ana Marasović, Swabha Swayamdipta, Kyle Lo, Iz Beltagy, Doug Downey, and Noah A. Smith. Don’t stop pretraining: Adapt language models to domains and tasks, 2020. 8
- [33] Kaiming He, Xiangyu Zhang, Shaoqing Ren, and Jian Sun. Deep residual learning for image recognition, 2015. 3
- [34] Kaiming He, Haoqi Fan, Yuxin Wu, Saining Xie, and Ross Girshick. Momentum contrast for unsupervised visual representation learning, 2020. 3
- [35] Dan Hendrycks and Kevin Gimpel. A baseline for detecting misclassified and out-of-distribution examples in neural networks. 2016. 16
- [36] Dan Hendrycks, Mantas Mazeika, Saurav Kadavath, and Dawn Song. Using self-supervised learning can improve model robustness and uncertainty, 2019. 1, 2, 17
- [37] S.C. Huang, A. Pareek, M. Jensen, et al. Self-supervised learning for medical image classification: a systematic review and implementation guidelines. *npj Digital Medicine*, 6(74), 2023. 3
- [38] Zhe Huang, Ruijie Jiang, Shuchin Aeron, and Michael C. Hughes. Systematic comparison of semi-supervised and self-supervised learning for medical image classification, 2024. 1, 2, 13
- [39] Marie Humbert-Droz, Pritam Mukherjee, and Olivier Gevaert. Strategies to address the lack of labeled data for supervised machine learning training with electronic health records: Case study for the extraction of symptoms from clinical notes. *JMIR Medical Informatics*, 10(3):e32903, 2022. 1
- [40] Mingu Kang, Heon Song, Seonwook Park, Donggeun Yoo, and Sérgio Pereira. Benchmarking self-supervised learning on diverse pathology datasets, 2023. 1, 2
- [41] Jakob Nikolas Kather, Johannes Krisam, Pornpimol Charoentong, Tom Luedde, Esther Herpel, Cleo Aron Weis, Timo Gaiser, Alexander Marx, Nektarios A. Valous, Dyke Ferber, Lina Jansen, Constantino Carlos Reyes-Aldasoro, Inka Zörnig, Dirk Jäger, Hermann Brenner, Jenny Chang-Claude, Michael Hoffmeister, and Niels Halama. Predicting survival from colorectal cancer histology slides using deep learning: A retrospective multicenter study. *PLOS Medicine*, 16(e1002730), 2019. 14
- [42] Daniel S. Kermany, Michael Goldbaum, Wenjia Cai, Carolina C.S. Valentim, Huiying Liang, Sally L. Baxter, Alex McKeown, Ge Yang, Xiaokang Wu, Fangbing Yan, et al. Identifying medical diagnoses and treatable diseases by image-based deep learning. *Cell*, 172:1122–1131.e9, 2018. 14
- [43] Umar Khalid, Ashkan Esmaceli, Nazmul Karim, and

- Nazanin Rahnavard. Rodd: A self-supervised approach for robust out-of-distribution detection, 2022. 1
- [44] Alexander Kolesnikov, Xiaohua Zhai, and Lucas Beyer. Revisiting self-supervised visual representation learning, 2019. 3
- [45] Sonja Kunzmann, Mathias Öttl, Prathmesh Madhu, Felix Denzinger, and Andreas Maier. An unobtrusive quality supervision approach for medical image annotation, 2022. 1
- [46] Kimin Lee, Kibok Lee, Honglak Lee, and Jinwoo Shin. A simple unified framework for detecting out-of-distribution samples and adversarial attacks, 2018. 3, 16, 17
- [47] Haoliang Li, YuFei Wang, Renjie Wan, Shiqi Wang, Tie-Qiang Li, and Alex Kot. Domain generalization for medical imaging classification with linear-dependency regularization. *Advances in neural information processing systems*, 33:3118–3129, 2020. 2
- [48] Jingyao Li, Pengguang Chen, Shaozuo Yu, Zexin He, Shu Liu, and Jiaya Jia. Rethinking out-of-distribution (ood) detection: Masked image modeling is all you need, 2023. 1, 2, 17
- [49] Hong Liu, Jeff Z. HaoChen, Adrien Gaidon, and Tengyu Ma. Self-supervised learning is more robust to dataset imbalance, 2022. 8
- [50] Ruhan Liu, Xiangning Wang, Qiang Wu, Ling Dai, Xi Fang, Tao Yan, Jaemin Son, Shiqi Tang, Jiang Li, Zijian Gao, Adrian Galdran, J. M. Poorneshwaran, Hao Liu, Jie Wang, Yerui Chen, Prasanna Porwal, Gavin Siew Wei Tan, Xi-aokang Yang, Chao Dai, Haitao Song, Mingang Chen, Huating Li, Weiping Jia, Dinggang Shen, Bin Sheng, and Ping Zhang. Deepdrid: Diabetic retinopathy—grading and image quality estimation challenge. *Patterns*, 3:100512, 2022. 14
- [51] Weitang Liu, Xiaoyun Wang, John D. Owens, and Yixuan Li. Energy-based out-of-distribution detection, 2020. 16
- [52] Vebjorn Ljosa, Katherine L. Sokolnicki, and Anne E. Carpenter. Annotated high-throughput microscopy image sets for validation. *Nature Methods*, 9(7):637, 2012. 14
- [53] Ilya Loshchilov and Frank Hutter. Decoupled weight decay regularization, 2019. 15
- [54] Markus Marks, Manuel Knott, Neehar Kondapaneni, Elijah Cole, Thijs Defraeye, Fernando Perez-Cruz, and Pietro Perona. A closer look at benchmarking self-supervised pre-training with image classification, 2024. 2
- [55] Christos Matsoukas, Johan Fredin Haslum, Magnus Söderberg, and Kevin Smith. Is it time to replace cnns with transformers for medical images?, 2021. 2, 3, 9
- [56] Christos Matsoukas, Johan Fredin Haslum, Moein Sorkhei, Magnus Söderberg, and Kevin Smith. What makes transfer learning work for medical images: Feature reuse & other factors, 2022. 2
- [57] Sina Mohseni, Mandar Pitale, Jbs Yadawa, and Zhangyang Wang. Self-supervised learning for generalizable out-of-distribution detection. In *AAAI Conference on Artificial Intelligence*, 2020. 1, 2
- [58] Mohammad Amin Morid, Alireza Borjali, and Guilherme Del Fiol. A scoping review of transfer learning research on medical image analysis using imagenet. *Computers in Biology and Medicine*, 128:104115, 2021. 2
- [59] Vivek Narayanaswamy, Yamen Mubarka, Rushil Anirudh, Deepta Rajan, and Jayaraman J. Thiagarajan. Exploring inlier and outlier specification for improved medical ood detection. In *Proceedings of the IEEE/CVF International Conference on Computer Vision (ICCV) Workshops*, pages 4589–4598, 2023. 2, 13
- [60] Ece Ozkan and Xavier Boix. Multi-domain improves out-of-distribution and data-limited scenarios for medical image analysis, 2024. 2, 13
- [61] Maithra Raghu, Chiyuan Zhang, Jon Kleinberg, and Samy Bengio. Transfusion: Understanding transfer learning for medical imaging, 2019. 8
- [62] Mert Bulent Sariyildiz, Yannis Kalantidis, Karteek Alahari, and Diane Larlus. No reason for no supervision: Improved generalization in supervised models, 2023. 8
- [63] Marc-Andre Schulz, Bertrand Thirion, Alexandre Gramfort, Gaël Varoquaux, and Danilo Bzdok. Label scarcity in biomedicine: Data-rich latent factor discovery enhances phenotype prediction, 2021. 1
- [64] Vikash Sehwal, Mung Chiang, and Prateek Mittal. Ssd: A unified framework for self-supervised outlier detection, 2021. 2
- [65] Kihyuk Sohn, David Berthelot, Nicholas Carlini, Zizhao Zhang, Han Zhang, Colin A Raffel, Ekin Dogus Cubuk, Alexey Kurakin, and Chun-Liang Li. Fixmatch: Simplifying semi-supervised learning with consistency and confidence. In *Advances in Neural Information Processing Systems*, pages 596–608. Curran Associates, Inc., 2020. 15
- [66] Igor Susmelj, Matthias Heller, Philipp Wirth, Jeremy Prescott, Malte Ebner, and et al. Lightly. 15
- [67] Mohammad Reza Hosseinzadeh Taher, Fatemeh Haghighi, Ruibin Feng, Michael B. Gotway, and Jianming Liang. A systematic benchmarking analysis of transfer learning for medical image analysis, 2021. 3, 8
- [68] Nima Tajbakhsh, Jae Y. Shin, Suryakanth R. Gurudu, R. Todd Hurst, Christopher B. Kendall, Michael B. Gotway, and Jianming Liang. Convolutional neural networks for medical image analysis: Full training or fine tuning? *IEEE Transactions on Medical Imaging*, 35(5):1299–1312, 2016. 2, 3
- [69] Philipp Tschandl, Cliff Rosendahl, and Harald Kittler. The ham10000 dataset, a large collection of multi-source dermatoscopic images of common pigmented skin lesions. *Scientific Data*, 5:1–9, 2018. 14
- [70] Stefano Woerner, Arthur Jaques, and Christian F. Baumgartner. A comprehensive and easy-to-use multi-domain multi-task medical imaging meta-dataset (medimeta), 2024. 2
- [71] Junfei Xiao, Yutong Bai, Alan Yuille, and Zongwei Zhou. Delving into masked autoencoders for multi-label thorax disease classification, 2022. 1, 4
- [72] Xuanang Xu, Fugen Zhou, Bo Liu, Dongshan Fu, and Xiangzhi Bai. Efficient multiple organ localization in ct images using 3d region proposal network. *IEEE Transactions on Medical Imaging*, 38(8):1885–1898, 2019. 14
- [73] Siyuan Yan, Zhen Yu, Chi Liu, Lie Ju, Dwarikanath Mahapatra, Brigid Betz-Stablein, Victoria Mar, Monika Janda, Peter Soyer, and Zongyuan Ge. Prompt-driven latent domain

- generalization for medical image classification. *IEEE Transactions on Medical Imaging*, 2024. [2](#)
- [74] Jiancheng Yang, Rui Shi, Donglai Wei, Zequan Liu, Lin Zhao, Bilian Ke, Hanspeter Pfister, and Bingbing Ni. Medmnist v2 - a large-scale lightweight benchmark for 2d and 3d biomedical image classification. *Scientific Data*, 10(1), 2023. [3](#), [13](#), [16](#)
- [75] Karina Zadorozhny, Patrick Thorat, Paul Elbers, and Giovanni Cinà. Out-of-distribution detection for medical applications: Guidelines for practical evaluation, 2022. [2](#)
- [76] Muhammad Zaid, Shafaqat Ali, Mohsen Ali, Sarfaraz Hussein, Asma Saadia, and Waqas Sultani. Identifying out of distribution samples for skin cancer and malaria images. *Biomedical Signal Processing and Control*, 78:103882, 2022. [2](#)
- [77] Jure Zbontar, Li Jing, Ishan Misra, Yann LeCun, and Stéphane Deny. Barlow twins: Self-supervised learning via redundancy reduction, 2021. [3](#), [15](#)
- [78] Chongzhi Zhang, Mingyuan Zhang, Shanghang Zhang, Daisheng Jin, Qiang Zhou, Zhongang Cai, Haiyu Zhao, Xianglong Liu, and Ziwei Liu. Delving deep into the generalization of vision transformers under distribution shifts, 2021. [6](#)
- [79] Yu Zhang, Jing Chen, Xiangxun Ma, Gang Wang, Uzair Aslam Bhatti, and Mengxing Huang. Interactive medical image annotation using improved attention u-net with compound geodesic distance. *Expert Syst. Appl.*, 237(PA), 2024. [1](#)
- [80] Mingkai Zheng, Shan You, Fei Wang, Chen Qian, Changshui Zhang, Xiaogang Wang, and Chang Xu. Resl: Relational self-supervised learning with weak augmentation, 2021. [1](#), [3](#), [14](#), [16](#)
- [81] Yuanyi Zhong, Haoran Tang, Junkun Chen, Jian Peng, and Yu-Xiong Wang. Is self-supervised learning more robust than supervised learning?, 2022. [2](#)
- [82] Haoran Zhu, Boyuan Chen, and Carter Yang. Understanding why vit trains badly on small datasets: An intuitive perspective, 2023. [4](#)

Appendix

A . Dataset Details	13
B . Method Details	14
C . Implementation Details	15
C.1 Pre-Training	15
C.2 Data Augmentations	15
C.3 Linear Evaluation	16
C.4 Loss Criterion and Evaluation Metrics	16
C.5 Out-of-distribution Detection	16
D . Additional Analysis	17
D.1 In-Domain Performance	17
D.1.1 Linear Evaluation with All Labels	17
D.1.2 Linear Evaluation with Limited Labels	21
D.2 Out-of-distribution Detection	26
D.2.1 Effect of SSL Method	26
D.2.2 Effect of Backbone Architecture	27
D.2.3 Effect of Initialization	29
D.2.4 Effect of Multi-domain Datasets	30
D.3 Generalizability	39
D.4 KNN Evaluation	44
E . Conclusion & Future Work	46

A. Dataset Details

MedMNIST is a medical imaging dataset comprising 18 sub-datasets from various medical domains [74]. For our work, we focus on 12 of these sub-datasets, specifically those containing 2D images. MedMNIST offers a diverse representation of medical imaging modalities and supports multiple classification tasks, making it a comprehensive resource for benchmarking. Its extensive adoption in medical image recognition research [21, 38, 59, 60] further establishes its value as a standard benchmark. Accordingly, we utilize the 2D subset of MedMNIST, referred to as MedMNIST2D, which we simply denote as MedMNIST in the paper.

The MedMNIST dataset was initially introduced in a resolution of 28×28 pixels and has since been expanded by MedMNIST+ to additionally include 64×64 , 128×128 , and 224×224 resolutions. Due to limited GPU memory, we opted to use the 64×64 resolution version of the dataset throughout our experiments. As lower resolutions are also shown to yield reasonable accuracies in previous research [38, 74], we do not sacrifice much by not using a larger resolution. Detailed information regarding each dataset, such as data source, domain, classification task type (including the number of classes), and publicly available data splits that correspond to our benchmark are provided in Table 5.

The datasets encompass diverse imaging modalities, including X-ray, CT, ultrasound, fundus camera, dermatoscope, and microscope images. Beyond spanning multiple medical domains, these modalities vary in technical characteristics such as color channels and level of detail. This diversity makes it particularly well-suited for self-supervised learning tasks, as it captures the unique challenges and nuances of different medical imaging fields. Such variability enables the development and rigorous evaluation of models that must generalize effectively across different image types—a critical requirement for robust medical image analysis. Leveraging MedMNIST not only facilitates the creation of domain-agnostic representations but also provides a platform for testing these representations across a wide range of medical imaging scenarios.

The classification tasks supported in MedMNIST are diverse, encompassing multi-class classification (MC), binary classification (BC), and ordinal regression (OR). Multi-class classification treats each class as distinct and independent, without accounting for relationships among them, while binary classification is a specific case of multi-class classification involving only two classes. Ordinal regression, on the other hand, is a regression task where the output represents a discrete value reflecting the ordered relationship between classes. In our experiments, we treat ordinal regression as multi-class classification by assigning each ordinal level as a separate class. While this method loses information on the ordinal relationships between classes, it enables consistent evaluation across all datasets in our benchmark. We excluded ChestMNIST, as explained in Section 3, since it involves multi-label classification, while our study focuses solely on single-label classification tasks.

Dataset	Data Modality	Task (# Classes / Labels)	# Samples	# Training / Validation / Test
PathMNIST [41]	Colon Pathology	MC (9)	107,180	89,996 / 10,004 / 7,180
DermaMNIST [17, 69]	Dermatoscope	MC (7)	10,015	7,007 / 1,003 / 2,005
OCTMNIST [42]	Retinal OCT	MC (4)	109,309	97,477 / 10,832 / 1,000
PneumoniaMNIST [42]	Chest X-Ray	BC (2)	5,856	4,708 / 524 / 624
RetinaMNIST [50]	Fundus Camera	OR (5)	1,600	1,080 / 120 / 400
BreastMNIST [4]	Breast Ultrasound	BC (2)	780	546 / 78 / 156
BloodMNIST [1]	Blood Cell Microscope	MC (8)	17,092	11,959 / 1,712 / 3,421
TissueMNIST [52]	Kidney Cortex Microscope	MC (8)	236,386	165,466 / 23,640 / 47,280
OrganAMNIST [10, 72]	Abdominal CT	MC (11)	58,850	34,581 / 6,491 / 17,778
OrganCMNIST [10, 72]	Abdominal CT	MC (11)	23,660	13,000 / 2,392 / 8,268
OrganSMNIST [10, 72]	Abdominal CT	MC (11)	25,221	13,940 / 2,452 / 8,829

Table 5. Overview of the MedMNIST2D datasets employed in our benchmarking study, which include tasks involving multiclass classification, binary classification, and ordinal regression.

B. Method Details

Self-supervised learning (SSL) techniques are a subset of unsupervised methods focused on extracting meaningful representations from unlabeled data. These techniques have gained significant attention due to their ability to leverage large datasets and improve model performance on various downstream tasks [30].

SSL methods can be broadly classified into generative and discriminative approaches. Generative methods aim to reconstruct or generate data samples to capture meaningful representations, whereas discriminative methods focus on distinguishing between data points to learn robust and invariant features. In this study, we focus on discriminative self-supervised learning methods, which are specifically designed to maximize the similarity between augmented versions of the same image (“positive pairs”) while minimizing the similarity with other images (“negative pairs”). More recent approaches eliminate the need for negative pairs, instead focusing solely on maximizing the similarity between positive pairs. These methods enable the model to learn robust features, which can then be used in many downstream visual recognition tasks. We consider the following discriminative SSL methods:

SimCLR [14] (Simple Framework for Contrastive Learning of Visual Representations) is a contrastive SSL method that learns representations by maximizing the agreement between differently augmented views of the same image. SimCLR utilizes a contrastive loss function, specifically the normalized temperature-scaled cross-entropy (NT-Xent) loss, to increase the similarity between augmented pairs while minimizing it with other samples.

DINO [13] (Distillation with No Labels) employs a teacher-student architecture to learn from self-distilled knowledge. *Self-distillation* is a process where given two different views of a sample image, the student model directly predicts the output of the teacher model. The teacher model has the same architecture as the student, but its parameters are updated using a momentum encoder on the student’s parameters. Thus, the student model “distills” knowledge from the teacher and extracts similar features for different views, without needing labels or negative samples.

BYOL [29] (Bootstrap Your Own Latent) leverages two neural networks, an *online network* and a *target network*, to iteratively improve each other’s representations. BYOL does not rely on negative pairs; instead, it minimizes the difference between the two networks’ representations of the same image. The target network is updated using a moving average of the online network parameters, which in turn is updated via back-propagation.

ReSSL [80] (Relational Self-Supervised Learning) introduces a relation metric to better capture nuanced relationships between different samples. That is, instead of strictly enforcing positive and negative pairs as in contrastive SSL, ReSSL calculates the relationship distribution among the samples, and minimizes the KL divergence between those of the views of a sample. This approach enables ReSSL to learn more nuanced inter-sample relationships.

MoCo v3 [15] (Momentum Contrast v3) builds upon the original Momentum Contrast framework, which frames contrastive learning as a dictionary look-up task. In this approach, encoders are trained to ensure that the representation of a *query* (i.e. a data sample) is similar to its corresponding *key* (i.e. a positive sample) while being dissimilar to other samples (“negative keys”). Earlier versions of MoCo utilized a dynamic and memory-efficient dictionary, maintaining key representations in a queue that was updated on-the-fly using a momentum-updated encoder. MoCo v3 simplifies this design by removing the memory queue entirely and instead leveraging a purely end-to-end transformer-based architecture.

VICReg [8] (Variance-Invariance-Covariance Regularization) avoids using negative samples or asymmetric networks. It prevents representation collapse by combining three key terms: a variance term to ensure diversity across feature dimensions, an invariance term to align features of augmented views of the same image, and a covariance term to reduce redundancy by decorrelating feature dimensions. Together, these components enable the learning of robust and informative representations.

Barlow Twins [77] is another SSL method that aims to prevent representation collapse by employing an objective function inspired by neuroscientist H. Barlow’s *redundancy-reduction* principle. Specifically, the cross-correlation between the outputs of a Siamese network are made as close as possible to the identity matrix. This approach reduces redundancy across feature dimensions while encouraging different views of the same sample to have similar representations, thereby learning robust and diverse features.

NNCLR [23] (Nearest-Neighbor Contrastive Learning of Representations) is a contrastive SSL method that incorporates nearest neighbors as additional positive pairs. In addition to using augmented views of a sample, NNCLR finds the closest semantic matches in a dynamically updated support set and uses them as extra positive pairs in contrastive loss. This reduces the reliance on heavy augmentations and enables the model to learn features that are more stable under larger semantic variations.

C. Implementation Details

C.1 Pre-Training

For training, we employ mini-batch gradient descent using the AdamW optimizer [53] and a cosine learning rate schedule [65] beginning with a 10-epoch linear warm-up from 3×10^{-5} . To ensure fairness, we conduct a grid search using learning rates of the form 3×10^x , where $x \in \{-1, -2, -3, -4\}$, and weight decays of the form 1×10^x , where $x \in \{-3, -4, -5\}$. We select the model with the best performance on the downstream validation set. The batch size is set to 256, with coefficients for computing running averages of the gradient and its square as $\beta_1 = 0.9$ and $\beta_2 = 0.95$ respectively. We train the models for a total of 400 epochs.

For our experimental evaluation with self-supervised IMAGENET1K pre-training, we employ four established methods: MoCo v3, SimCLR, BYOL, and DINO. The MoCo v3 weights were obtained from the `mmselfsup` library [18], specifically utilizing the model variant trained for 100 epochs with a batch size of 4,096 on the IMAGENET1K dataset. For SimCLR, BYOL, and DINO, we leverage pre-trained weights from the `LightlySSL` framework [66]. These models were trained for 100 epochs, with varying batch sizes: 256 for SimCLR and BYOL, and 128 for DINO.

In the IMAGENET1K initialization experiments, the backbone weights were initialized from the IMAGENET1K checkpoint, while auxiliary components (such as the projection head, classifier, and other task-specific layers) were discarded. We conducted experiments with multi-domain datasets using 5 SSL methods, including SimCLR, DINO, BYOL, ReSSL, and MoCo v3. First, we merged the datasets and pre-trained the encoder using the selected SSL method. Then, hyperparameter selection was performed based on the average performance of linear classifiers, which were trained independently on each constituent dataset.

C.2 Data Augmentations

All of the used SSL methods employ a sequence of image transformations to obtain different views from a sample. In our experiments, we have used augmentation configurations provided in the `solo-learn` library, as described below. Specifically, we have used the respective configurations of VICReg and ReSSL and the default *asymmetric* configuration for the other methods. *Asymmetric* here refers to the two contrasting views obtained from a single image sample. This default configuration in question applies the following augmentations (denoted as T) twice to obtain the two views:

Random Resized Crop (T_{RRC}): With probability 1, a random crop of the image is extracted. The scale of the crop is uniformly sampled from the range $[0.2, 1]$, while maintaining the aspect ratio. The cropped region is then resized to the original image dimensions.

Color Jitter (T_{CJ}): With probability 0.8, the image undergoes random adjustments in brightness, contrast, saturation, and hue. The maximum intensity of these adjustments is set to 0.4 for brightness and contrast, 0.2 for saturation, and 0.1 for hue.

Grayscale Conversion (T_{Gray}): With probability 0.2, the RGB image is converted to grayscale by computing the luminance L of each pixel using the formula $L = 0.299R + 0.587G + 0.114B$ where R , G , and B are the red, green, and blue channel values, respectively.

Gaussian Blur (T_{GB}): Applied with probability 1, the image is blurred using a Gaussian filter. The standard deviation σ of the Gaussian kernel is uniformly sampled from the range $[0.1, 2]$.

Solarization (T_S): Solarization is applied asymmetrically across augmented views. For one view, it is applied with probability 0.2, and for the other view, it is not applied (probability 0). The transformation inverts the pixel intensities for pixels with values $L \geq 128$ (assuming pixel intensities in the range $[0, 255]$) using $L' = 255 - L$ where L is the original pixel intensity and L' is the transformed intensity.

Horizontal Flip (T_F): With probability 0.5, the image is flipped horizontally.

The transformation sequence for ReSSL differs since it classifies the augmentations as *weak* and *contrastive* [80]. In the contrastive augmentations, the scale for T_{RRC} is chosen uniformly from range $[0.08, 1]$, T_{GB} is applied with probability 0.5 and T_S is not applied. Rest of the augmentations are the same as above. For the weak augmentation the scale for T_{RRC} is again chosen uniformly from range $[0.08, 1]$, T_F is applied with probability 0.5 and there are no other augmentations applied.

VICReg augmentations also differ since they are applied *symmetrically*, that is, with the same parameters and probabilities for two different views. T_{GB} is applied with probability 0.5 and T_S applied with probability 0.1 for both views. The rest of the augmentations is the same as the default configuration.

C.3 Linear Evaluation

We utilize the train, validation, and test set splits as provided by MedMNIST. All images are converted to RGB format and normalized. We use stochastic gradient descent with a step learning rate scheduler, decaying at epochs $[60, 80]$. For a fair comparison, we conduct a grid search over learning rates $\{0.1, 0.01, 0.001\}$ and weight decay values $\{0, 0.1, 0.01\}$, selecting the best hyperparameters based on validation set performance. The test set is used only once at the end to evaluate the classifier with the optimal hyperparameters. We train the linear classifier for 100 epochs. We report the mean and standard deviation of performance metrics on downstream tasks over five runs. Assuming a t -distribution, we calculate the confidence intervals as $\bar{x} \pm t \times \text{SE}$, where \bar{x} represents the mean metric and SE is the standard error, calculated as $\text{SE} = \frac{\text{SD}}{\sqrt{n}}$ where n is the number of trials and SD is the standard deviation.

C.4 Loss Criterion and Evaluation Metrics

Our downstream tasks include multiclass classification (MC), binary classification (BC), and ordinal regression (OR). To maintain consistency with the experiments conducted by Yang et al. [74], we used the cross-entropy loss for all classification tasks, including ordinal regression. We adopted the same evaluation metrics as in the previous work, including accuracy (ACC) and the area under the receiver operating characteristic curve (AUC or AUROC), to assess the models' ability to differentiate between classes. For multiclass classification, we employ macro averaging, calculating the metric independently for each class and then averaging the results. We used different numbers of epochs for pre-training, to accommodate the differences in the training set sizes.

C.5 Out-of-distribution Detection

A sample x is considered *in-distribution* if drawn from the training distribution \mathcal{P}_{ID} , and *out-of-distribution* if drawn from a different distribution $\mathcal{P}_{\text{OOD}} \neq \mathcal{P}_{\text{ID}}$, representing different domains or modalities. To determine whether a sample originates from the in-distribution (ID) \mathcal{P}_{ID} or out-of-distribution (OOD) \mathcal{P}_{OOD} , we primarily adopt the *Mahalanobis Distance* [46] as the core metric. While energy-based [51] and softmax-based [35] methods are also considered, our experiments consistently demonstrate that the Mahalanobis distance-based approach yields superior OOD detection performance. This approach computes the distance between the extracted feature vector of an input sample and the nearest class-conditional Gaussian distribution, facilitating the assignment of pseudo-labels to features. Formally, let $\mathbf{f}(x) \in \mathbb{R}^d$ denote the feature representation of input x extracted by a trained encoder. Assuming that the feature representations of each class follow a multivariate Gaussian distribution, we define the class-conditional distributions as:

$$p(\mathbf{f}(x)|y = c) = \mathcal{N}(\mathbf{f}(x)|\boldsymbol{\mu}_c, \Sigma),$$

where $\mu_c \in \mathbb{R}^d$ and $\Sigma \in \mathbb{R}^{d \times d}$ represent the class mean and a shared covariance matrix, respectively. These parameters are estimated empirically from the training data $\mathcal{P}_{\text{ID}}^{\text{train}}$:

$$\mu_c = \frac{1}{N_c} \sum_{i:y_i=c} \mathbf{f}(x_i), \quad \Sigma = \frac{1}{N} \sum_{c=1}^m \sum_{i:y_i=c} (\mathbf{f}(x_i) - \mu_c)(\mathbf{f}(x_i) - \mu_c)^\top,$$

where N_c is the number of training samples in class c , and N is the total number of training samples.

The Mahalanobis distance between a sample’s feature vector $\mathbf{f}(x)$ and a class-conditional distribution is given by:

$$D_{\text{M}}(x, c) = \sqrt{(\mathbf{f}(x) - \mu_c)^\top \Sigma^{-1} (\mathbf{f}(x) - \mu_c)}$$

The confidence score $S(x)$ for an input sample is defined as the negative of the minimum Mahalanobis distance:

$$S(x) = - \min_c D_{\text{M}}(x, c)$$

To assess the effectiveness of different SSL methods for OOD detection, we evaluate the widely used AUROC and AUPR metrics, both of which are threshold-independent [26, 36, 48]. The performance is assessed by comparing Mahalanobis-based scores derived from $\mathcal{P}_{\text{ID}}^{\text{test}}$ and \mathcal{P}_{OOD} . Following the framework of [46], we validate the method across various datasets and configurations. Specifically, models trained on \mathcal{P}_{ID} are evaluated against other 10 MedMNIST datasets, yielding $11 \times 10 \times 2$ (initializations) $\times 2$ (backbone types) = 440 OOD detection scores per each method, backbone, and initialization combination.

This comprehensive evaluation framework allows us to rigorously compare methods across diverse settings, highlighting the robustness and consistency of the Mahalanobis distance-based approach in handling OOD detection. If further clarity is needed on the methodology, readers are encouraged to refer to the foundational work in [46].

D. Additional Analysis

D.1 In-Domain Performance

D.1.1 Linear Evaluation with All Labels The in-domain performance of the self-supervised learning methods using ResNet-50 with random initialization is presented in Section 4.1 in Table 2. Additional results for ResNet-50 with IMAGENET1K initialization, ViT-Small with random initialization, and ViT-Small with IMAGENET1K initialization are provided in Tables 5, 6, and 8 respectively. Similar to Table 2, Area Under the Curve (AUC) and accuracy (ACC) metrics are reported, and supervised learning results are provided for reference. The highest accuracy scores among the SSL methods are highlighted in **green**, and conversely, the lowest ones are highlighted in **red**.

These tables illustrate how initialization and architecture choices impact the performance of different SSL methods. Notably, DINO performs significantly better with IMAGENET1K initialization on both ResNet-50 and ViT-Small, whereas it ranks among the worst with random initialization. Moreover, compared to the random initialization results for ResNet-50 in Table 2, SimCLR achieves notably higher accuracy with ViT-Small. Further analyses on the impact of initialization and backbone architecture are provided in Tables 9 and 10, respectively. Additionally, Figure 11 shows the performance differences between random and IMAGENET1K initialization for each dataset and SSL method.

Method	PathMNIST		DermaMNIST		OCTMNIST		PneumoniaMNIST		RetinaMNIST	
	AUC \uparrow	ACC \uparrow	AUC \uparrow	ACC \uparrow	AUC \uparrow	ACC \uparrow	AUC \uparrow	ACC \uparrow	AUC \uparrow	ACC \uparrow
Supervised (random init.)	96.22 \pm 0.04	79.57 \pm 0.15	86.52 \pm 0.58	73.99 \pm 0.35	91.90 \pm 0.29	70.04 \pm 0.14	84.81 \pm 3.03	83.71 \pm 0.52	72.60 \pm 0.74	51.95 \pm 0.60
Supervised (IMAGENET1K init.)	98.72 \pm 0.15	92.53 \pm 0.09	92.76 \pm 0.20	80.49 \pm 0.20	92.95 \pm 1.35	80.16 \pm 0.11	94.69 \pm 1.69	86.69 \pm 0.24	72.02 \pm 0.09	51.05 \pm 0.94
SimCLR	99.33 \pm 0.01	92.88 \pm 0.11	94.36 \pm 0.06	78.85 \pm 0.08	97.41 \pm 0.07	77.38 \pm 0.57	96.54 \pm 0.48	93.30 \pm 1.71	72.71 \pm 3.22	49.50 \pm 4.36
DINO	99.40 \pm 0.01	94.09 \pm 0.06	94.39 \pm 0.09	78.85 \pm 0.72	97.24 \pm 0.16	79.28 \pm 1.03	97.71 \pm 1.12	88.39 \pm 2.39	74.65 \pm 0.73	50.80 \pm 1.75
BYOL	98.77 \pm 0.03	92.18 \pm 0.18	95.25 \pm 0.02	80.58 \pm 0.23	93.40 \pm 0.09	70.24 \pm 0.35	99.51 \pm 0.04	93.52 \pm 0.36	72.18 \pm 1.97	51.30 \pm 2.66
ReSSL	99.34 \pm 0.03	92.51 \pm 0.22	94.80 \pm 0.21	79.21 \pm 0.73	96.08 \pm 0.04	74.78 \pm 0.20	98.51 \pm 0.45	92.30 \pm 1.15	73.40 \pm 1.38	50.55 \pm 2.09
MoCo v3	99.42 \pm 0.02	94.14 \pm 0.12	94.86 \pm 0.02	79.71 \pm 0.19	97.27 \pm 0.05	78.22 \pm 0.41	98.88 \pm 0.23	93.87 \pm 1.41	70.92 \pm 1.37	48.95 \pm 1.54
VICReg	98.94 \pm 0.04	91.60 \pm 0.18	91.52 \pm 0.28	75.13 \pm 0.45	95.24 \pm 0.14	76.18 \pm 0.83	98.36 \pm 0.14	94.16 \pm 0.62	69.12 \pm 2.23	46.70 \pm 2.87
Barlow Twins	99.01 \pm 0.04	91.63 \pm 0.14	93.29 \pm 0.13	77.05 \pm 0.29	96.74 \pm 0.18	76.12 \pm 1.14	99.28 \pm 0.06	94.19 \pm 0.26	70.16 \pm 2.27	48.30 \pm 2.66
NNCLR	99.22 \pm 0.02	92.73 \pm 0.10	94.65 \pm 0.10	78.48 \pm 0.35	95.57 \pm 0.11	75.72 \pm 0.70	99.38 \pm 0.03	94.16 \pm 0.30	51.56 \pm 0.00	11.50 \pm 0.00

Method	BreastMNIST		BloodMNIST		TissueMNIST		OrganAMNIST		OrganCMNIST		OrganSMNIST	
	AUC \uparrow	ACC \uparrow	AUC \uparrow	ACC \uparrow	AUC \uparrow	ACC \uparrow	AUC \uparrow	ACC \uparrow	AUC \uparrow	ACC \uparrow	AUC \uparrow	ACC \uparrow
Supervised (random init.)	75.68 \pm 0.31	77.82 \pm 0.71	98.90 \pm 0.44	93.76 \pm 0.15	87.98 \pm 7.65	66.53 \pm 16.46	98.87 \pm 0.26	89.90 \pm 0.85	97.89 \pm 0.21	88.26 \pm 0.09	93.29 \pm 0.33	73.65 \pm 0.08
Supervised (IMAGENET1K init.)	85.69 \pm 3.42	87.82 \pm 1.26	99.72 \pm 0.16	97.23 \pm 0.46	87.01 \pm 0.63	67.72 \pm 0.04	99.52 \pm 0.05	95.21 \pm 0.05	99.62 \pm 0.08	94.76 \pm 0.05	95.09 \pm 1.27	82.28 \pm 0.24
SimCLR	89.99 \pm 1.51	87.17 \pm 3.23	99.91 \pm 0.00	98.01 \pm 0.06	89.95 \pm 0.01	61.69 \pm 0.03	99.61 \pm 0.01	92.62 \pm 0.22	99.16 \pm 0.13	89.73 \pm 0.60	97.23 \pm 0.11	77.34 \pm 0.11
DINO	90.75 \pm 1.18	86.41 \pm 1.18	99.91 \pm 0.01	98.03 \pm 0.30	91.01 \pm 0.01	63.81 \pm 0.05	99.70 \pm 0.03	92.63 \pm 0.83	99.46 \pm 0.01	91.84 \pm 0.09	97.66 \pm 0.02	78.08 \pm 0.28
BYOL	88.25 \pm 1.72	83.20 \pm 2.84	99.90 \pm 0.01	98.39 \pm 0.16	87.70 \pm 0.02	58.87 \pm 0.12	99.34 \pm 0.05	88.47 \pm 0.74	98.27 \pm 0.04	87.70 \pm 0.24	95.51 \pm 0.03	74.41 \pm 0.07
ReSSL	85.55 \pm 1.04	85.38 \pm 1.31	99.89 \pm 0.00	97.85 \pm 0.07	88.90 \pm 0.01	59.37 \pm 0.04	99.44 \pm 0.08	90.77 \pm 0.58	99.14 \pm 0.01	89.01 \pm 0.08	97.29 \pm 0.04	77.38 \pm 0.15
MoCo v3	86.65 \pm 1.39	86.66 \pm 2.66	99.92 \pm 0.01	98.15 \pm 0.03	89.34 \pm 0.01	60.56 \pm 0.08	99.38 \pm 0.03	89.71 \pm 0.29	98.55 \pm 0.06	88.27 \pm 0.41	96.29 \pm 0.05	76.27 \pm 0.27
VICReg	90.75 \pm 1.72	87.17 \pm 0.80	99.37 \pm 0.08	96.41 \pm 0.32	87.36 \pm 0.00	57.24 \pm 0.03	97.92 \pm 0.03	87.39 \pm 0.10	96.09 \pm 0.33	84.54 \pm 0.49	94.20 \pm 0.01	73.69 \pm 0.22
Barlow Twins	85.73 \pm 2.32	81.53 \pm 3.62	99.86 \pm 0.01	97.51 \pm 0.07	89.24 \pm 0.00	60.21 \pm 0.07	98.84 \pm 0.22	88.68 \pm 0.50	98.54 \pm 0.20	88.19 \pm 0.28	95.80 \pm 0.11	75.85 \pm 0.21
NNCLR	91.22 \pm 1.08	88.20 \pm 2.29	99.90 \pm 0.00	98.11 \pm 0.09	89.21 \pm 0.00	60.74 \pm 0.04	98.77 \pm 0.16	89.57 \pm 0.40	98.10 \pm 0.32	87.15 \pm 0.61	96.12 \pm 0.15	75.13 \pm 0.06

Table 8. In-domain performance of the SSL methods using ViT-Small with IMAGENET1K initialization.

Effect of Initialization with respect to Method and Dataset: Figure 11 illustrates the impact of random versus IMAGENET1K initialization on the performance of various SSL methods across diverse datasets, evaluated on both ResNet-50 and ViT-Small backbones. IMAGENET1K initialization generally enhances model accuracy, although the extent of improvement differs across methods and datasets. Some datasets receive greater gains in general such as BreastMNIST and OctMNIST. However, it can also be seen that TissueMNIST and OrganAMNIST prefer random initialization on ViT backbone most of the time as an exception. These insights suggest that selecting an appropriate pre-training method and initialization strategy is crucial for optimizing performance on particular tasks, especially in medical imaging domains where dataset characteristics vary widely. Nonetheless, working with IMAGENET1K initialization is most of the time better.

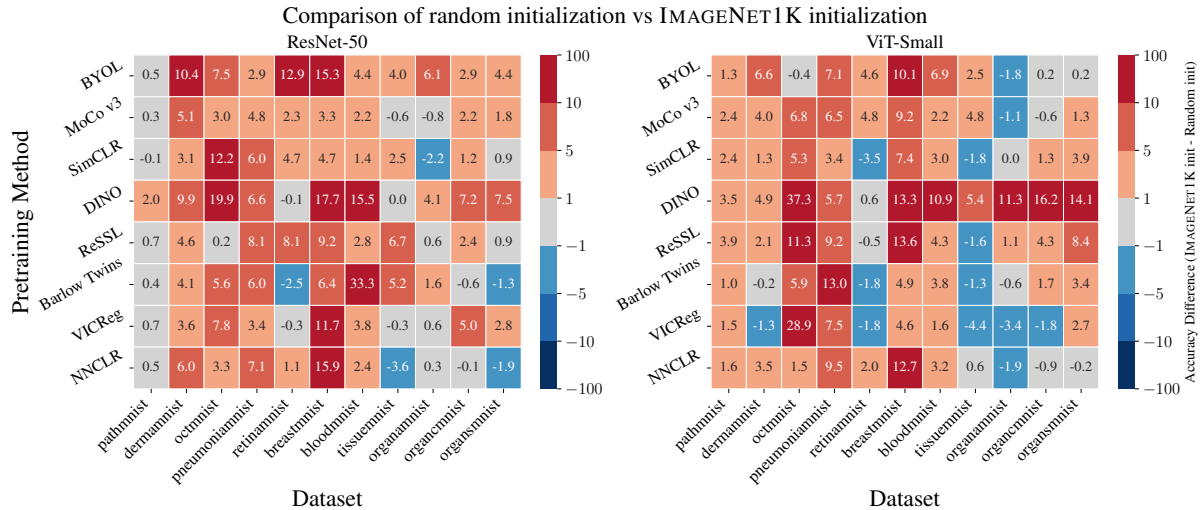


Figure 11. Heatmap showing the accuracy differences for various methods on different datasets using ResNet-50 and ViT-Small backbones. Positive values (shades of red) indicate higher accuracy with IMAGENET1K initialization compared to random, while negative values (shades of blue) show the opposite trend.

Random vs IMAGENET1K Initialization Performance Comparison: We analyze the impact of initialization strategies on self-supervised learning methods across various medical datasets in Table 9. The best scores in random initialization are underlined and the best scores in IMAGENET1K initialization are **bolded**. MoCo v3 emerges as the best method under random initialization, achieving superior performance in 5 out of 11 datasets. The transition to IMAGENET1K initialization shifts the performance landscape; DINO and BYOL show the most substantial improvements. DINO becomes the new leader, achieving the best accuracy in 3 out of 11 datasets. The results show that while IMAGENET1K initialization generally enhances performance, the choice of self-supervised method should be tailored to specific medical imaging tasks, considering both the initialization strategy and the target domain’s characteristics.

Dataset	MoCo v3		SimCLR		DINO		ReSSL		BYOL		VICReg		NNCLR		Barlow Twins	
	Rand.	IN1K	Rand.	IN1K	Rand.	IN1K	Rand.	IN1K	Rand.	IN1K	Rand.	IN1K	Rand.	IN1K	Rand.	IN1K
PathMNIST	92.50	92.84	92.92	92.81	92.03	94.05	91.99	92.69	<u>93.36</u>	93.85	92.32	93.02	92.72	93.18	92.43	92.82
BloodMNIST	95.72	97.90	96.52	97.88	82.85	98.35	95.49	98.28	<u>93.72</u>	98.08	93.25	97.06	95.95	98.30	64.44	97.72
BreastMNIST	<u>85.26</u>	88.59	<u>82.44</u>	87.18	70.38	88.08	72.44	81.67	73.21	88.46	73.46	85.13	73.08	88.97	79.62	86.03
DermaMNIST	<u>73.45</u>	78.50	74.22	77.29	68.78	78.63	<u>74.75</u>	79.32	68.60	78.99	73.06	76.67	72.68	78.70	72.83	76.90
OCTMNIST	<u>79.96</u>	82.94	68.82	80.98	60.70	80.64	<u>78.56</u>	78.74	74.94	82.44	75.20	83.00	79.16	82.48	77.28	82.86
OrganAMNIST	<u>92.63</u>	91.85	89.87	87.69	91.06	95.13	91.89	92.47	86.58	92.70	89.67	90.25	92.56	92.83	91.21	92.80
OrganCMNIST	<u>88.30</u>	90.47	<u>90.22</u>	91.47	84.27	91.51	89.31	91.68	86.51	89.38	84.88	89.90	89.45	89.38	89.29	88.70
OrganSMNIST	<u>77.92</u>	79.69	<u>76.78</u>	77.72	71.01	78.48	77.20	78.12	76.24	80.63	73.86	76.69	76.65	74.73	76.54	75.20
PneumoniaMNIST	<u>87.34</u>	92.18	88.81	94.81	87.24	93.85	87.21	95.29	90.99	93.88	<u>91.03</u>	94.42	88.24	95.35	88.08	94.07
RetinaMNIST	47.75	50.05	46.45	51.15	46.20	46.15	43.15	51.30	41.20	54.10	<u>49.15</u>	48.85	47.40	48.45	<u>52.50</u>	49.95
TissueMNIST	<u>59.68</u>	59.09	58.15	60.65	59.39	59.43	48.45	55.18	55.59	59.58	56.20	55.92	59.39	55.79	<u>53.89</u>	59.09

Table 9. Comparison of mean accuracy scores between random initialization (Rand.) and IMAGENET1K initialization (IN1K) for self-supervised training using ResNet-50 across different methods and datasets.

ResNet-50 vs. ViT-S Performance Comparison: To systematically assess the impact of architectural differences, we compare ResNet-50 and ViT-Small under both random and IMAGENET1K initialization strategies. Table 10 presents the performance differential, computed as the accuracy of ResNet-50 minus that of ViT-Small. For visual clarity, we employ a color-coding scheme where **red** indicates superior ResNet-50 performance and **blue** denotes better ViT-Small performance. Cells are left uncolored when the absolute performance difference is negligible (< 0.01 percentage points). IMAGENET1K initialization generally reduces the performance gap between architectures, suggesting that pre-training helps mitigate architectural biases. Some datasets (e.g., OCT, OrganA) exhibit consistent architectural preferences regardless of initialization, while others (e.g., Blood, Breast) show initialization-dependent trends, where the preferred architecture shifts based on the initialization strategy.

Dataset	MoCo v3		SimCLR		DINO		ReSSL		BYOL		VICReg		NNCLR		Barlow Twins	
	Rand.	IN1K	Rand.	IN1K	Rand.	IN1K	Rand.	IN1K	Rand.	IN1K	Rand.	IN1K	Rand.	IN1K	Rand.	IN1K
PathMNIST	0.79	-1.31	2.40	-0.07	1.40	-0.04	3.33	0.17	2.43	1.66	2.17	1.41	1.56	0.44	1.81	1.19
BloodMNIST	-0.20	-0.26	1.49	-0.14	-4.27	0.32	1.93	0.43	2.18	-0.32	-1.56	0.65	1.02	0.19	-29.24	0.20
BreastMNIST	7.82	1.92	2.69	0.00	-2.69	1.67	0.64	-3.72	0.13	5.26	-9.10	-2.05	-2.44	0.77	2.95	4.49
DermaMNIST	-2.29	-1.21	-3.29	-1.57	-5.15	-0.22	-2.35	0.11	-5.42	-1.60	-3.38	1.54	-2.33	0.22	-4.45	-0.16
OCTMNIST	8.58	4.72	-3.22	3.60	18.76	1.36	15.08	3.96	4.28	12.20	27.96	6.82	4.98	6.76	7.06	6.74
OrganAMNIST	1.80	2.14	-2.74	-4.93	9.69	2.50	2.24	1.70	-3.72	4.23	-1.09	2.85	1.05	3.26	1.96	4.11
OrganCMNIST	-0.61	2.20	1.82	1.74	8.67	-0.34	4.62	2.67	-1.03	1.67	-1.49	5.36	1.44	2.22	2.75	0.50
OrganSMNIST	2.97	3.42	3.29	0.37	7.02	0.40	8.18	0.73	1.98	6.21	2.88	3.00	1.29	-0.40	4.10	-0.66
PneumoniaMNIST	0.00	-1.70	-1.06	1.51	4.52	5.45	4.10	2.98	4.62	0.35	4.36	0.26	3.56	1.19	6.89	-0.13
RetinaMNIST	3.60	1.10	-6.55	1.65	-4.00	-4.65	-7.90	0.75	-5.45	2.80	0.65	2.15	-0.65	36.95	2.45	1.65
TissueMNIST	3.94	-1.48	-5.29	-1.04	0.97	-4.38	-12.53	-4.20	-0.74	0.71	-5.46	-1.32	-0.77	-4.95	-7.59	-1.12

Table 10. Performance difference between ResNet-50 and ViT across different initialization strategies and methods. Red indicates better ResNet-50 performance, and blue indicates better ViT performance.

D.1.2 Linear Evaluation with Limited Labels The in-domain performance results for various label availability scenarios are presented in Tables 11, 12, 13, and 14; corresponding to ResNet-50 and ViT-Small architectures with random or IMAGENET1K initialization. As discussed in Section 4.1, only 1% or 10% of the labels from each dataset were used during downstream training in these scenarios. Notably, all backbones were pre-trained with 100% of their respective datasets. The highest and lowest accuracy values are again highlighted in green and red, respectively.

The aforementioned tables illustrate how label scarcity impacts the performance of different methods. DINO notably shows significant robustness to label scarcity compared to other methods when tested on IMAGENET1K-initialized backbones, prevailing as the best performing method on several datasets in both label scarcity scenarios and with both architectures. For further inspection, DINO’s performance is further evaluated with a fine-tuned backbone as presented in Figure 12. On the other hand, detailed analysis of the effects of label scarcity across different SSL methods, architectures, and initialization strategies is provided in Figure 13. Moreover, Figure 14 presents details on individual methods’ robustness to label scarcity and Figure 15 includes additional analysis of label scarcity on ViT-Small.

Method	PathMNIST		DermaMNIST		OCTMNIST		PneumoniaMNIST		RetinaMNIST	
	10%	1%	10%	1%	10%	1%	10%	1%	10%	1%
SimCLR	92.13 ± 0.51	90.00 ± 0.50	71.71 ± 0.48	69.68 ± 0.82	67.64 ± 0.78	59.58 ± 1.84	91.41 ± 0.57	88.94 ± 3.84	43.35 ± 2.18	41.95 ± 3.36
DINO	91.86 ± 0.05	91.79 ± 0.29	68.05 ± 0.80	66.88 ± 0.65	58.46 ± 0.38	60.14 ± 1.61	91.63 ± 1.04	90.09 ± 0.79	45.70 ± 2.12	42.90 ± 1.67
BYOL	92.28 ± 0.12	92.26 ± 0.08	67.45 ± 0.60	66.92 ± 0.57	77.60 ± 0.72	77.18 ± 1.14	91.79 ± 0.70	90.92 ± 0.62	41.90 ± 2.68	42.05 ± 2.30
ReSSL	91.40 ± 0.22	89.60 ± 0.36	71.19 ± 0.46	69.21 ± 0.59	78.26 ± 1.98	80.72 ± 1.37	90.44 ± 1.26	90.28 ± 1.12	41.20 ± 1.15	42.75 ± 2.08
MoCo v3	92.69 ± 0.10	92.62 ± 0.48	71.58 ± 0.15	70.45 ± 0.52	79.16 ± 0.69	75.76 ± 0.98	91.95 ± 1.49	86.89 ± 2.10	47.95 ± 2.37	43.05 ± 1.69
VICReg	92.85 ± 0.23	92.98 ± 0.13	72.19 ± 0.28	69.73 ± 0.40	73.24 ± 1.32	70.64 ± 1.10	91.05 ± 1.25	86.69 ± 0.98	43.30 ± 0.14	42.75 ± 1.94
Barlow Twins	92.25 ± 0.14	92.24 ± 0.18	72.23 ± 0.43	70.69 ± 0.62	76.66 ± 0.37	69.66 ± 1.12	88.52 ± 1.14	88.36 ± 1.22	51.70 ± 1.54	48.85 ± 4.16
NNCLR	92.57 ± 0.11	92.59 ± 0.22	71.98 ± 0.15	69.98 ± 0.48	77.34 ± 1.22	78.06 ± 0.69	91.12 ± 1.33	89.13 ± 3.06	42.35 ± 3.74	41.10 ± 2.28

Method	BreastMNIST		BloodMNIST		TissueMNIST		OrganAMNIST		OrganCMNIST		OrganSMNIST	
	10%	1%	10%	1%	10%	1%	10%	1%	10%	1%	10%	1%
SimCLR	77.30 ± 1.65	74.61 ± 1.45	95.35 ± 0.23	93.17 ± 0.54	55.94 ± 0.05	51.49 ± 0.13	85.92 ± 1.58	80.47 ± 0.84	85.13 ± 0.53	78.77 ± 0.82	72.45 ± 0.47	62.95 ± 0.74
DINO	71.02 ± 2.06	69.87 ± 2.52	77.43 ± 0.23	70.51 ± 0.68	56.60 ± 0.09	51.94 ± 0.21	87.08 ± 1.39	82.34 ± 0.63	75.49 ± 0.38	60.39 ± 1.88	64.26 ± 0.54	49.48 ± 1.60
BYOL	73.33 ± 0.71	73.07 ± 0.00	90.79 ± 0.09	85.27 ± 0.21	53.26 ± 0.13	48.48 ± 0.55	83.82 ± 0.80	77.16 ± 0.45	79.73 ± 0.48	67.70 ± 0.90	71.51 ± 0.45	59.46 ± 0.46
ReSSL	72.69 ± 1.07	71.66 ± 1.63	93.49 ± 0.31	85.56 ± 0.10	45.49 ± 0.19	42.68 ± 0.09	89.86 ± 0.52	84.52 ± 1.82	83.03 ± 0.51	68.99 ± 0.29	72.31 ± 0.23	57.06 ± 2.18
MoCo v3	79.10 ± 1.21	78.71 ± 1.04	93.69 ± 0.26	89.43 ± 0.33	57.06 ± 0.01	52.50 ± 0.19	89.96 ± 1.43	86.45 ± 0.88	86.08 ± 0.41	73.94 ± 2.81	74.20 ± 0.31	56.26 ± 2.50
VICReg	73.33 ± 1.07	73.59 ± 0.36	90.96 ± 0.21	86.95 ± 0.24	54.18 ± 0.05	49.63 ± 0.14	86.19 ± 0.56	79.90 ± 0.45	82.18 ± 1.26	70.86 ± 0.25	69.20 ± 0.42	52.86 ± 2.28
Barlow Twins	73.46 ± 0.44	73.84 ± 1.73	58.87 ± 0.45	51.44 ± 2.01	50.91 ± 0.09	47.17 ± 0.14	87.38 ± 1.37	83.66 ± 0.70	85.49 ± 0.43	74.07 ± 1.70	70.51 ± 0.33	59.12 ± 0.86
NNCLR	73.97 ± 1.55	74.35 ± 1.78	93.47 ± 0.10	89.79 ± 0.26	56.97 ± 0.08	52.44 ± 0.14	89.66 ± 0.92	87.46 ± 0.38	85.95 ± 1.14	78.08 ± 1.30	73.47 ± 0.48	63.61 ± 0.46

Table 11. In-domain performance of the self-supervised learning methods using ResNet-50 with random initialization with 1% and 10% of the labels.

Method	PathMNIST		DermaMNIST		OCTMNIST		PneumoniaMNIST		RetinaMNIST	
	10%	1%	10%	1%	10%	1%	10%	1%	10%	1%
SimCLR	92.20 ± 0.17	90.88 ± 0.07	73.78 ± 0.98	70.70 ± 0.18	81.66 ± 1.10	80.06 ± 0.14	93.97 ± 1.18	82.24 ± 1.50	47.80 ± 1.02	47.15 ± 2.15
DINO	93.64 ± 0.06	92.17 ± 0.10	75.20 ± 0.36	71.48 ± 0.39	83.10 ± 1.25	80.12 ± 0.85	95.48 ± 0.17	93.84 ± 1.90	47.70 ± 2.29	46.30 ± 4.78
BYOL	93.48 ± 0.23	92.61 ± 0.16	74.04 ± 0.46	71.93 ± 0.51	84.26 ± 0.30	77.90 ± 0.65	95.22 ± 0.55	93.26 ± 1.93	45.70 ± 1.56	42.95 ± 2.12
ReSSL	91.95 ± 0.07	90.61 ± 0.20	74.60 ± 0.50	69.84 ± 0.64	76.40 ± 0.29	63.64 ± 0.14	95.80 ± 0.09	88.14 ± 0.24	48.20 ± 2.54	46.35 ± 2.16
MoCo v3	92.42 ± 0.10	91.53 ± 0.08	74.88 ± 0.34	69.32 ± 0.30	82.96 ± 0.93	82.64 ± 0.27	95.83 ± 0.00	94.35 ± 1.15	44.95 ± 2.67	44.70 ± 1.62
VICReg	92.34 ± 0.09	91.79 ± 0.17	72.99 ± 0.26	68.45 ± 0.32	84.38 ± 0.51	76.14 ± 0.14	94.03 ± 0.41	72.75 ± 1.28	43.75 ± 1.24	42.90 ± 3.05
Barlow Twins	91.92 ± 0.11	91.87 ± 0.15	73.96 ± 0.53	70.70 ± 0.34	83.88 ± 0.86	77.88 ± 0.20	93.71 ± 1.16	85.00 ± 1.47	44.85 ± 0.71	46.10 ± 1.19
NNCLR	91.84 ± 0.05	91.00 ± 0.09	74.41 ± 0.26	71.79 ± 0.92	84.52 ± 0.59	80.86 ± 0.59	94.35 ± 0.26	92.34 ± 1.76	44.70 ± 2.77	47.35 ± 1.72

Method	BreastMNIST		BloodMNIST		TissueMNIST		OrganAMNIST		OrganCMNIST		OrganSMNIST	
	10%	1%	10%	1%	10%	1%	10%	1%	10%	1%	10%	1%
SimCLR	80.51 ± 0.91	73.97 ± 0.44	97.58 ± 0.15	96.03 ± 0.20	57.98 ± 0.07	54.12 ± 0.15	89.78 ± 0.27	84.90 ± 0.72	87.56 ± 0.63	73.27 ± 2.31	73.58 ± 1.29	63.84 ± 0.29
DINO	80.25 ± 2.48	74.35 ± 1.87	97.11 ± 0.29	96.77 ± 0.08	57.91 ± 0.15	54.50 ± 0.07	93.12 ± 0.20	90.30 ± 0.54	89.40 ± 0.42	81.40 ± 0.11	75.55 ± 0.22	63.17 ± 0.49
BYOL	79.23 ± 1.07	76.66 ± 1.83	97.82 ± 0.13	97.47 ± 0.38	56.83 ± 0.12	53.06 ± 0.13	90.76 ± 0.38	86.25 ± 0.45	86.25 ± 0.34	79.51 ± 0.44	76.66 ± 0.50	64.05 ± 0.12
ReSSL	79.74 ± 1.83	79.35 ± 1.53	97.64 ± 0.03	95.28 ± 0.04	52.91 ± 0.07	49.22 ± 0.06	90.59 ± 0.35	85.43 ± 1.56	88.46 ± 0.46	72.34 ± 1.01	76.06 ± 0.60	61.93 ± 1.21
MoCo v3	80.25 ± 1.73	73.84 ± 1.04	97.25 ± 0.18	95.99 ± 0.13	56.27 ± 0.13	52.41 ± 0.23	89.04 ± 0.68	83.87 ± 1.88	89.32 ± 0.90	81.34 ± 0.16	75.96 ± 0.43	65.56 ± 0.85
VICReg	76.92 ± 0.80	74.48 ± 1.31	96.67 ± 0.11	91.73 ± 0.18	53.59 ± 0.15	49.99 ± 0.13	85.12 ± 0.62	84.70 ± 1.08	86.56 ± 0.50	73.22 ± 0.22	72.36 ± 0.27	63.02 ± 0.21
Barlow Twins	77.17 ± 1.74	74.23 ± 1.31	97.08 ± 0.26	96.32 ± 0.09	56.65 ± 0.08	52.72 ± 0.05	88.82 ± 1.38	86.98 ± 0.13	85.55 ± 0.49	74.91 ± 0.79	72.15 ± 0.17	58.25 ± 0.86
NNCLR	82.05 ± 1.69	72.82 ± 2.43	97.64 ± 0.24	96.97 ± 0.36	52.98 ± 0.12	48.03 ± 0.45	89.70 ± 0.37	86.60 ± 2.01	86.85 ± 0.57	76.41 ± 1.67	73.74 ± 0.29	62.08 ± 1.86

Table 12. In-domain performance of the self-supervised learning methods using ResNet-50 with IMAGENET1K initialization with 1% and 10% of the labels.

Method	PathMNIST		DermaMNIST		OCTMNIST		PneumoniaMNIST		RetinaMNIST	
	10%	1%	10%	1%	10%	1%	10%	1%	10%	1%
SimCLR	90.19 ± 0.29	90.42 ± 0.14	74.12 ± 0.80	69.58 ± 0.60	71.58 ± 0.84	66.42 ± 1.03	89.48 ± 0.73	80.03 ± 1.63	43.25 ± 2.19	43.35 ± 2.16
DINO	88.79 ± 0.62	89.40 ± 0.59	70.37 ± 1.45	67.36 ± 0.78	36.64 ± 0.19	35.86 ± 0.24	82.53 ± 1.93	82.50 ± 1.21	47.10 ± 4.46	44.35 ± 2.46
BYOL	89.53 ± 0.16	89.33 ± 0.26	71.45 ± 0.84	69.50 ± 0.26	69.56 ± 0.84	63.14 ± 1.87	89.23 ± 1.17	88.59 ± 0.53	43.40 ± 3.06	44.75 ± 1.32
ReSSL	86.95 ± 1.00	88.43 ± 0.13	73.46 ± 0.27	68.68 ± 0.50	60.88 ± 0.37	52.72 ± 3.07	82.53 ± 0.37	79.39 ± 1.06	45.80 ± 4.08	44.05 ± 2.25
MoCo v3	90.52 ± 0.16	90.21 ± 0.07	71.94 ± 0.36	70.27 ± 0.49	70.48 ± 0.94	63.20 ± 1.76	85.76 ± 3.65	88.01 ± 0.88	44.00 ± 1.39	43.55 ± 0.14
VICReg	89.48 ± 0.24	88.47 ± 0.14	72.69 ± 0.40	69.14 ± 0.44	43.26 ± 0.37	39.58 ± 1.43	89.35 ± 0.36	84.90 ± 1.07	44.15 ± 1.98	42.95 ± 0.80
Barlow Twins	89.11 ± 0.07	88.23 ± 0.31	72.28 ± 0.64	69.66 ± 0.19	69.18 ± 0.90	64.40 ± 1.71	79.77 ± 0.62	81.37 ± 1.44	47.05 ± 2.87	42.30 ± 1.96
NNCLR	89.83 ± 0.20	89.53 ± 0.10	71.74 ± 0.47	69.55 ± 0.33	74.14 ± 0.34	71.72 ± 0.64	84.39 ± 1.72	87.72 ± 0.50	43.50 ± 0.00	43.80 ± 1.41

Method	BreastMNIST		BloodMNIST		TissueMNIST		OrganAMNIST		OrganCMNIST		OrganSMNIST	
	10%	1%	10%	1%	10%	1%	10%	1%	10%	1%	10%	1%
SimCLR	76.15 ± 0.67	76.02 ± 2.55	91.62 ± 0.36	81.91 ± 0.48	61.47 ± 0.03	57.07 ± 0.11	90.11 ± 0.19	83.51 ± 0.27	84.60 ± 0.28	71.45 ± 0.41	70.12 ± 0.36	57.78 ± 0.26
DINO	73.07 ± 0.00	73.07 ± 0.00	81.84 ± 0.43	72.55 ± 1.25	56.17 ± 0.13	53.38 ± 0.56	77.23 ± 0.16	69.64 ± 0.95	67.02 ± 0.50	58.67 ± 0.43	56.93 ± 0.30	43.82 ± 0.54
BYOL	73.07 ± 0.00	73.07 ± 0.00	86.71 ± 0.29	74.11 ± 0.91	53.71 ± 0.30	47.63 ± 0.18	89.11 ± 0.28	83.31 ± 0.53	82.92 ± 1.05	72.45 ± 2.19	69.94 ± 0.18	58.87 ± 0.61
ReSSL	72.82 ± 1.33	70.64 ± 2.72	89.36 ± 0.27	79.63 ± 1.36	59.05 ± 0.04	54.39 ± 0.05	87.57 ± 0.20	81.64 ± 0.26	79.15 ± 0.38	68.46 ± 0.22	63.21 ± 0.91	46.55 ± 0.50
MoCo v3	73.33 ± 1.21	76.53 ± 0.71	92.31 ± 0.24	83.87 ± 0.80	51.15 ± 0.24	45.54 ± 0.18	88.97 ± 0.47	86.19 ± 0.34	85.70 ± 0.47	77.71 ± 0.51	71.13 ± 1.45	56.62 ± 2.02
VICReg	76.28 ± 3.65	78.97 ± 1.42	90.98 ± 0.19	81.17 ± 0.35	59.82 ± 0.08	55.04 ± 0.08	88.98 ± 0.43	82.60 ± 0.25	81.00 ± 0.51	69.64 ± 0.52	66.15 ± 0.34	52.57 ± 0.71
Barlow Twins	74.87 ± 0.36	73.59 ± 1.04	88.43 ± 0.25	77.86 ± 0.38	59.30 ± 0.05	55.33 ± 0.11	87.21 ± 0.28	80.89 ± 0.49	83.39 ± 0.52	70.60 ± 1.08	69.26 ± 0.50	54.55 ± 0.83
NNCLR	71.79 ± 0.00	73.46 ± 1.07	90.99 ± 0.27	82.39 ± 0.61	57.55 ± 0.04	53.40 ± 0.14	90.25 ± 0.40	84.16 ± 0.45	85.24 ± 0.61	74.78 ± 0.16	71.88 ± 0.21	56.40 ± 0.71

Table 13. In-domain performance of the self-supervised learning methods using ViT-Small with random initialization with 1% and 10% of the labels.

Method	PathMNIST		DermaMNIST		OCTMNIST		PneumoniaMNIST		RetinaMNIST	
	10%	1%	10%	1%	10%	1%	10%	1%	10%	1%
SimCLR	92.19 ± 0.25	89.12 ± 0.14	74.10 ± 0.45	69.22 ± 0.85	76.90 ± 0.65	75.34 ± 0.64	94.87 ± 0.34	82.24 ± 1.65	46.80 ± 1.21	45.25 ± 0.49
DINO	92.72 ± 0.19	92.10 ± 0.11	75.07 ± 0.44	70.57 ± 0.45	81.62 ± 0.67	79.78 ± 0.56	93.84 ± 2.13	87.59 ± 2.82	46.85 ± 0.92	43.10 ± 3.56
BYOL	89.99 ± 0.15	88.74 ± 0.21	75.86 ± 0.34	71.02 ± 0.56	69.34 ± 1.04	64.32 ± 1.57	94.90 ± 1.05	84.51 ± 1.32	48.00 ± 1.10	44.00 ± 0.66
ReSSL	92.25 ± 0.03	87.45 ± 0.18	74.98 ± 0.22	69.24 ± 0.58	77.62 ± 0.32	71.70 ± 3.89	94.71 ± 1.93	81.69 ± 2.62	46.55 ± 0.46	44.80 ± 1.83
MoCo v3	92.44 ± 0.26	90.20 ± 0.14	74.49 ± 0.69	69.63 ± 1.20	78.74 ± 1.89	79.04 ± 0.75	93.59 ± 0.77	84.35 ± 0.80	46.40 ± 6.26	43.90 ± 2.11
VICReg	91.34 ± 0.11	90.47 ± 0.28	72.14 ± 0.73	68.40 ± 0.48	75.98 ± 1.01	69.06 ± 1.68	91.60 ± 0.30	75.54 ± 0.61	43.45 ± 1.93	42.95 ± 2.39
Barlow Twins	91.29 ± 0.07	89.34 ± 0.13	72.09 ± 0.78	69.26 ± 1.30	75.00 ± 0.64	72.96 ± 0.76	92.66 ± 1.07	78.81 ± 0.38	45.00 ± 1.77	42.10 ± 3.19
NNCLR	92.38 ± 0.19	90.47 ± 0.34	73.30 ± 0.40	70.31 ± 0.75	75.78 ± 0.58	74.54 ± 0.84	93.62 ± 1.32	84.48 ± 0.97	46.45 ± 2.68	45.95 ± 1.38

Method	BreastMNIST		BloodMNIST		TissueMNIST		OrganAMNIST		OrganCMNIST		OrganSMNIST	
	10%	1%	10%	1%	10%	1%	10%	1%	10%	1%	10%	1%
SimCLR	82.56 ± 2.60	78.33 ± 0.87	97.13 ± 0.18	92.93 ± 0.25	60.38 ± 0.06	55.07 ± 0.07	90.05 ± 0.31	84.48 ± 0.23	86.71 ± 0.46	67.31 ± 1.68	74.27 ± 0.92	56.68 ± 0.61
DINO	77.30 ± 3.50	75.25 ± 0.71	97.84 ± 0.12	95.66 ± 0.35	62.33 ± 0.03	57.67 ± 0.06	92.38 ± 0.36	86.50 ± 0.23	88.37 ± 0.79	77.08 ± 2.49	74.56 ± 0.61	65.72 ± 0.61
BYOL	78.84 ± 4.74	82.17 ± 0.67	97.48 ± 0.12	95.52 ± 0.05	56.84 ± 0.15	51.66 ± 0.05	86.47 ± 1.41	77.61 ± 3.21	85.02 ± 0.40	75.99 ± 2.10	72.24 ± 0.41	64.33 ± 0.45
ReSSL	77.69 ± 2.28	80.12 ± 2.81	96.37 ± 0.20	88.29 ± 0.20	57.43 ± 0.07	52.89 ± 0.09	90.06 ± 0.20	81.34 ± 0.73	85.56 ± 0.28	67.56 ± 0.45	73.75 ± 0.21	54.29 ± 0.95
MoCo v3	80.25 ± 2.48	77.94 ± 3.11	97.53 ± 0.11	93.96 ± 0.24	58.85 ± 0.05	54.48 ± 0.07	85.08 ± 0.75	53.98 ± 7.60	86.23 ± 0.38	76.01 ± 0.72	73.66 ± 0.59	59.44 ± 2.74
VICReg	78.97 ± 1.82	70.51 ± 6.27	95.76 ± 0.33	87.30 ± 0.36	55.60 ± 0.12	50.77 ± 0.11	86.51 ± 0.43	79.25 ± 0.31	83.33 ± 0.36	64.08 ± 0.40	70.82 ± 0.65	54.91 ± 0.32
Barlow Twins	78.20 ± 2.52	72.94 ± 1.31	96.69 ± 0.13	90.73 ± 1.36	58.13 ± 0.09	53.69 ± 0.12	87.09 ± 0.65	84.13 ± 0.44	84.29 ± 0.72	67.73 ± 0.93	72.87 ± 0.40	59.53 ± 1.64
NNCLR	77.82 ± 1.65	81.41 ± 1.26	97.39 ± 0.13	94.56 ± 0.33	58.26 ± 0.12	54.17 ± 0.07	88.14 ± 1.02	83.40 ± 0.60	85.16 ± 0.97	76.96 ± 0.94	73.60 ± 0.53	62.02 ± 0.88

Table 14. In-domain performance of the self-supervised learning methods using ViT-Small with IMAGENET1K initialization with 1% and 10% of the labels.

Comparison of Fine-Tuning Strategies with Limited Labeled Data: Figure 12 presents the experiments using DINO to assess whether fine-tuning the encoder alongside the linear classifier in a low-shot setting improves performance compared to training only the linear classifier. Specifically, we perform two experiments:

- **Frozen Backbone:** We first train a ResNet-50 backbone, initialized with IMAGENET1K weights, on 100% of the training data in a self-supervised manner using DINO. Next, we train a linear classifier on top of the frozen backbone using only 1% of the labeled data.
- **Fine-Tuned Backbone:** Using the same pre-trained ResNet-50 backbone, we fine-tune both the backbone and the linear classifier with 1% of the labeled training data.

Our results align with the findings of Caron et al. [13], demonstrating that the representations learned by DINO are not only robust but often surpass fine-tuned models in terms of accuracy. Interestingly, we observe that fine-tuned models exhibited higher variance across downstream classification tasks. This increased variability is likely attributed to the continuous parameter updates during gradient-based fine-tuning, which can make the model more sensitive to the limited labeled data available in the low-shot setting.

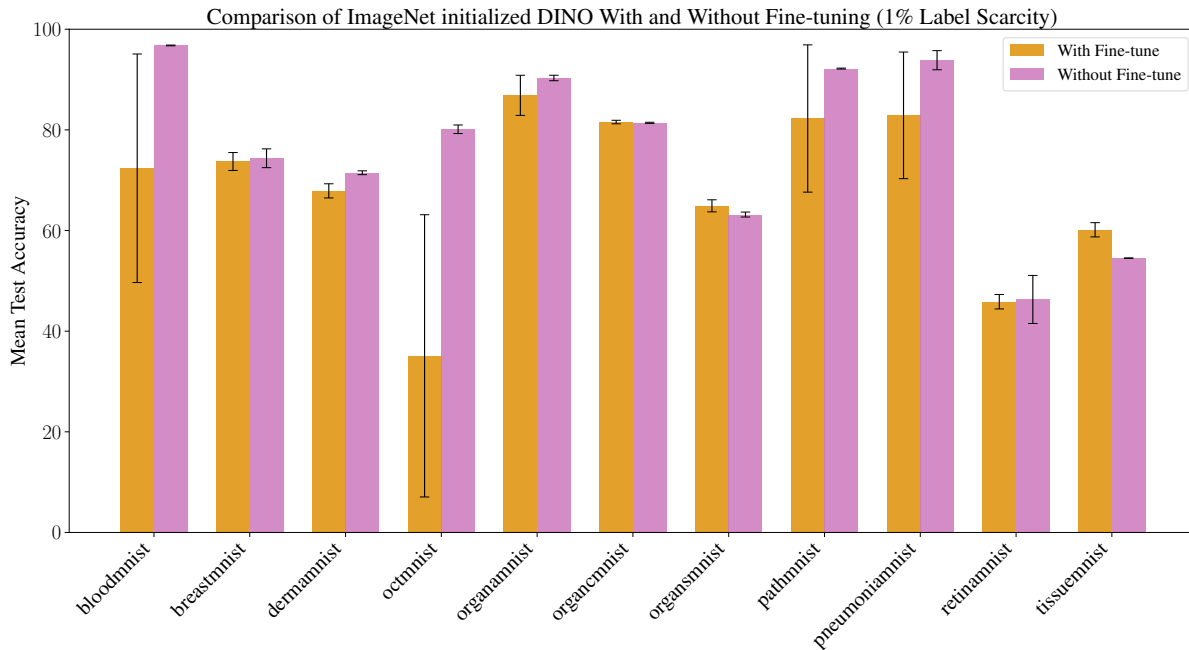


Figure 12. In-domain performance of DINO with ResNet-50 backbone and IMAGENET1K initialization, with and without fine-tuning, across datasets.

Analysis of Performance Drop due to Label Scarcity Across Methods and Initializations: Figure 13 depicts the percentage performance drops of various self-supervised learning methods across different datasets, comparing ResNet-50 and ViT-Small backbones as well as IMAGENET1K and random initialization. Each data point represents the accuracy drop for a specific dataset and method, with larger values indicating greater performance drops. Dashed lines mark the average performance drop for each backbone or initialization setting, summarizing overall trends.

In the top two plots, comparing ResNet-50 with ViT-Small across both IMAGENET1K and random initializations, ResNet-50 consistently exhibits lower average performance drops than ViT-Small across methods and datasets. This suggests that ResNet-50 offers more stable accuracy across a range of medical imaging tasks under these conditions.

Conversely, the bottom two plots comparing IMAGENET1K with random initialization for different backbones show less consistency, with average performance drop lines frequently crossing. This indicates no definitive advantage of one initialization strategy over the other across all datasets and methods, suggesting that the impact of initialization is more context-dependent, varying significantly with the specific dataset or backbone used.

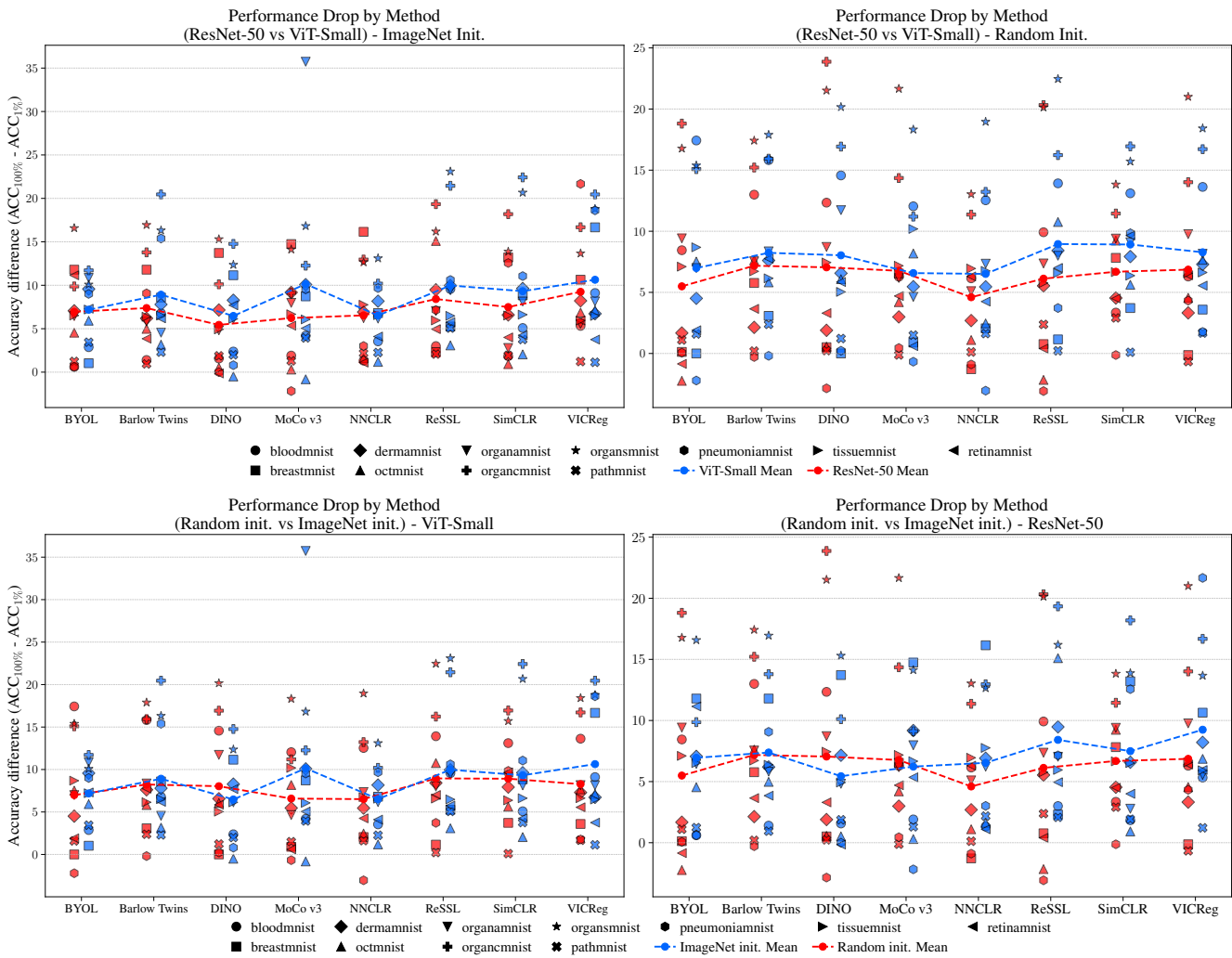


Figure 13. Scatter plots showing the performance drop (%) for different SSL methods across various datasets. The top row compares ResNet-50 and ViT-Small backbones, while the bottom row contrasts IMAGENET1K and random initialization strategies. Each data point represents the performance drop of a specific method on a particular dataset, with dashed lines indicating the average performance drop for each comparison.

Performance Comparison of SSL Methods Under Label Scarcity: Figure 14 shows the mean test accuracy across all datasets using various self-supervised learning methods at different levels of label availability (1%, 10%, and 100%). This visualization highlights how accuracy scales with the availability of labeled data for each method, encompassing all combinations of backbones (ResNet-50 and ViT) and initialization types (Random Initialization and IMAGENET1K Initialization).

The results show that at 1% label availability, there is significantly higher variance in test accuracy compared to 10% and 100%, indicating greater instability with limited labels. As label availability increases, the mean accuracy naturally improves, demonstrating enhanced performance with more labeled data. Furthermore, the increase in mean accuracy from 10% to 100% label availability seems to be smaller than the increase from 1% to 10%, suggesting that additional label access yields diminishing returns in accuracy gains.

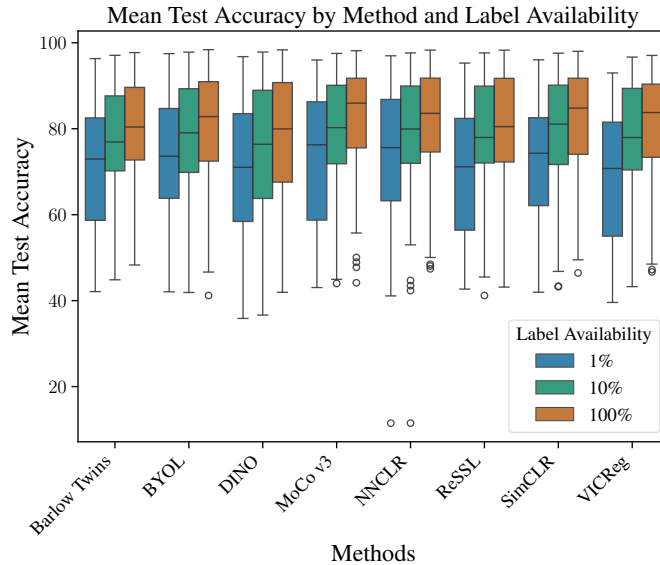


Figure 14. Mean test accuracy across different self-supervised learning methods at varying levels of label availability (1%, 10%, and 100%). The plot illustrates how accuracy scales with label availability for each method. All combinations of backbones (ResNet50, ViT) and initialization types (Random Initialization, IMAGENET1K Initialization) were used to calculate the means.

D.2 Out-of-distribution Detection

D.2.1 Effect of SSL Method Tables 15, 16, 17 and 18 show performance metrics (AUROC and AUPR) for OOD detection across 8 self-supervised learning models on diverse medical imaging datasets. Each cell shows the average scores across all $(\mathcal{P}_{ID}, \mathcal{P}_{OOD})$ pairs when the dataset mentioned in that row is considered \mathcal{P}_{ID} and used for pre-training. Each model’s performance is evaluated in terms of AUROC (higher values indicate better separability) and AUPR (higher values indicate better precision-recall performance) with the best results highlighted in green and the worst in red for AUROC. Similarly, for AUPR, the best results are highlighted in light green and the worst in light red.

For ResNet-50 architectures, we observe from Tables 15 and 16 that NNCLR consistently outperforms other models, achieving the highest average AUROC and AUPR across datasets. MoCo v3 demonstrates stable performance under both random and IMAGENET1K initialization strategies, highlighting its robustness. In contrast, BYOL exhibits excellent performance under IMAGENET1K initialization but performs poorly when initialized with random weights, indicating sensitivity to initialization strategies. SimCLR, on the other hand, achieves the lowest OOD detection scores when models are initialized with IMAGENET1K weights, reflecting its relative inefficiency in such scenarios.

For ViT-Small architectures, Tables 17 and 18 reveal that MoCo v3 delivers the best performance across both random and IMAGENET1K initialization strategies, establishing itself as the most robust approach for OOD detection in this setting. DINO achieves strong results under IMAGENET1K initialization but experiences a significant decline in performance when initialized with random weights, indicating a reliance on pretrained feature representations. In contrast, VICReg shows the largest drop in average AUROC and AUPR when switching from random initialization to IMAGENET1K initialization, suggesting a potential mismatch between its pretrained features and OOD detection requirements.

Figures 16, 18, and 17 present the density distributions of AUROC scores for various SSL methods across different

Comparison of IMAGENET1K vs Random Initialization using ViT-Small in Low-Label Setting: Figure 15 illustrates the mean test accuracy of ViT-Small across datasets under 1%, 10%, and 100% label availability, comparing models initialized with IMAGENET1K weights to those with random initialization (hatched bars).

As is evident from the plot, models initialized with IMAGENET1K weights consistently outperform those with random initialization, particularly in label-scarce scenarios. Notably, DINO exhibits significant performance gains at 1% label availability, transitioning from the worst-performing method under random initialization to the best-performing one when initialized with IMAGENET1K weights. Furthermore, the increase across all methods in mean test accuracy from 10% to 100% label availability seems smaller than the increase from 1% to 10%, suggesting that additional label access yields diminishing returns in accuracy gains.

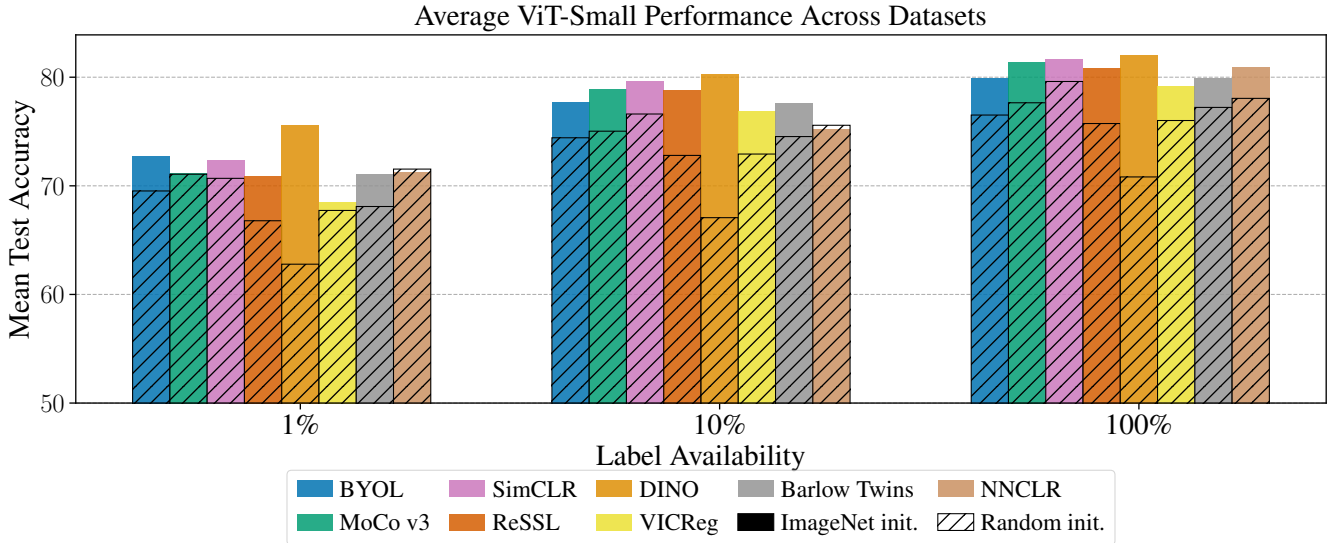


Figure 15. Mean test accuracy across all datasets with 1%, 10%, and 100% label availability, comparing IMAGENET1K against random initialization (hatched) using ViT-Small for different methods.

Dataset	MoCo v3		SimCLR		DINO		ReSSL		BYOL		VICReg		NNCLR		Barlow Twins	
	AUROC	AUPR	AUROC	AUPR	AUROC	AUPR	AUROC	AUPR	AUROC	AUPR	AUROC	AUPR	AUROC	AUPR	AUROC	AUPR
PathMNIST	0.982	0.952	0.872	0.774	0.974	0.956	0.936	0.904	0.982	0.964	0.986	0.968	0.973	0.945	0.990	0.973
DermaMNIST	0.988	0.949	0.994	0.978	0.925	0.556	0.978	0.909	0.516	0.173	0.984	0.927	0.965	0.900	0.987	0.965
OCTMNIST	0.904	0.674	0.888	0.644	0.998	0.994	0.952	0.819	0.983	0.962	0.989	0.934	0.975	0.907	0.955	0.874
PneumoniaMNIST	0.998	0.994	0.998	0.995	0.924	0.311	0.990	0.964	0.808	0.189	0.997	0.980	0.998	0.996	0.988	0.925
BreastMNIST	0.568	0.019	0.751	0.028	0.943	0.714	0.525	0.020	0.911	0.596	0.498	0.033	0.840	0.122	0.843	0.068
BloodMNIST	0.997	0.986	0.984	0.930	0.997	0.991	0.991	0.977	0.985	0.965	0.994	0.977	0.997	0.989	0.954	0.908
TissueMNIST	0.995	0.996	0.995	0.997	0.998	0.999	0.998	0.999	0.999	0.999	0.998	0.999	0.990	0.994	0.999	0.999
OrganAMNIST	0.864	0.823	0.740	0.649	0.823	0.804	0.725	0.711	0.672	0.702	0.772	0.722	0.894	0.874	0.851	0.816
OrganCMNIST	0.878	0.791	0.871	0.782	0.720	0.627	0.906	0.821	0.780	0.701	0.831	0.724	0.866	0.776	0.823	0.717
OrganSMNIST	0.894	0.789	0.852	0.760	0.703	0.605	0.894	0.800	0.786	0.709	0.813	0.733	0.881	0.795	0.741	0.649
Average	0.907	0.797	0.894	0.754	0.901	0.756	0.889	0.792	0.842	0.696	0.886	0.800	0.938	0.830	0.913	0.789

Table 15. Average OOD detection performance of ResNet-50 models initialized with random weights for different datasets

model backbones and initialization schemes. These visualizations provide insights into the performance of each method in OOD detection under distinct configurations. Notably, MoCo v3 consistently achieves the highest AUROC scores with ViT-Small backbones, both when randomly initialized and when initialized with IMAGENET1K weights. In contrast, NNCLR demonstrates superior OOD detection performance when paired with a ResNet-50 backbone. Figure 16 suggests that for SimCLR models, IMAGENET1K initialization with a ResNet-50 backbone results in a distinctively low AUROC score for OOD detection. This variability in performance highlights the impact of both the SSL method and the model architecture on OOD detection capabilities, emphasizing the importance of selecting the right combination for optimal results.

D.2.2 Effect of Backbone Architecture The choice of backbone architecture is crucial for OOD detection performance. Figure 19 demonstrates how the choice of backbone affects the distribution of OOD AUROC scores for each method, strongly

Dataset	MoCo v3		SimCLR		DINO		ReSSL		BYOL		VICReg		NNCLR		Barlow Twins	
	AUROC	AUPR	AUROC	AUPR	AUROC	AUPR	AUROC	AUPR	AUROC	AUPR	AUROC	AUPR	AUROC	AUPR	AUROC	AUPR
PathMNIST	0.974	0.955	0.765	0.627	0.979	0.963	0.944	0.906	0.982	0.966	0.878	0.805	0.979	0.955	0.914	0.858
DermaMNIST	0.959	0.850	0.795	0.522	0.981	0.944	0.976	0.935	0.994	0.972	0.835	0.509	0.993	0.959	0.959	0.833
OCTMNIST	0.920	0.667	0.819	0.503	0.998	0.991	0.751	0.257	0.994	0.967	0.915	0.648	0.969	0.878	0.954	0.805
PneumoniaMNIST	0.971	0.916	0.580	0.189	0.986	0.958	0.987	0.958	0.970	0.941	0.886	0.418	0.992	0.964	0.971	0.931
BreastMNIST	0.996	0.928	0.998	0.941	0.964	0.451	0.715	0.043	0.997	0.912	0.983	0.697	0.998	0.943	0.993	0.876
BloodMNIST	0.992	0.968	0.908	0.727	0.986	0.956	0.999	0.997	0.991	0.952	0.941	0.829	0.996	0.986	0.979	0.919
TissueMNIST	0.995	0.997	0.994	0.996	0.650	0.695	0.994	0.995	0.999	0.999	0.983	0.994	0.999	0.999	0.993	0.997
OrganAMNIST	0.830	0.754	0.524	0.526	0.812	0.734	0.613	0.614	0.822	0.760	0.867	0.827	0.899	0.829	0.875	0.826
OrganCMNIST	0.770	0.663	0.604	0.480	0.725	0.575	0.623	0.508	0.859	0.753	0.809	0.694	0.848	0.742	0.879	0.772
OrganSMNIST	0.755	0.619	0.632	0.497	0.620	0.520	0.627	0.514	0.757	0.637	0.744	0.577	0.821	0.705	0.857	0.748
Average	0.916	0.832	0.762	0.601	0.870	0.779	0.823	0.673	0.937	0.886	0.884	0.700	0.949	0.896	0.937	0.856

Table 16. Average OOD detection performance of ResNet-50 models initialized with IMAGENET1K weights evaluated across different datasets.

Dataset	MoCo v3		SimCLR		DINO		ReSSL		BYOL		VICReg		NNCLR		Barlow Twins	
	AUROC	AUPR	AUROC	AUPR	AUROC	AUPR	AUROC	AUPR	AUROC	AUPR	AUROC	AUPR	AUROC	AUPR	AUROC	AUPR
PathMNIST	0.999	0.999	0.997	0.997	0.996	0.996	0.996	0.995	0.995	0.989	0.997	0.996	0.999	0.999	0.993	0.991
DermaMNIST	0.998	0.995	0.997	0.991	0.996	0.986	0.997	0.986	0.997	0.991	0.986	0.938	0.996	0.988	0.995	0.986
OCTMNIST	0.992	0.969	0.996	0.974	0.971	0.890	0.994	0.960	0.980	0.928	0.965	0.801	0.975	0.920	0.760	0.309
PneumoniaMNIST	0.999	0.984	0.998	0.986	0.988	0.912	0.992	0.894	0.990	0.937	0.985	0.835	0.999	0.990	0.989	0.877
BreastMNIST	0.987	0.811	0.955	0.768	0.690	0.184	0.869	0.571	0.749	0.258	0.970	0.796	0.965	0.751	0.995	0.851
BloodMNIST	0.999	0.999	0.999	0.999	0.999	0.999	0.999	0.999	0.999	0.999	0.999	0.996	0.999	0.999	0.999	0.999
TissueMNIST	0.999	0.999	0.999	0.999	0.999	0.999	0.998	0.998	0.998	0.999	0.998	0.999	0.999	0.999	0.998	0.999
OrganAMNIST	0.924	0.911	0.929	0.899	0.889	0.843	0.888	0.865	0.928	0.911	0.923	0.904	0.924	0.897	0.911	0.880
OrganCMNIST	0.870	0.762	0.869	0.773	0.796	0.682	0.821	0.677	0.850	0.753	0.820	0.668	0.850	0.754	0.868	0.753
OrganSMNIST	0.825	0.728	0.845	0.757	0.808	0.712	0.829	0.713	0.860	0.773	0.727	0.578	0.842	0.743	0.842	0.729
Average	0.959	0.916	0.959	0.914	0.913	0.820	0.938	0.866	0.935	0.854	0.937	0.851	0.955	0.904	0.935	0.837

Table 17. Average OOD detection performance of ViT-Small models initialized with random weights evaluated across different datasets

Dataset	MoCo v3		SimCLR		DINO		ReSSL		BYOL		VICReg		NNCLR		Barlow Twins	
	AUROC	AUPR	AUROC	AUPR	AUROC	AUPR	AUROC	AUPR	AUROC	AUPR	AUROC	AUPR	AUROC	AUPR	AUROC	AUPR
PathMNIST	0.987	0.965	0.974	0.956	0.996	0.994	0.975	0.959	0.807	0.722	0.949	0.901	0.987	0.972	0.967	0.934
DermaMNIST	0.993	0.966	0.994	0.972	0.995	0.971	0.997	0.983	0.996	0.988	0.859	0.563	0.994	0.964	0.965	0.815
OCTMNIST	0.976	0.852	0.977	0.892	0.999	0.998	0.981	0.863	0.852	0.743	0.810	0.292	0.898	0.645	0.932	0.664
PneumoniaMNIST	0.999	0.998	0.998	0.996	0.984	0.946	0.998	0.981	0.997	0.983	0.901	0.464	0.999	0.998	0.993	0.942
BreastMNIST	0.999	0.981	0.964	0.629	0.992	0.908	0.995	0.931	0.996	0.941	0.948	0.587	0.999	0.946	0.955	0.687
BloodMNIST	0.998	0.984	0.998	0.990	0.999	0.997	0.999	0.998	0.996	0.993	0.960	0.831	0.997	0.983	0.952	0.806
TissueMNIST	0.998	0.999	0.999	0.999	0.999	0.999	0.984	0.993	0.957	0.980	0.809	0.856	0.999	0.999	0.934	0.968
OrganAMNIST	0.931	0.915	0.793	0.756	0.907	0.903	0.782	0.750	0.902	0.872	0.808	0.743	0.849	0.824	0.802	0.781
OrganCMNIST	0.836	0.702	0.837	0.738	0.819	0.759	0.771	0.687	0.824	0.671	0.827	0.660	0.805	0.679	0.874	0.727
OrganSMNIST	0.843	0.738	0.774	0.644	0.802	0.727	0.800	0.715	0.724	0.600	0.816	0.638	0.811	0.704	0.850	0.713
Average	0.956	0.910	0.931	0.857	0.949	0.920	0.928	0.886	0.905	0.849	0.869	0.654	0.934	0.872	0.922	0.804

Table 18. Average OOD detection performance of ViT-Small models initialized with IMAGENET1K weights evaluated across different datasets.

suggesting that ViT-Small is the superior option among all SSL methods in general. A comparison between Figures 5 and 17 for random initialization setting reveals that ViT-Small architectures exhibit a lower variance and a higher density of AUROC scores in the upper range, indicating their effectiveness in OOD detection. Specifically, as depicted in Figure 17, ViT-Small models, particularly those employing MoCo v3 and SimCLR, show pronounced peak densities near AUROC scores of 0.96. This is significantly higher compared to the ResNet-50 models shown in Figure 5, where the AUROC scores are more broadly distributed with a maximum around 0.93. Furthermore, this observation holds true for the IMAGENET1K initialization setting as well. Figures 16 and 18 demonstrate that the ViT-Small architecture consistently exhibits a higher density of large AUROC scores compared to the ResNet-50 architecture.

To investigate the impact of backbone architecture in more detail, we analyze the effect of backbone among different $(\mathcal{P}_{ID}, \mathcal{P}_{OOD})$ pairs in Figures 20 and 21. For random initialization, we observe an improvement in OOD scores when ViT-Small is used across many of the $(\mathcal{P}_{ID}, \mathcal{P}_{OOD})$ pairs. In contrast, Figures 22 and 23 reveal a shift in backbone preferences when models are initialized with IMAGENET1K weights. Notably, SimCLR, DINO, ReSSL, and MoCo v3 tend to favor ViT-Small for the majority of $(\mathcal{P}_{ID}, \mathcal{P}_{OOD})$ pairs, whereas BYOL, NNCLR, and VICReg demonstrate a preference for ResNet-50. For Barlow Twins, there is no clear preference for either backbone.

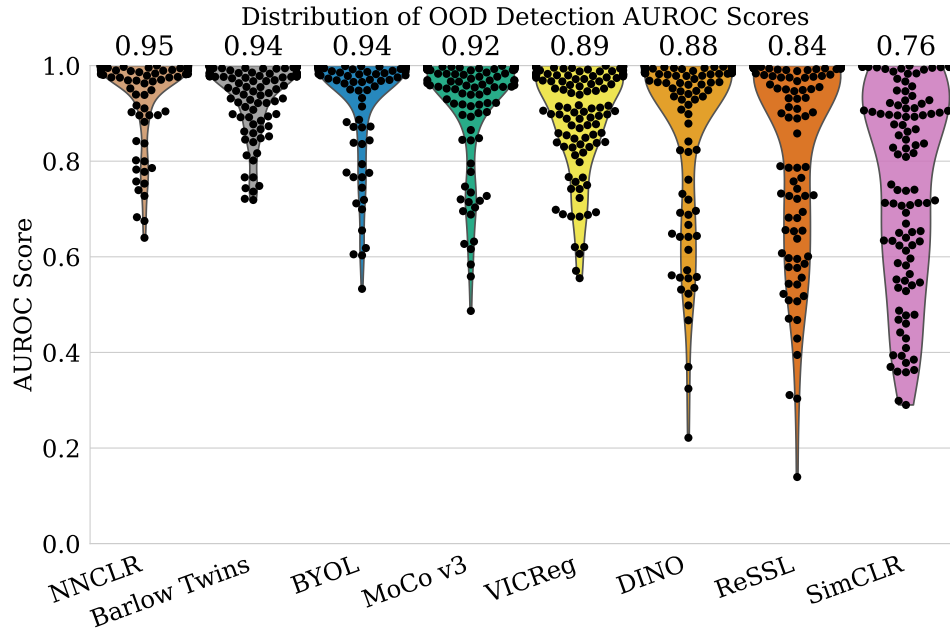


Figure 16. AUROC score distributions for various SSL methods on IMAGENET1K initialized ResNet-50 backbone in OOD detection.

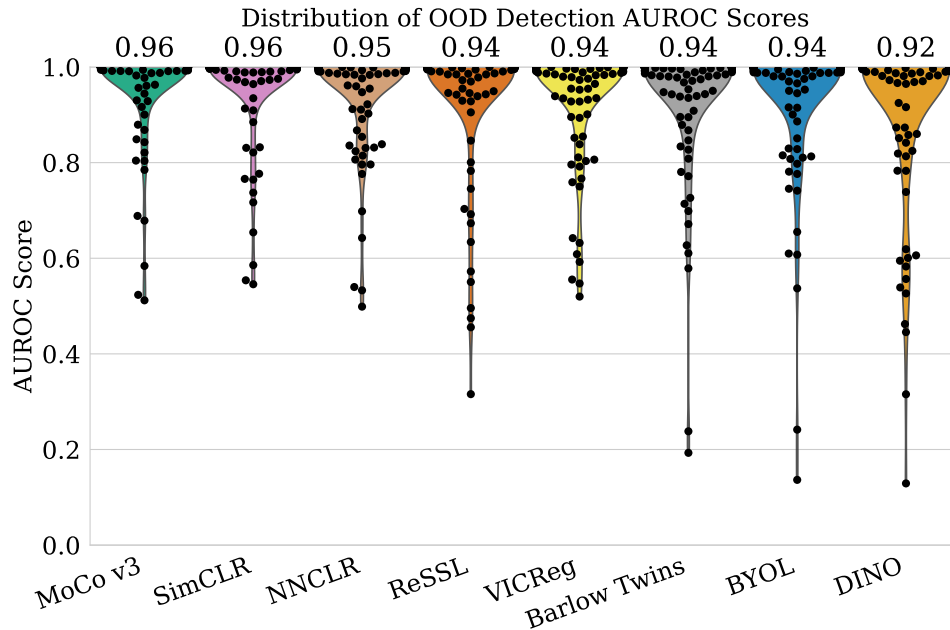


Figure 17. AUROC score distributions for various SSL methods on random initialized ViT-Small backbone in OOD detection.

D.2.3 Effect of Initialization For the OOD detection task, we compare the importance of IMAGENET1K-supervised weight initialization with that of random initialization. Figures 24 and 25 illustrate the effect of initialization across ResNet-50 based models and $(\mathcal{P}_{ID}, \mathcal{P}_{OOD})$ pairs. It is evident that the effect of initialization depends on both the choice of SSL model and the specific $(\mathcal{P}_{ID}, \mathcal{P}_{OOD})$ pair. For many datasets, methods such as SimCLR, ReSSL, MoCo v3, and VICReg tend to prefer random initialization over IMAGENET1K initialization, whereas BYOL and DINO favor IMAGENET1K initialization. Additionally, models trained on smaller datasets like BreastMNIST and RetinaMNIST specifically benefit from IMAGENET1K initialization across all SSL methods for OOD detection. This observation indicates that, for the ResNet-50

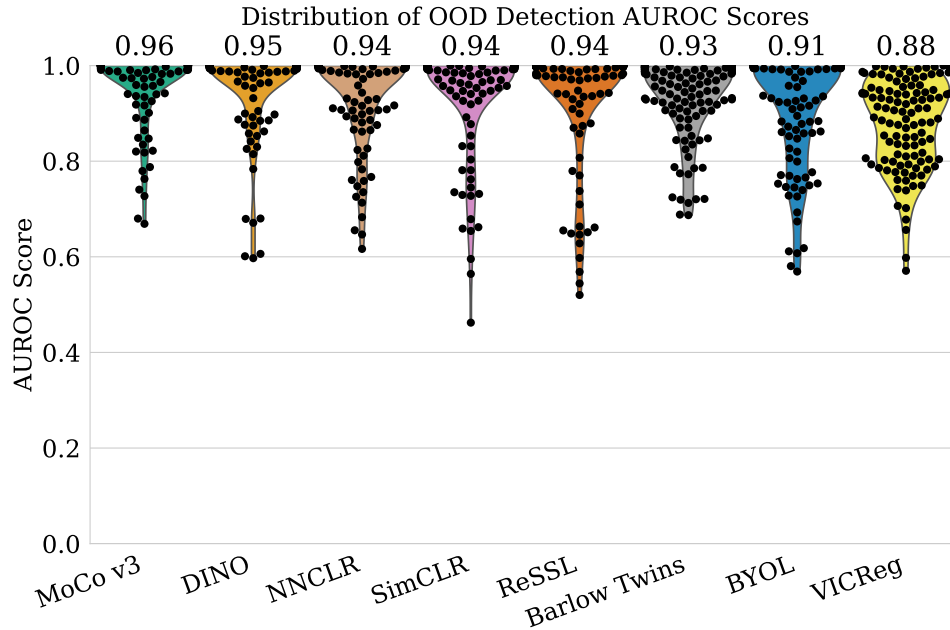


Figure 18. AUROC score distributions for various SSL methods on IMAGENET1K initialized ViT-Small backbones in OOD detection.

backbone, smaller datasets gain significant advantages from supervised IMAGENET1K weights.

Next, we investigate whether this observation also holds for the ViT-Small backbone. Figures 26 and 27 illustrate the effect of initialization for ViT-Small architectures. Compared to ResNet-50, it can be observed that the effect of initialization is diminished, as the differences between AUROC scores are closer to zero for many $(\mathcal{P}_{ID}, \mathcal{P}_{OOD})$ pairs. Despite this, several models still favor random initialization over IMAGENET1K initialization for when trained with datasets such as OCTMNIST, OrganAMNIST, OrganCMNIST, and OrganSMNIST. BYOL, DINO, and ReSSL methods trained with BreastMNIST prefers IMAGENET1K initialization for better OOD detection. However, unlike the ResNet-50 backbone, this preference does not extend consistently across other SSL methods. These findings suggest that while ViT-Small may be less sensitive to initialization strategies overall, certain models and datasets still benefit from appropriate weight initialization.

D.2.4 Effect of Multi-domain Datasets Figure 28 compares the OOD AUROC scores of models trained on single-domain datasets versus multi-domain datasets. On average, multi-domain datasets containing more diverse samples, such as Organ{A,S}PnePath, outperform less diverse datasets like Organ{A,C,S} across all $(\mathcal{P}_{ID}, \mathcal{P}_{OOD})$ pairs.

The left panel of Figure 28 highlights that models trained on single-domain datasets generally achieve higher AUROC scores compared to those trained on the Organ{A,C,S} dataset. Conversely, the right panel shows that models trained on Organ{A,S}PnePath consistently achieve higher AUROC scores compared to single-domain trained models, leading to superior overall OOD detection performance.

These results emphasize the critical role of dataset diversity in improving OOD detection performance. Incorporating more diverse samples during training significantly enhances a model’s ability to generalize and detect OOD examples effectively. This underscores the importance of dataset design and diversity in the development of robust OOD detection systems.

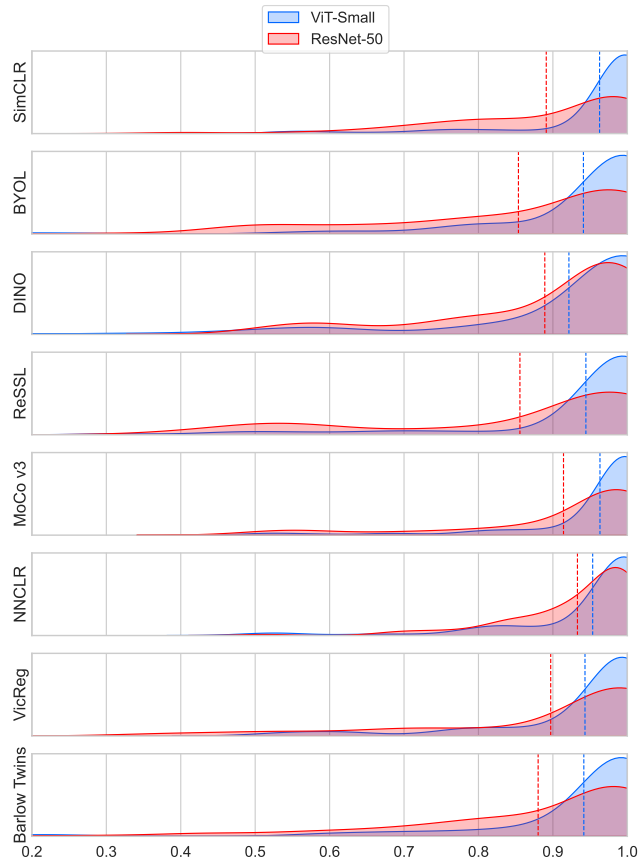


Figure 19. Distribution of AUROC scores for different SSL methods.

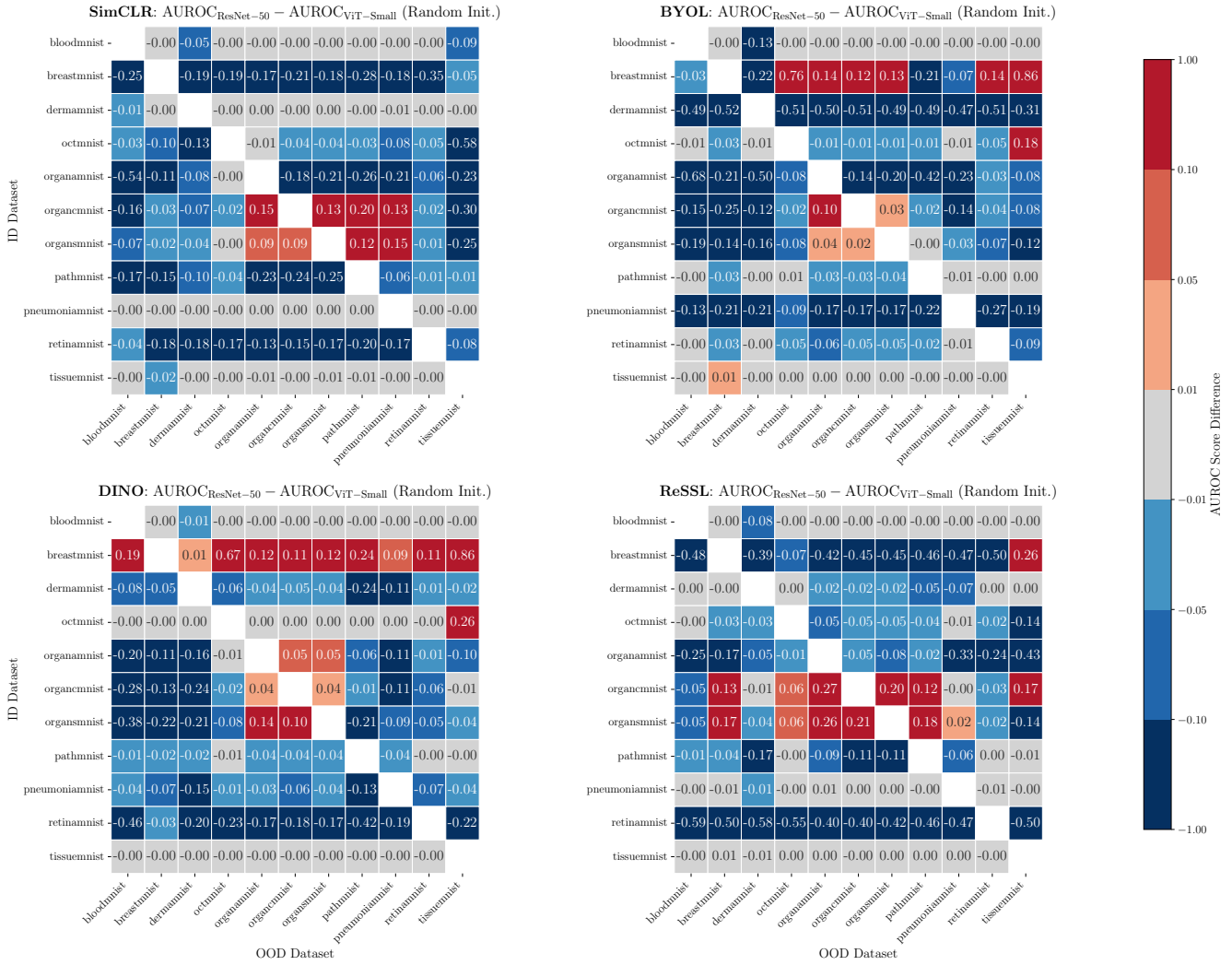


Figure 20. Effect of backbone choice (ResNet vs. ViT) on AUROC scores for OOD detection across various dataset combinations and SSL methods with random initialization. Negative values (blue) indicate better OOD detection performance with the ViT backbone, while positive values (red) favor ResNet-50.

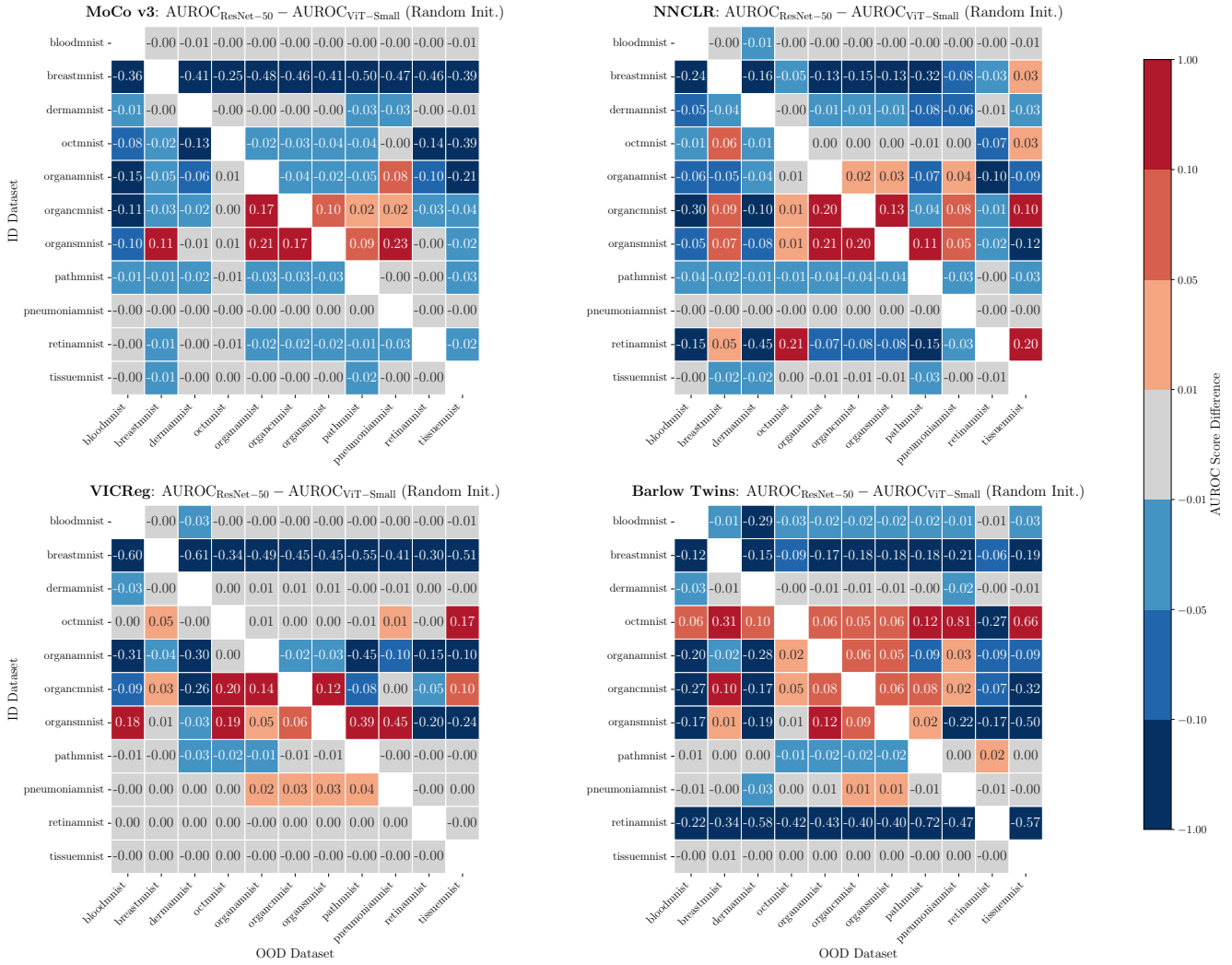


Figure 21. Effect of backbone choice (ResNet vs. ViT) on AUROC scores for OOD detection across various dataset combinations and SSL methods with random initialization. Negative values (blue) indicate better OOD detection performance with the ViT backbone, while positive values (red) favor ResNet-50.

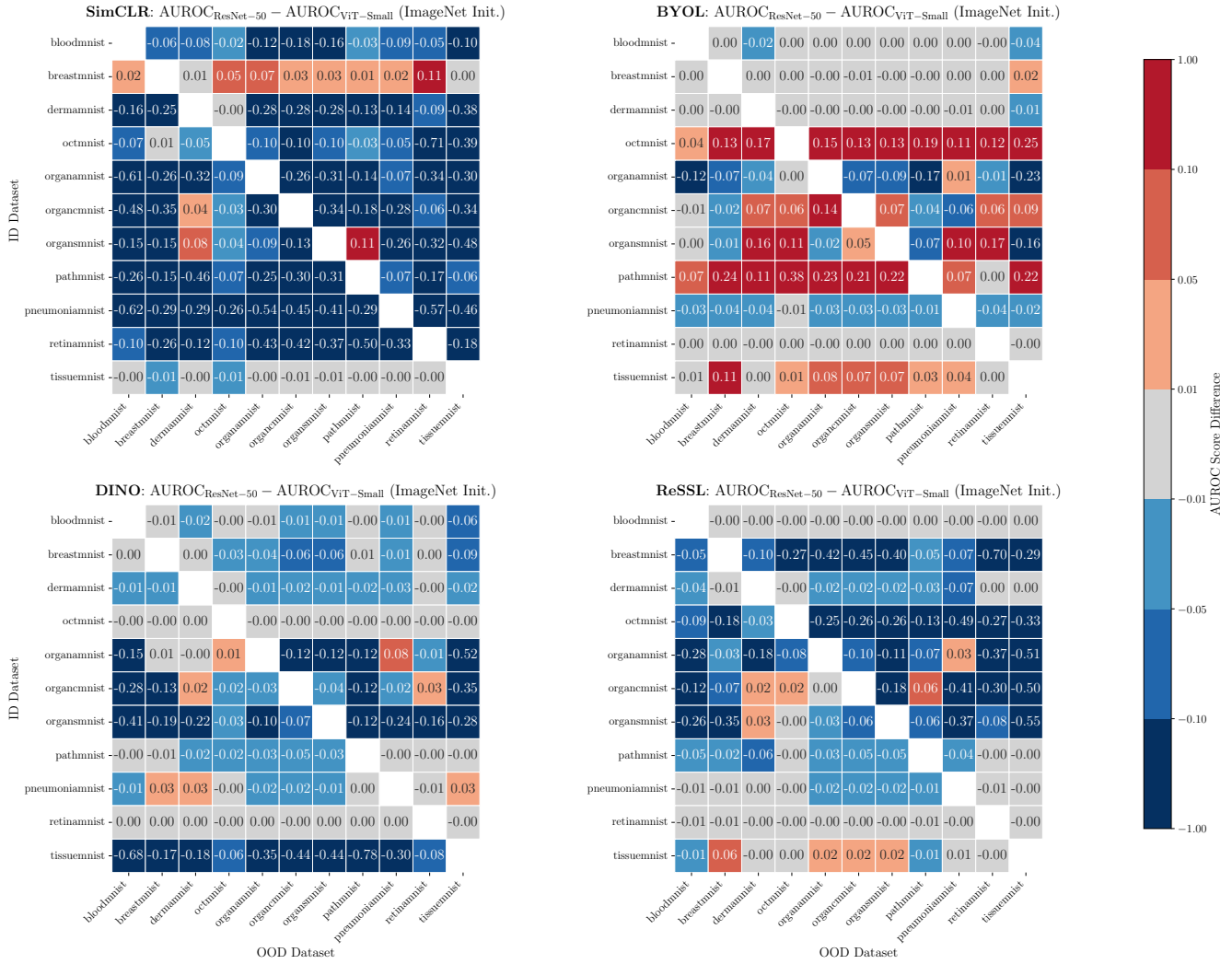


Figure 22. Effect of backbone choice (ResNet vs. ViT) on AUROC scores for OOD detection across various dataset combinations and SSL methods with IMAGENET1K initialization. Negative values (blue) indicate better OOD detection performance with the ViT backbone, while positive values (red) favor ResNet-50.

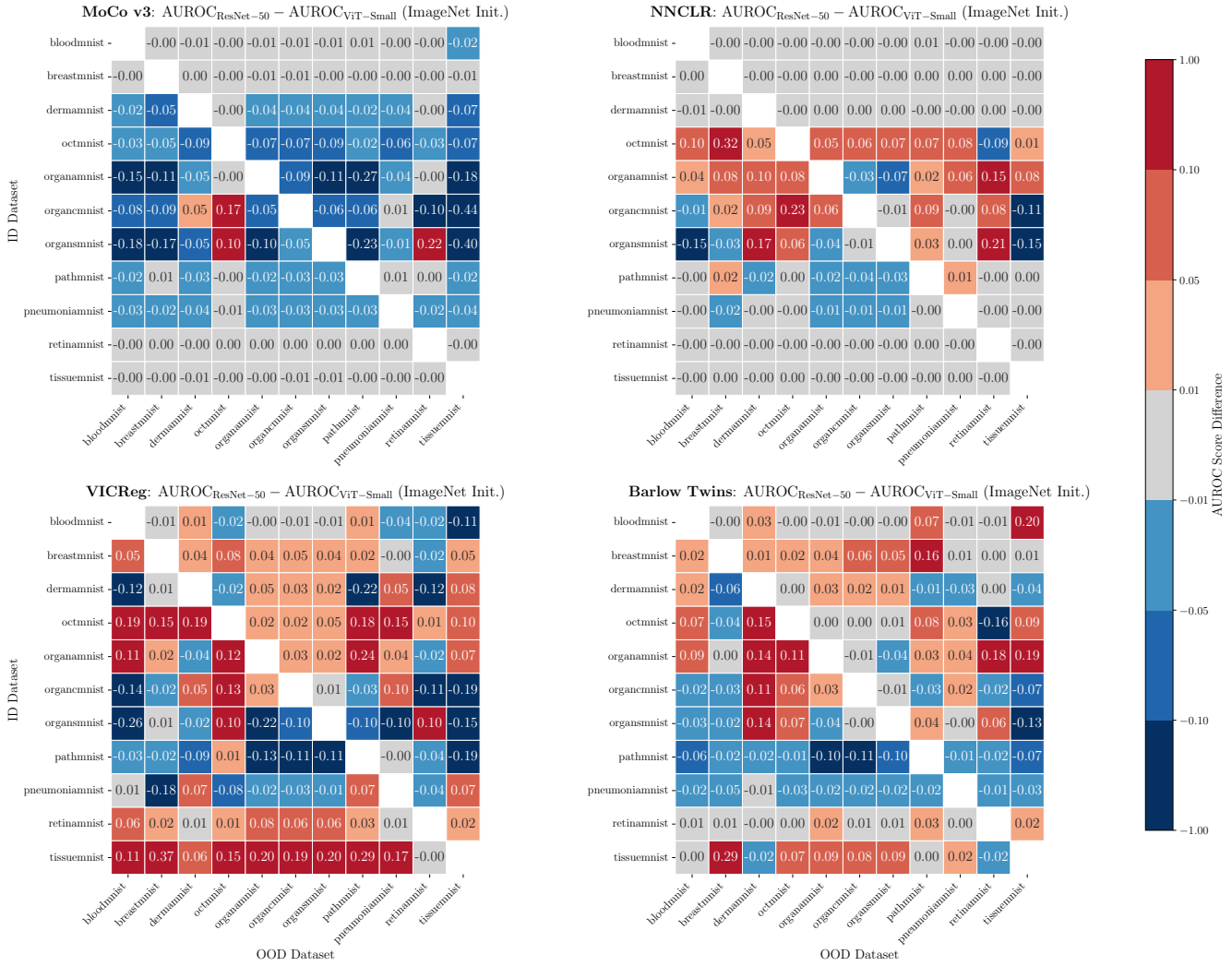


Figure 23. Effect of backbone choice (ResNet vs. ViT) on AUROC scores for OOD detection across various dataset combinations and SSL methods with IMAGENET1K initialization. Negative values (blue) indicate better OOD detection performance with the ViT backbone, while positive values (red) favor ResNet-50.

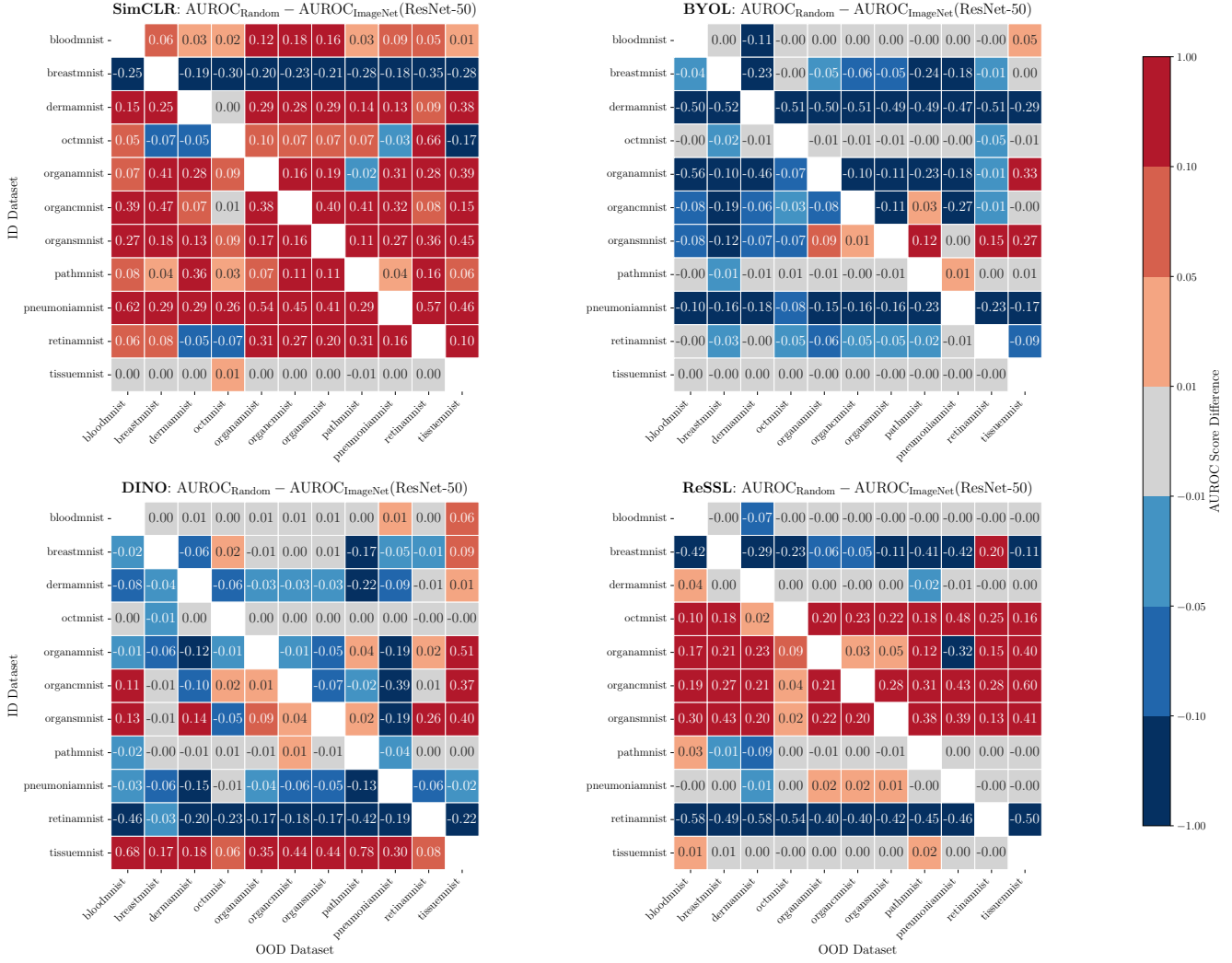


Figure 24. Effect of Initialization (Random vs. IMAGENET1K) on AUROC scores for OOD detection across various dataset combinations and SSL methods with ResNet-50 backbone. Positive values (blue) indicate better OOD detection performance with the random initialization, while negative values (red) favor IMAGENET1K initialization.

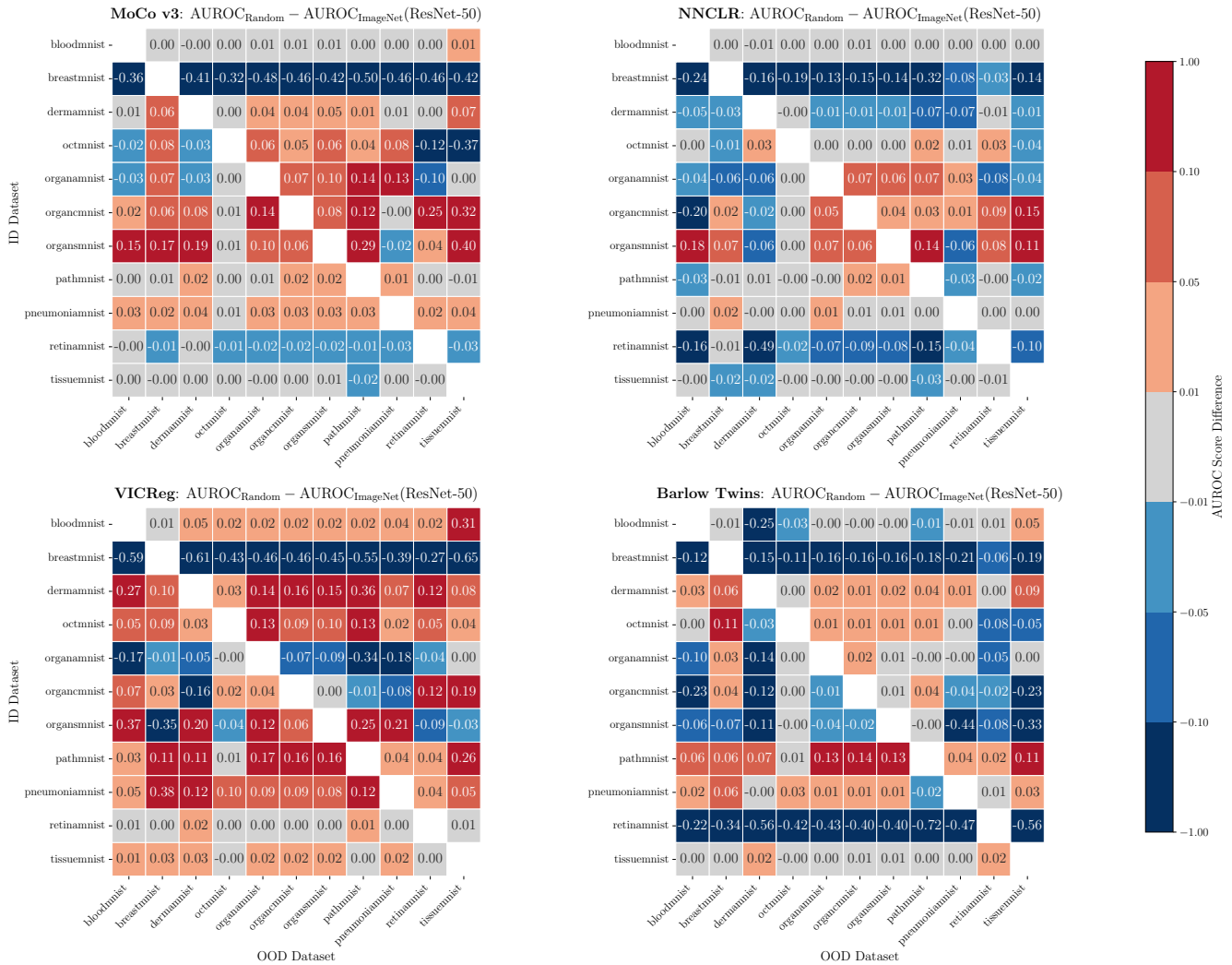


Figure 25. Effect of Initialization (Random vs. IMAGENET1K) on AUROC scores for OOD detection across various dataset combinations and SSL methods with ResNet-50 backbone. Positive values (blue) indicate better OOD detection performance with the random initialization, while negative values (red) favor IMAGENET1K initialization.

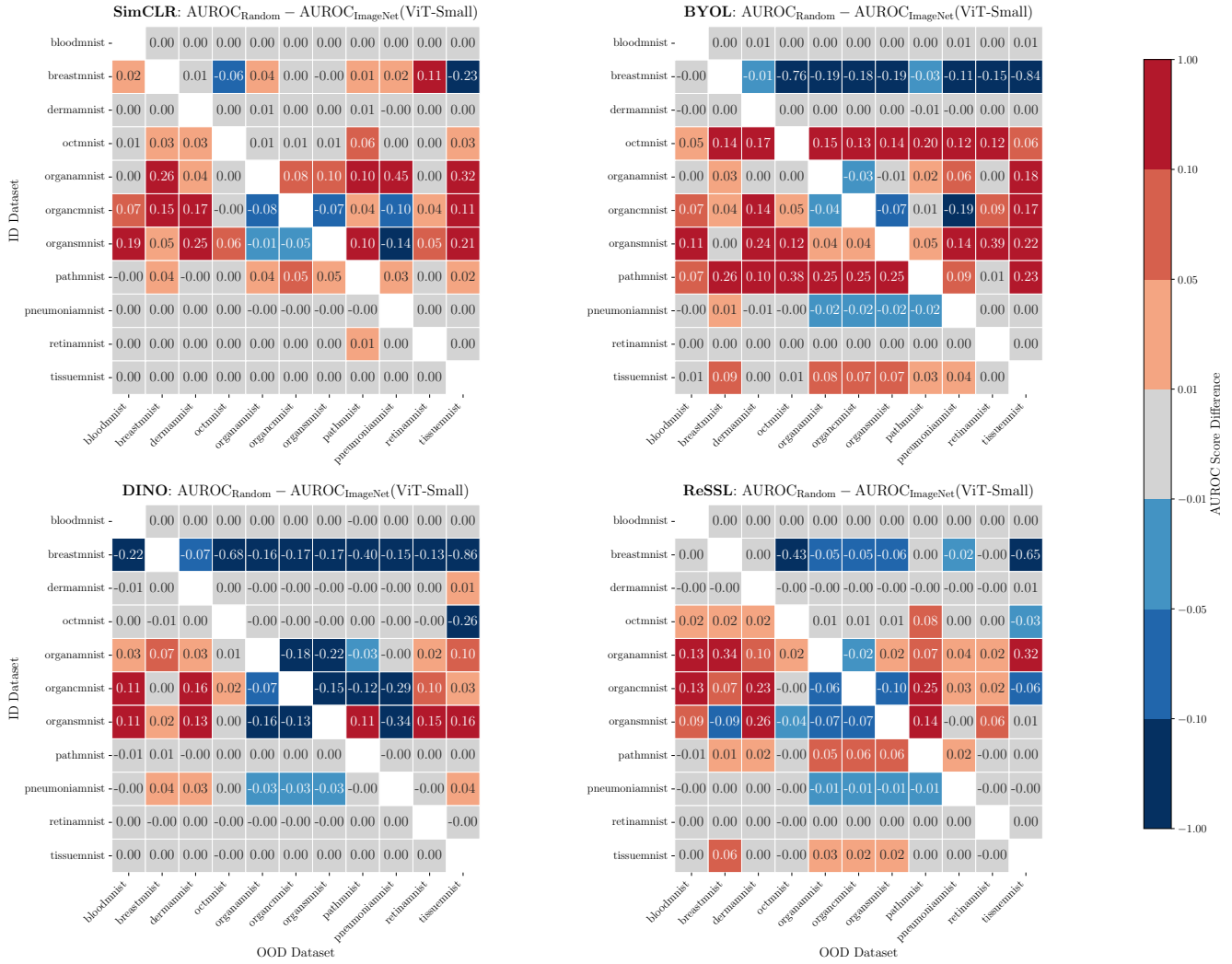


Figure 26. Effect of initialization (Random vs. IMAGENET1K) on AUROC scores for OOD detection across various dataset combinations and SSL methods with ViT-Small backbone. Positive values (blue) indicate better OOD detection performance with the random initialization, while negative values (red) favor IMAGENET1K initialization.

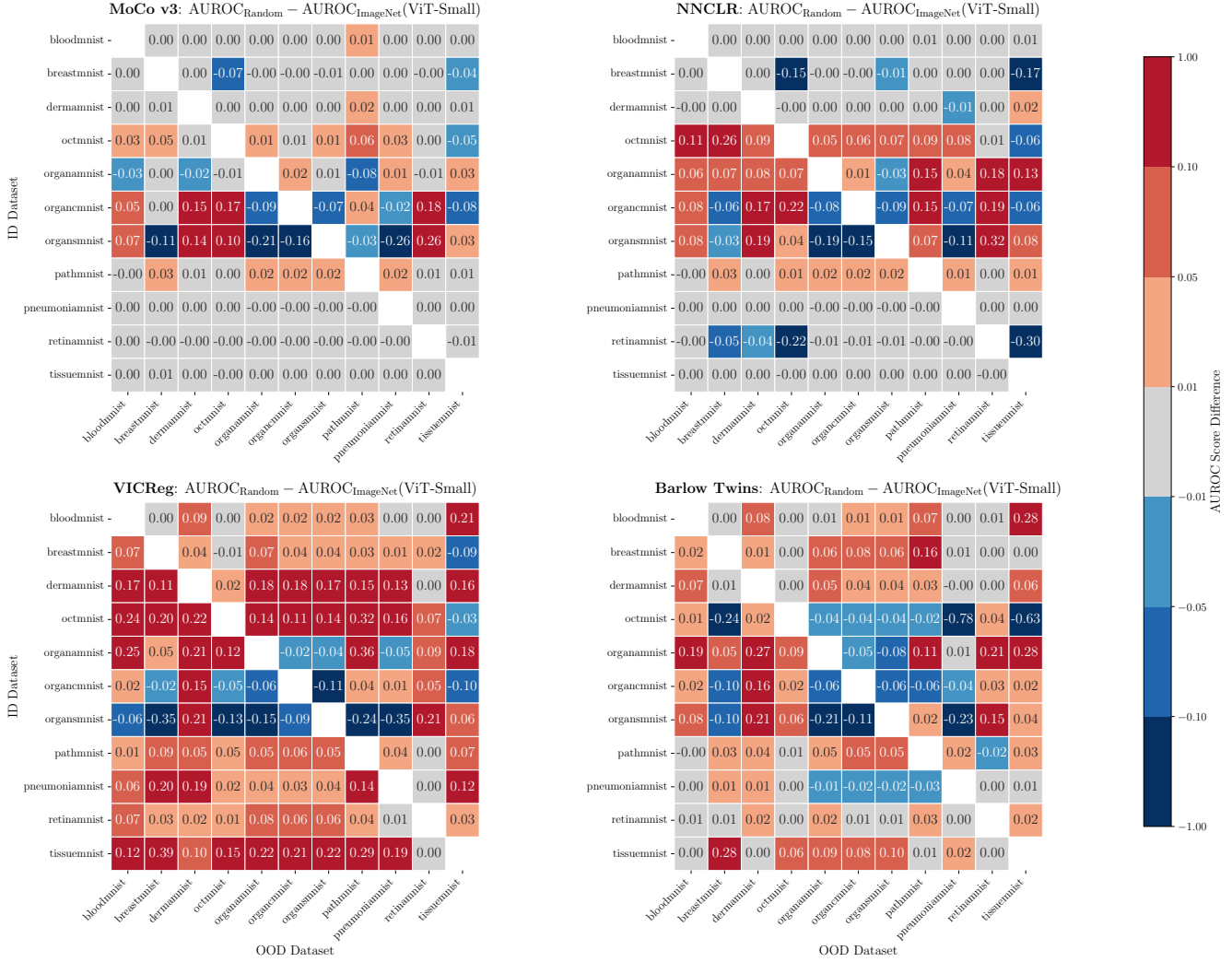


Figure 27. Effect of initialization (Random vs. IMAGENET1K) on AUROC Scores for OOD detection across various dataset combinations and SSL methods with ViT-Small backbone. Positive values (blue) indicate better OOD detection performance with the random initialization, while negative values (red) favor IMAGENET1K initialization.

D.3 Generalizability

In Figures 29 and 30, we provide a detailed analysis of cross-dataset transfer performance across the MedMNIST collection for various self-supervised learning methods.

The heatmaps illustrate the performance matrix, where each row corresponds to a source (training) dataset and each column corresponds to a target (test) dataset. The diagonal elements represent in-domain performance, indicating the results when the source and target datasets are identical. Off-diagonal elements reveal the transferability of learned representations, showcasing how well models trained on one dataset generalize to others.

This comprehensive analysis offers insights into the strengths and limitations of different SSL methods when applied to diverse medical datasets, highlighting their adaptability in cross-domain scenarios.

OOD Detection Score Differences: Single-domain vs. Multi-domain Models

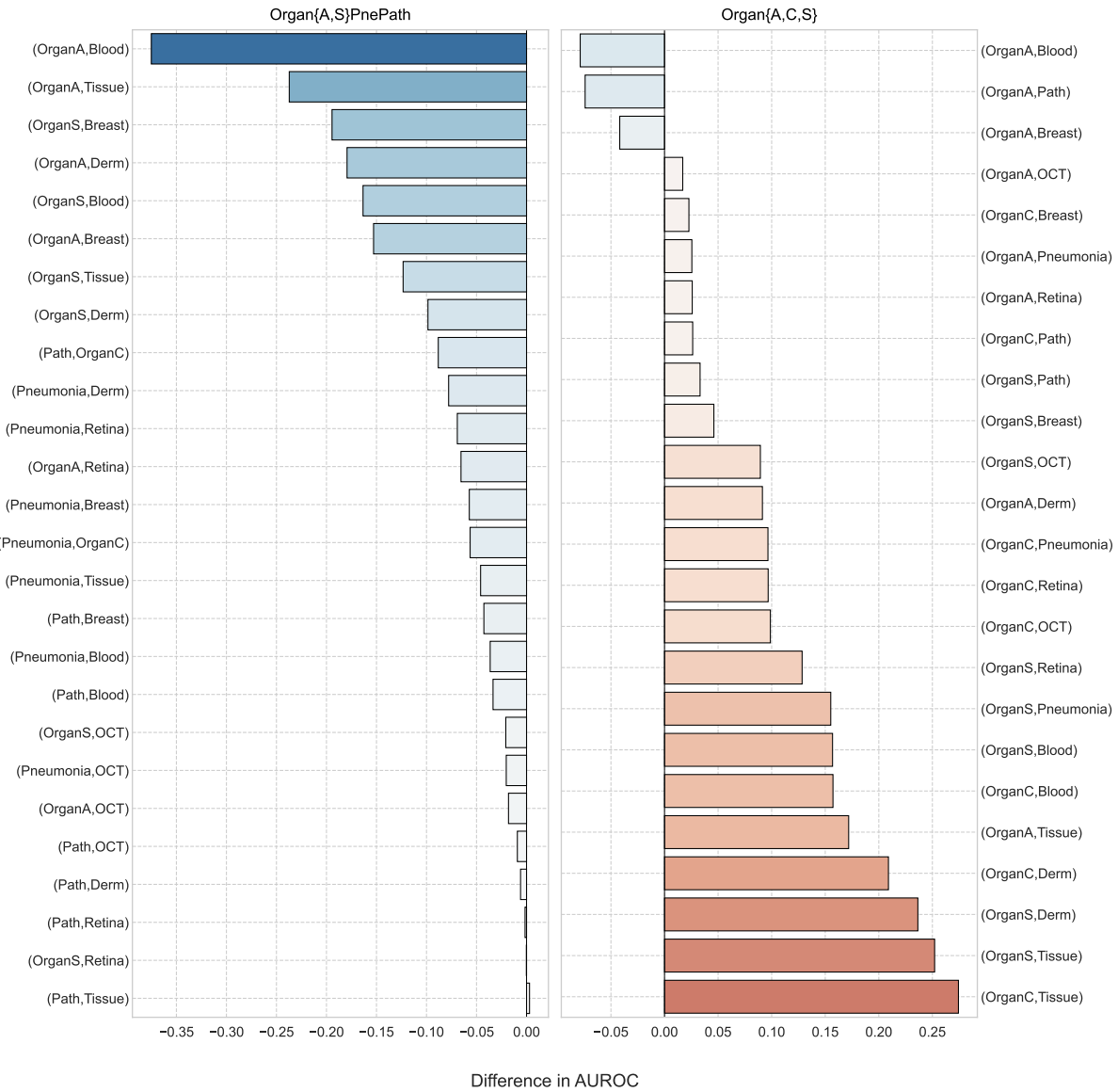


Figure 28. Differences in OOD AUROC scores between models trained on single-domain datasets and those trained on multi-domain datasets, averaged across different models. The y-axis lists the $(\mathcal{P}_{ID}, \mathcal{P}_{OOD})$ pairs, where \mathcal{P}_{ID} represents the in-domain dataset used to train single-domain models and to calculate Gaussian class centers for both single-domain and multi-domain models, while \mathcal{P}_{OOD} represents the out-of-distribution (OOD) dataset. Positive values on the x-axis indicate higher average AUROC scores for single-domain models, whereas negative values favor multi-domain models. Left: Comparison between single-domain models and models trained on the multi-domain dataset Organ{A,C,S}. Right: Comparison between single-domain models and models trained on Organ{A,S}PnePath.

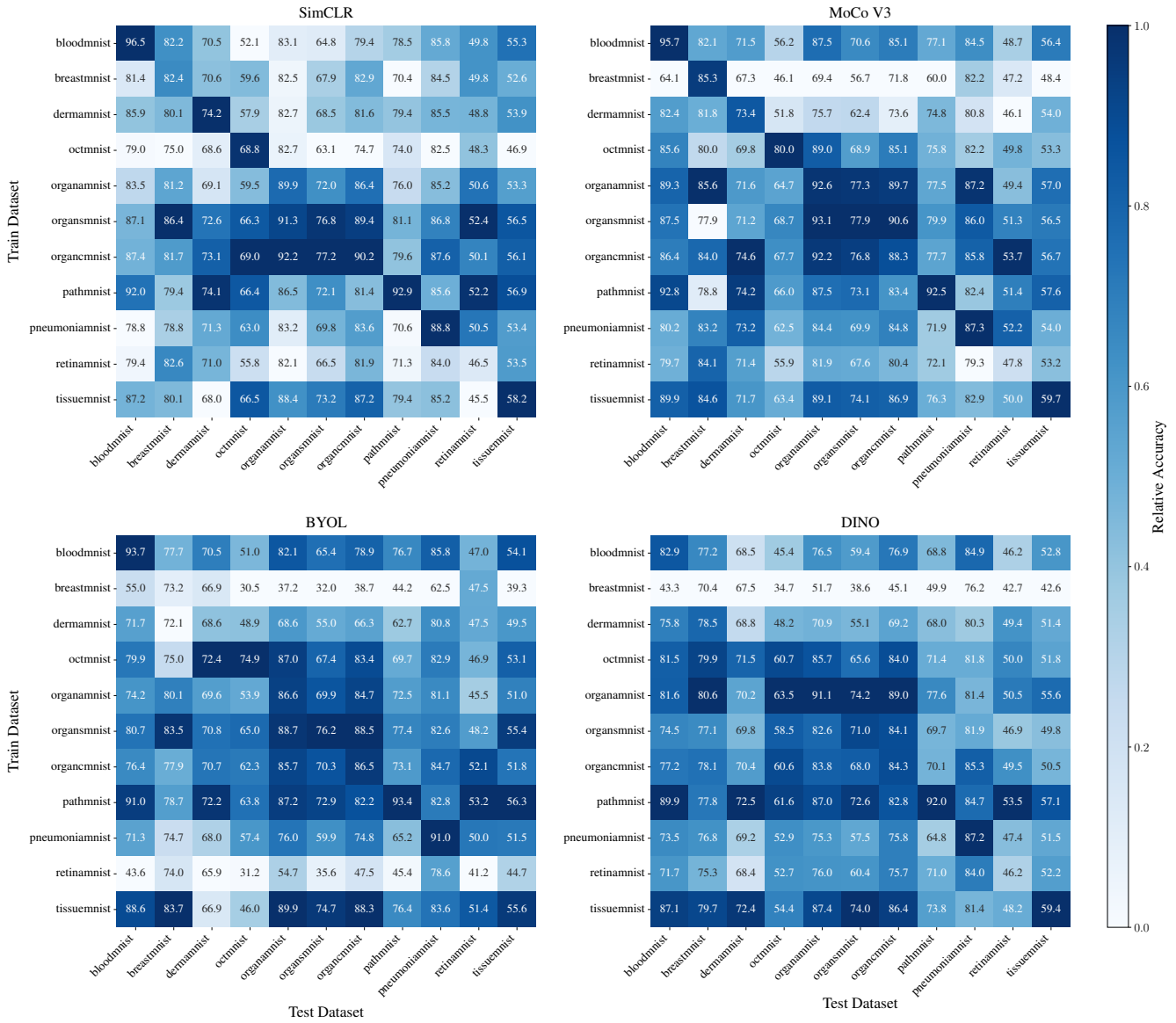


Figure 29. Cross-dataset transfer performance of four SSL methods (SimCLR, MoCo v3, BYOL, and DINO) using ResNet-50 with random initialization. Each heatmap shows the linear evaluation accuracy (%) when the model is pre-trained on one dataset (y-axis) and evaluated on another (x-axis), with column-wise normalized color intensities where darker blue indicates higher relative performance.

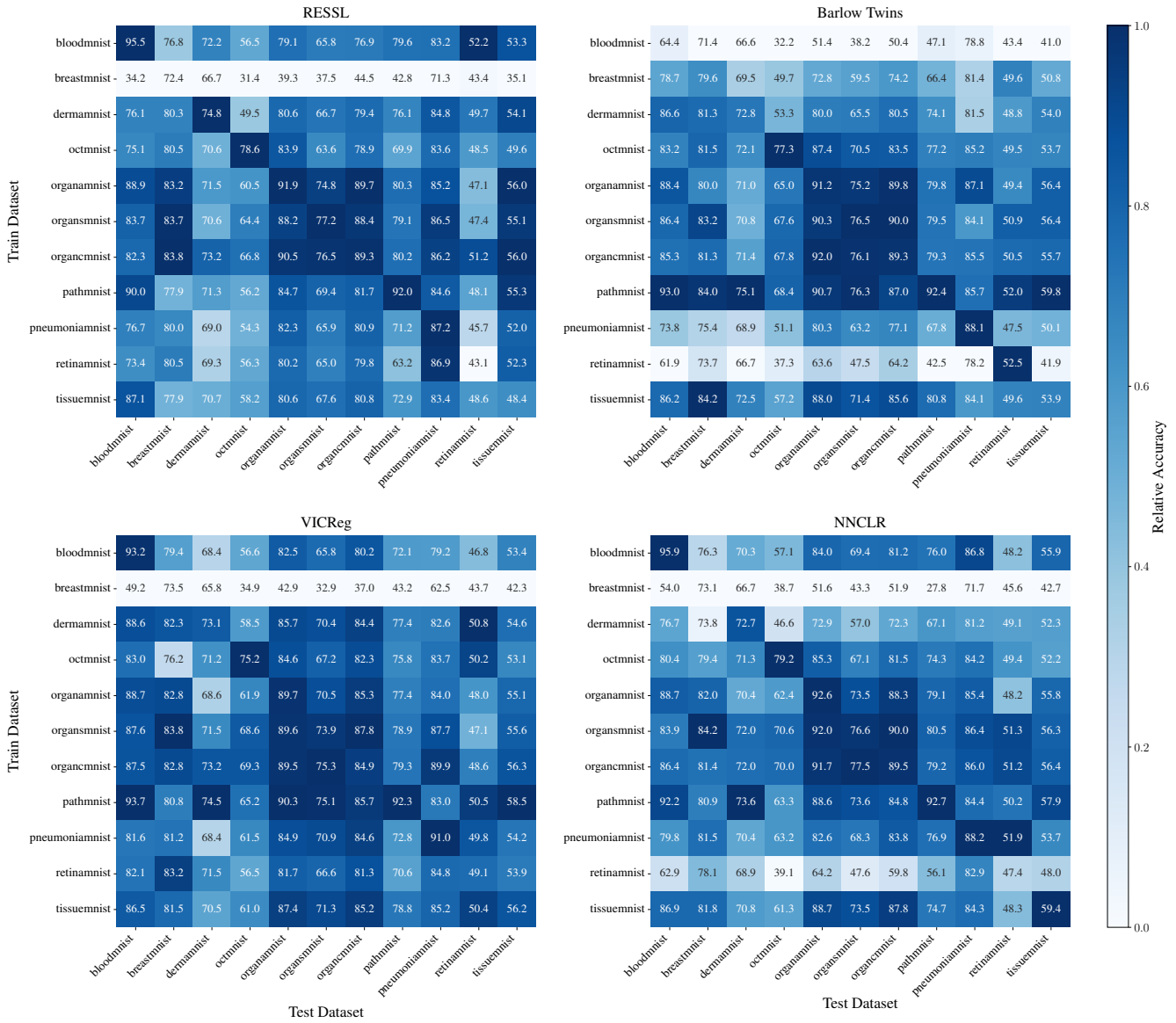


Figure 30. Cross-dataset transfer performance of four SSL methods (RESSL, Barlow Twins, VICReg, and NNCLR) using ResNet-50 with random initialization. Each heatmap shows the linear evaluation accuracy (%) when the model is pre-trained on one dataset (y-axis) and evaluated on another (x-axis), with column-wise normalized color intensities where darker blue indicates higher relative performance.

Mean Cross-Dataset Performance: In Figure 31, we report the mean accuracies across five SSL methods (SimCLR, MoCo v3, ReSSL, DINO, and BYOL) for 13 distinct medical imaging datasets. The performance matrix, visualized with column-wise normalized colors, includes both single-domain and multi-domain datasets (Organ{A,C,S} and Organ{A,S}PnePath). Matrix elements, where the train and test datasets are identical, represent the in-domain performance. Notably, the Organ{A,C,S} datasets exhibit stronger transfer performance among themselves, forming a distinct cluster that suggests these datasets share similar underlying features, which is due to their shared medical imaging modality with different viewing perspectives.

Furthermore, the empirical results demonstrate the superiority of multi-domain training, with Organ{A,C,S} exhibiting superior performance in 6 out of 11 target datasets compared to its constituent domains (as shown in Figure 31). This multi-domain approach achieves a mean accuracy of 76.11% across all target datasets, significantly outperforming the individual constituent domains which achieve mean accuracies of 74.14%, 75.06%, and 75.07% respectively. The analysis suggests a positive correlation between dataset size and source robustness, with the smallest datasets (BreastMNIST: 780 samples, RetinaMNIST: 1,600 samples) showing the poorest generalization performance. However, this correlation is not absolute, as evidenced by PathMNIST achieving the second-highest robustness despite some larger datasets performing worse. Interestingly, while Organ{A,S}PnePath does not consistently outperform its constituent datasets on most individual targets (as shown in Figure 32), it emerges as the most robust source dataset overall, achieving the highest average test accuracy (76.33%) across all target domains. This suggests that while domain-specific pre-training can provide better performance on particular targets, combining diverse domains leads to better overall generalization.

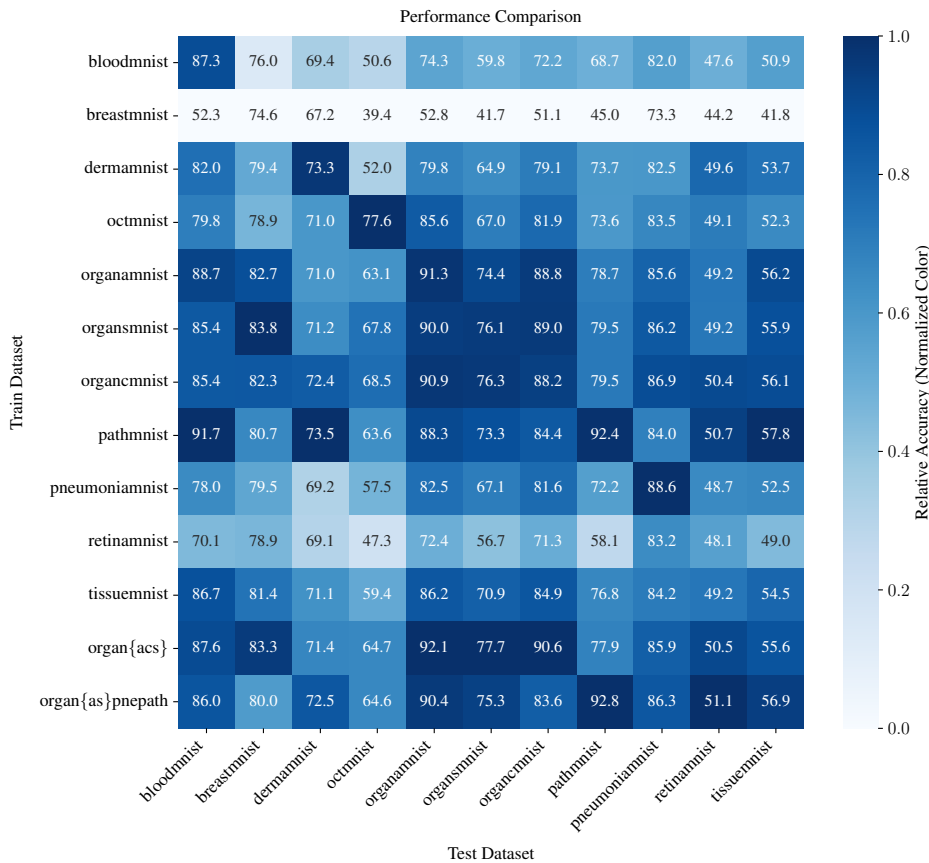


Figure 31. Performance matrix showing cross-dataset accuracy results averaged across five self-supervised methods (SimCLR, MoCo v3, ReSSL, DINO, BYOL). Values indicate mean accuracy percentages, with colors normalized per column to better visualize relative performance within each target domain.

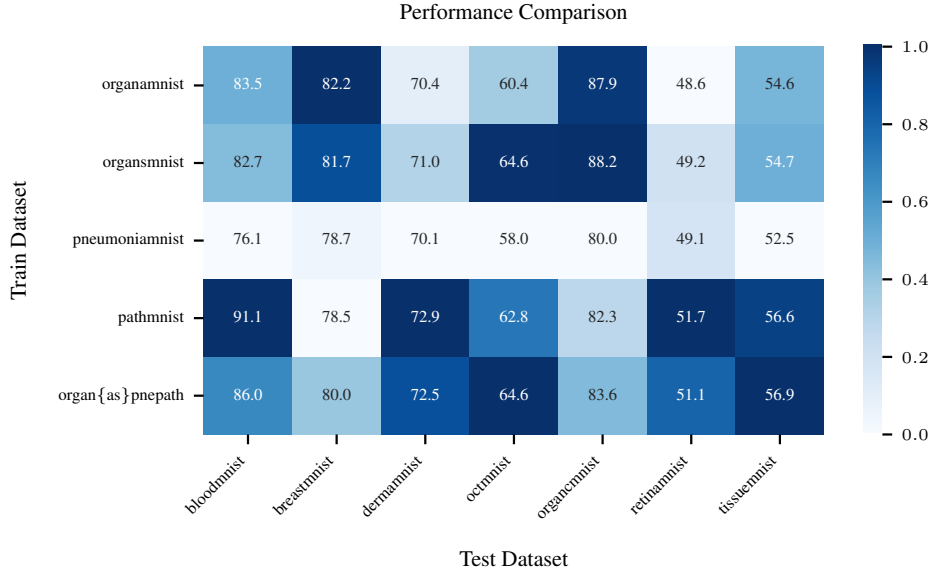


Figure 32. Performance matrix showing cross-domain accuracy results for Organ{A,S}PnePath and its constituent single-domain datasets across other target datasets, averaged over five self-supervised methods (SimCLR, MoCo v3, ReSSL, DINO, BYOL). Each row represents a source dataset used for training, while columns show the target datasets for evaluation. Values indicate mean accuracy percentages, with colors normalized per column to better visualize relative performance within each target domain.

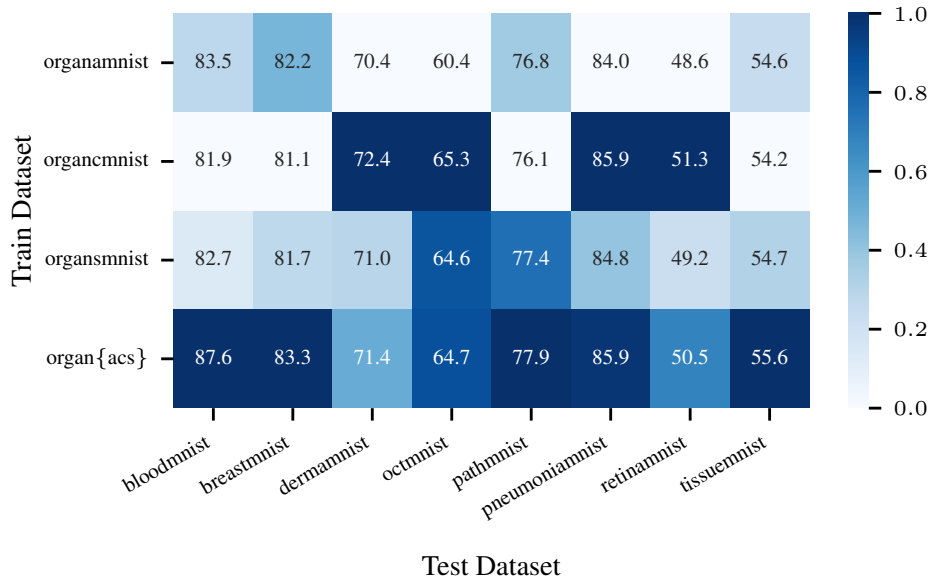


Figure 33. Performance matrix showing cross-domain accuracy results for Organ{A,C,S} and its constituent single-domain datasets across other target datasets, averaged over five self-supervised methods (SimCLR, MoCo v3, ReSSL, DINO, BYOL). Each row represents a source dataset used for training, while columns show the target datasets for evaluation. Values indicate mean accuracy percentages, with colors normalized per column to better visualize relative performance within each target domain.

D.4 KNN Evaluation

Here, we evaluate the effectiveness of a simpler, computationally efficient classifier on top of self-supervised features, compared to a standard linear classifier. We train a KNN classifier on features extracted from the training dataset using selected backbones (ResNet-50 and ViT-Small) with both IMAGENET1K and random initialization. To ensure optimal KNN performance, we conduct a grid search over several hyperparameters, including the number of neighbors, temperature scaling,

Comparison of IMAGENET1K vs. Random Initialization for In-Domain and Cross-Dataset Performance: In Table 19, we provide the results of paired t -tests to analyze the effect of IMAGENET1K initialization on the in-domain performance and generalizability of the learned representations. To evaluate the impact of IMAGENET1K initialization compared to random initialization, we conducted paired t -tests for each test dataset across all cross-dataset training combinations including the in-domain setting where test and train splits come from the same dataset. The results demonstrate statistically significant improvements ($p < 0.05$) across all datasets, with varying degrees of benefit. OCTMNIST showed the largest relative improvement ($22.08 \pm 31.16\%$), followed by PathMNIST ($16.95 \pm 32.10\%$) and OrganSMNIST ($13.55 \pm 29.62\%$). Even datasets with higher baseline accuracies benefited from IMAGENET1K initialization, with BloodMNIST improving from 80.23 to 88.41 ($13.52 \pm 27.58\%$ relative gain). The smallest improvements were observed in BreastMNIST ($3.47 \pm 6.47\%$), DermaMNIST ($3.76 \pm 4.48\%$), PneumoniaMNIST ($3.93 \pm 7.28\%$) and RetinaMNIST ($4.00 \pm 7.56\%$), though these gains remained statistically significant. Notably, all improvements were achieved with strong statistical significance ($p < 0.05$), providing robust evidence for the benefit of IMAGENET1K initialization in self-supervised pretraining across diverse medical imaging domains.

Dataset	Random Init.	IMAGENET1K Init.	Improvement	p -value
BloodMNIST	80.52	88.41	$13.52 \pm 27.58\%$	0.0000
BreastMNIST	79.68	82.26	$3.47 \pm 6.47\%$	0.0000
DermaMNIST	70.67	73.26	$3.76 \pm 4.48\%$	0.0000
OctMNIST	58.33	68.24	$22.08 \pm 31.16\%$	0.0000
OrganAMNIST	81.54	88.94	$12.79 \pm 26.96\%$	0.0000
OrganCMNIST	79.57	85.15	$10.86 \pm 27.45\%$	0.0002
OrganSMNIST	66.31	72.30	$13.55 \pm 29.62\%$	0.0000
PathMNIST	72.90	81.86	$16.95 \pm 32.10\%$	0.0000
PneumoniaMNIST	83.50	86.52	$3.93 \pm 7.28\%$	0.0000
RetinaMNIST	48.82	50.63	$4.00 \pm 7.56\%$	0.0000
TissueMNIST	52.99	57.46	$9.50 \pm 13.30\%$	0.0000

Table 19. Comparison of random initialization versus IMAGENET1K initialization across different medical datasets. Results show mean accuracy (%) for both initialization methods, relative improvement, and statistical significance.

and distance functions (Euclidean and cosine). This approach allows us to systematically assess how well KNN classifiers leverage the representations across various datasets and initialization strategies.

Figure 34 presents a detailed comparison of the performance differences between KNN and linear classifiers across various self-supervised learning methods on multiple datasets. Positive values (shaded in red) indicate higher accuracy with the linear classifier, while negative values (blue) highlight cases where KNN performs better. Gray values represent minimal accuracy differences, suggesting similar performances between the classifiers in those instances. This analysis reveals that the choice of classifier can significantly impact performance, with notable variation across datasets and initialization strategies (IMAGENET1K vs. random) on ResNet-50 and ViT-Small backbones.

Interestingly, there is a greater disparity in performance with random initialization compared to IMAGENET1K initialization. Specifically, there are 36 absolute differences exceeding 5 (indicated by a darker shade) with random initialization, whereas only 7 such differences occur with IMAGENET1K initialization. Another notable trend is that the initialization strategy and backbone choice primarily drive these performance differences, with consistent patterns across methods for the same initialization and backbone combination. This is evident from the vertical strips of similar colors or values, indicating that the trends are largely method-independent. However, exceptions like BreastMNIST and RetinaMNIST display different colors in their respective strips, likely due to their smaller dataset sizes, where greater fluctuations are expected.

In conclusion, IMAGENET1K-initialized models generally favor linear classifiers, while random-initialized models show more instability in performance. These findings emphasize the importance of carefully selecting both the initialization strategy and classifier type based on dataset characteristics, as these choices can meaningfully impact model performance. In particular, there are cases where using a KNN classifier, which is computationally less demanding, can yield better results than training a linear classifier.

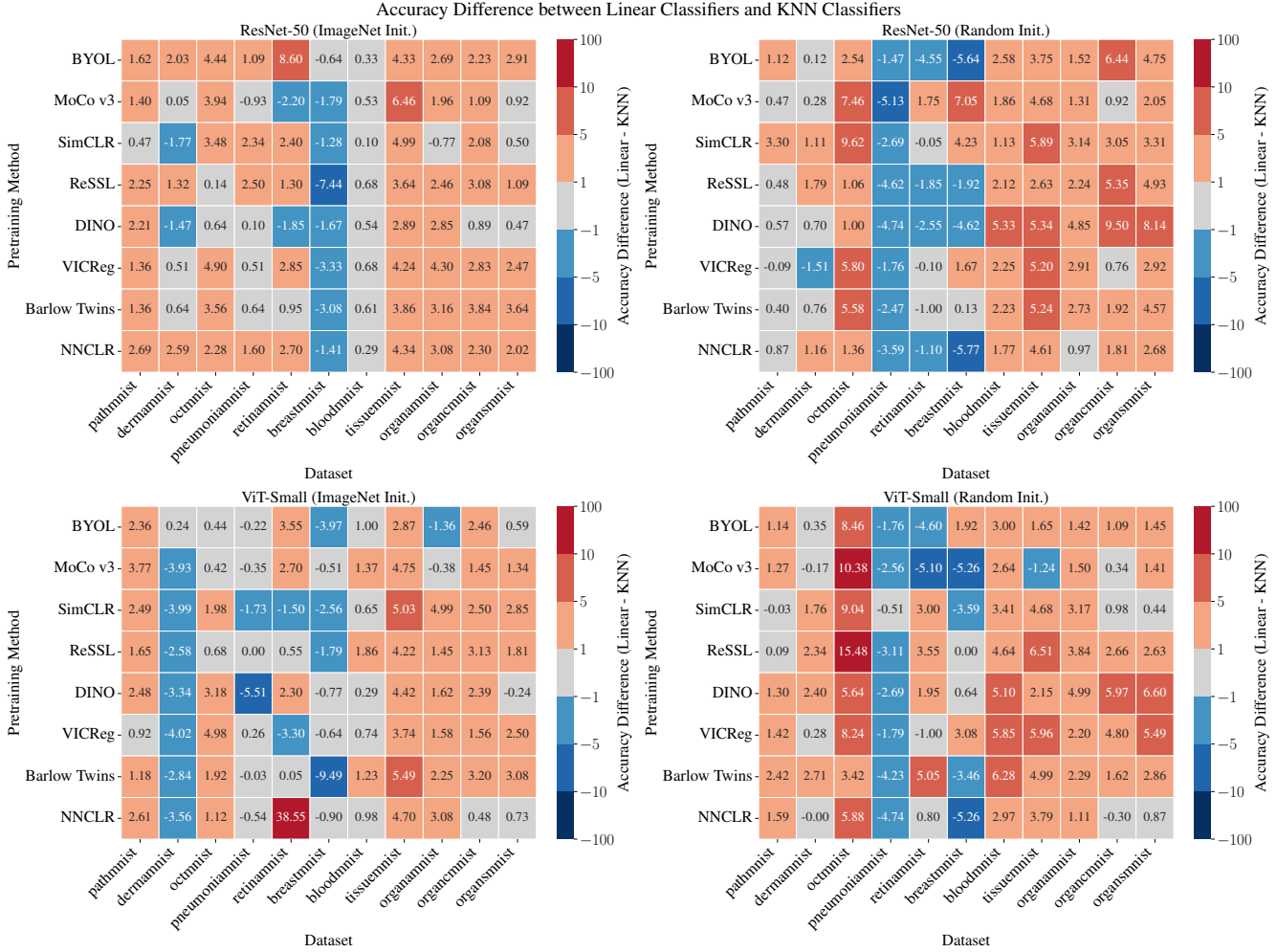


Figure 34. Heatmaps showing the accuracy differences between KNN and linear classifiers for various methods on different datasets, evaluated for both ResNet-50 and ViT-Small backbones as well as IMAGENET1K and random initializations. Positive values (shades of red) indicate higher accuracy with a linear classifier while negative values (shades of blue) indicate higher accuracy with a KNN classifier. Gray values show where the accuracy differences are less significant, less than 1.

E. Conclusion & Future Work

We present a comprehensive empirical study evaluating the robustness, generalizability, and cross-domain efficacy of self-supervised learning methods in medical imaging. Our analysis encompasses 11 distinct medical datasets from MedMNIST, examining 8 popular SSL approaches across both convolutional (ResNet-50) and transformer-based (ViT-Small) architectures. To ensure rigorous comparison, we conduct hyperparameter optimization through grid search for both pre-training and linear evaluation phases, and report the mean accuracy with confidence interval over five different runs. Our experimental framework investigates five distinct pre-training paradigms: (1) supervised learning with random initialization, (2) supervised learning with supervised IMAGENET1K initialization, (3) self-supervised learning with random initialization, (4) self-supervised learning with supervised IMAGENET1K initialization, and (5) self-supervised learning with self-supervised IMAGENET1K initialization. We evaluate these approaches across multiple dimensions, including in-domain classification performance, out-of-distribution (OOD) detection capabilities, transfer learning efficacy, and cross-dataset generalization.

Comparison of Augmentations For consistency in our comparisons, we maintain the default augmentation strategies specified in the `solo-learn` library for each SSL method. Future research could explore the impact of domain-specific augmentation strategies on model performance, providing insights into the relationship between data augmentation choices and in-domain performance, OOD detection, and generalizability.

Extensive Hyperparameter Search We conducted a grid search across learning rates and weight decay parameters during the encoder pre-training phase and then linear evaluation. Future research directions could explore a broader hyperparameter space by investigating the effects of varying batch sizes, temperature scaling factors, and momentum coefficients in the optimization process.

Additional Multi-Domain Datasets We evaluated multi-domain learning across two distinct dataset combinations: one comprising same-modality datasets (Organ{A,C,S}) and another incorporating datasets from different imaging modalities. Future research could extend this multi-domain investigation by systematically exploring a broader spectrum of domain combinations, encompassing both intra-modality (datasets within the same imaging modality) and cross-modality scenarios. This expanded analysis would provide deeper insights into the scalability and limitations of multi-domain learning approaches when handling varying numbers of different domains and diverse modality combinations.

Architectural Variations Our investigation focused on ResNet-50 and ViT-Small architectures as representative examples of convolutional and transformer-based approaches. Future studies could explore the impact of architecture using different variations of convolutional and transformer-based backbones. Additionally, investigating the role of architectural components like attention mechanisms, skip connections, and normalization layers specifically in the medical imaging context could reveal design principles better suited for healthcare applications.